# Dynamical and Mechanistic Effects of High Pressure Fluids in the Earth's Crust

Dissertation
zur
Erlangung des Doktorgrades (Dr. rer. nat.)
der
Mathematisch-Naturwissenschaftlichen Fakultät
der
Rheinischen Friedrich-Wilhelms-Universität Bonn

vorgelegt von
Anna Zoporowski
aus
Königshütte

Bonn 2011

Angefertigt mit Genehmigung der Mathematisch-Naturwissenschaftlichen Fakultät
der Rheinischen Friedrich-Wilhelms-Universität Bonn
am Steinmann-Institut für Geologie, Mineralogie und Paläontologie

1. Referent: Prof. Dr. Stephen A. Miller
2. Referent: Prof. Dr. Andreas Kemna

Tag der Promotion: 01. März 2012
Erscheinungsjahr: 2012

# Abstract

Overpressurized fluids in the lithosphere play a significant role in a diverse range of globally observed natural hazards. Their occurrence during volcanic eruptions or earth degassing processes is apparent, but their influence on seismic processes is still underestimated. The projects examined in this thesis aim to advance the physical understanding of fluid pressure related geo-hazards, and their effects on hydro-mechanical and dynamical systems. The cases discussed here cover many areas of geophysical research, analyzes of aftershock triggering scenarios, modeling dynamical behavior of fluid flow in volcanic systems, and developing schemes for understanding earthquake-fluid pressure correlations

A numerical model, developed for the Indonesian LUSI mud volcano, provides a dynamical description of mud volcano eruptions. Influence of rheological effects and fluid properties on extrusion rate, cyclic behavior and long-term decay are investigated. The conceptual model is stable to parameter changes, being adapted for and transferable to various mudflow issues.
We investigate the involvement of overpressurized fluids in earthquake generation with spatiotemporal investigations on the 2009 L'Aquila aftershock sequence in Italy. Analyses of the generally accepted triggering mechanism of static stress transfer shows that a pure mechanistic process is not responsible for the seismic events. An investigation of the volumetric strain response suggests high-pressure fluid induced seismicity, a result consistent with high pore pressures at depth inferred from earthquake focal mechanisms of that event.
Coupled fluid-flow and brittle failure processes are also implicated in the "drumbeat" seismicity observed at Mount St. Helens, Washington. A conceptual and mathematical model is developed to explain this remarkably periodic volcanic seismicity associated with the extrusion of a solid lava dome. We develop a numerical model by including stress-weakening effects of fluids to a dry friction model to mimic on-site observations and to point out limitations of the conceptual formulation.

We aim to improve methods for analyzing, quantifying and modeling natural phenomena in seismology, volcanology and earth sciences in general with the focus on identifying overpressurized fluids as underlying driving mechanism and involving their specific characteristics in mathematical models. The complexity of geophysical processes can be successfully approached by means of interdisciplinary research, and proceedings on prognostic modeling, reliable forecasting, early warning systems and hazard assessment methods can be achieved, with the benefit of minimizing natural disasters worldwide.

# Zusammenfassung

Das Vorkommen von unter Hochdruck stehenden Fluiden in der Erdkruste findet eine zunehmende Beachtung in der Untersuchung von Naturgewalten. Während ihre globale Rolle bei Vulkanausbrüchen oder bei Erdentgasungsprozessen offensichtlich ist, wird ihr Einfluss im seismologischen Kontext noch weitgehend unterschätzt. Mit den hier vorgestellten Projekten tragen wir dazu bei, das grundlegende physikalische Verständnis fluider Strömungen und ihrer statischen und dynamischen Auswirkungen zu verbessern. Die Fallstudien zur Nachbebensequenzanalyse, Modellierung von Fluiddynamik und Wechselwirkung beider Phänomene verbinden darüber hinaus verschiedene Gebiete geophysikalischer Forschung.

Wir entwickeln das erste numerische Modell, das die Dynamik von Schlammvulkanen beschreibt. Am Beispiel des indonesischen Schlammausbruchs LUSI untersuchen wir Effekte rheologischer und fluiddynamischer Parameter auf das Extrudier- und Langzeitverhalten. Die Stabilität des Modells gegenüber Anfangswerten ermöglicht eine Anpassung und Übertragung des Konzepts auf weitere Schlammvulkane.
Mit der Untersuchung der Nachbebenmuster beim L'Aquila Erdbeben von 2009 (Italien), decken wir die Frage nach Fluideinflüssen in der Seismologie ab. Da die konventionell angenommene statische Spannungsübertragung als zugrunde liegender Erdbebenauslösemechanismus die Lage der Nachbebenhypozentren nicht erklären kann, ebnen unsere Ergebnisse den Weg für neue Ansätze in der Aufdeckung fluidinduzierter seismischer Ereignisse.
Beide Aspekte, fluiddynamische und seismologische, werden in der Beschreibung der vulkanischen Seismizität am Mount St. Helens, USA, miteinander in Beziehung gebracht. Wir erweitern ein Modell, das die ungewöhnlich periodischen Erdbebensignale während der Extrusion von verfestigter Lava beschreibt, mit der spannungssenkenden Wirkung des Fluiddrucks. Neben der Reproduktion numerischer Ergebnisse und beobachteter Ereignisse, gelingt es uns im Hinblick auf zukünftige Untersuchungen, die Grenzen des Modells aufzuzeigen.

Mit den Schwerpunkten auf der Identifizierung von Fluiden als Antriebsmechanismus zahlreicher geophysikalischer Phänomene und auf der Einbeziehung ihrer spezifischen Merkmale in mathematische Modelle, verbessern wir gängige und etablieren neue Analyse-, Quantifizierungs- und Modellierungsmethoden in der Seismologie und Vulkanologie. Die interdisziplinären Forschungsansätze ermöglichen es, die Komplexität geophysikalischer Prozesse erfolgreich anzugehen sowie Verfahren der prognostischen Modellierung weiterzuentwickeln, und dadurch die Auswirkungen von Naturkatastrophen weltweit zu minimieren.

# Contents

1 **Introduction** **1**

2 **Theoretical Background** **11**

2.1 Mechanisms for developing overpressures . . . . . . . . . . . . . . . . . 11

2.2 Stress-weakening in earthquakes and faulting . . . . . . . . . . . . . . . 15

2.3 The nature of high-pressure fluid flow . . . . . . . . . . . . . . . . . . . 20

2.4 Earthquakes at volcanic settings . . . . . . . . . . . . . . . . . . . . . . 26

3 **Modeling Eruption Cycles and Decay of Mud Volcanoes** **33**

3.1 Introduction . . . . . . . . . . . . . . . . . . . . . . . . . . . . . . . . 33

3.2 Conceptual model . . . . . . . . . . . . . . . . . . . . . . . . . . . . . . 35

3.3 Mathematical formulation . . . . . . . . . . . . . . . . . . . . . . . . . 37

3.3.1 Governing equations . . . . . . . . . . . . . . . . . . . . . . . . 37

3.3.2 Supplementary equations . . . . . . . . . . . . . . . . . . . . . . 38

3.3.3 Results . . . . . . . . . . . . . . . . . . . . . . . . . . . . . . . . 39

3.4 Numerical results . . . . . . . . . . . . . . . . . . . . . . . . . . . . . . 40

3.4.1 Mud flow with deflating reservoir . . . . . . . . . . . . . . . . . 41

3.4.2 Comparison with non-deflating reservoir . . . . . . . . . . . . . 44

3.5 Discussion and conclusions . . . . . . . . . . . . . . . . . . . . . . . . . 47

4 **Fluid Pressure Driven Aftershocks Following the 2009 L'Aquila Earthquake** **51**

4.1 Introduction . . . . . . . . . . . . . . . . . . . . . . . . . . . . . . . . 51

4.2 Statistical analysis, Omori's Law . . . . . . . . . . . . . . . . . . . . . 53

4.3 Spatiotemporal patterns . . . . . . . . . . . . . . . . . . . . . . . . . . 55

4.4 Stress and dilatation calculations . . . . . . . . . . . . . . . . . . . . 58
  4.4.1 Fault geometry from InSAR . . . . . . . . . . . . . . . . . . . 58
  4.4.2 GPS source modeling . . . . . . . . . . . . . . . . . . . . . . . 59
  4.4.3 Fault with non-uniform slip distribution . . . . . . . . . . . . 60
  4.4.4 Multi-fault system . . . . . . . . . . . . . . . . . . . . . . . . 62
  4.4.5 Results at depth . . . . . . . . . . . . . . . . . . . . . . . . . 62
4.5 Discussion and Conclusions . . . . . . . . . . . . . . . . . . . . . . . 64

**5 Coupling Degassing with Lava Dome Extrusion and Periodic Seismicity for the 2004 Eruption of Mount St. Helens 67**
5.1 Introduction . . . . . . . . . . . . . . . . . . . . . . . . . . . . . . 67
5.2 Conceptual model and system equations . . . . . . . . . . . . . . . . 69
5.3 Model results . . . . . . . . . . . . . . . . . . . . . . . . . . . . . . 73
5.4 Discussion: Extensions and limitations . . . . . . . . . . . . . . . . . 78
5.5 Concluding remarks . . . . . . . . . . . . . . . . . . . . . . . . . . . 80

**6 Summary and Conclusion 83**

**A Appendix 91**
A.1 Runge-Kutta method . . . . . . . . . . . . . . . . . . . . . . . . . . 91
A.2 Coulomb failure stress analysis . . . . . . . . . . . . . . . . . . . . . 94

**Bibliography 99**

**List of Figures 113**

**List of Tables and Listings 121**

**Symbols and Abbreviations 123**

**Acknowledgments 129**

# Chapter 1

# Introduction

Natural phenomena and hazards have become a major scientific research field as their effects directly influence our living on Earth. Natural hazards can become natural disasters when meeting vulnerability, leading to environmental, financial and human losses (Wisner et al., 2004):

> *In disasters, a geophysical or biological event is implicated in some way as a trigger event or a link in a chain of causes. Yet, even where such natural hazards appear to be directly linked to loss of life and damage to property, there are social factors involved that cause peoples' vulnerability and can be traced back sometimes to quite 'remote' root and general causes. This vulnerability is generated by social, economic and political processes that influence how hazards affect people in varying ways and with differing intensities. [. . . ] By vulnerability we mean the characteristics of a person or group and their situation that influence their capacity to anticipate, cope with, resist and recover from the impact of a natural hazard (an extreme natural event or process). It involves a combination of factors that determine the degree to which someone's life, livelihood, property and other assets are put at risk by a discrete and identifiable event (or series or 'cascade' of such events) in nature and in society.*

Natural hazards are subdivided into different categories such as geological, atmospheric and hydrological hazards, and many of them are interrelated. Especially geohazards, like earthquakes, volcanism, avalanches and mudflows, and their interaction are currently omnipresent due to critical incidents in the last years:

- The Indian Ocean tsunami of December 26, 2004 along the coasts of most landmasses bordering the Indian Ocean, killing over 230,000 people in fourteen countries, was caused by the undersea Sumatra-Andaman magnitude 9.3 earthquake with an epicenter off the west coast of Sumatra, Indonesia (Lay et al., 2005).

- The eruption of mud and gas called LUSI that started 29th of May 2006 in North east Java (Mazzini et al., 2007), covered huge areas of the Sidoarjo

**Figure 1.1:** View from north-west of the caldera of Piton de la Fournaise, Île de la Réunion, Indian Ocean. The hot spot fed volcano is currently one of the most active volcanoes in the world, affecting the lives of the island inhabitants.

regency and wiped out twelve villages, displacing more than 40,000 inhabitants (Berry, 2010).

- The $M_w = 6.3$ main shock of the L'Aquila earthquake occurred on April 6, 2009 in the Italian Apennines and was followed by extensive aftershock sequences (Chiarabba et al., 2009). 308 people were killed, approximately 1,500 people were injured, and the earthquake caused damage to between 3,000 and 11,000 buildings, making around 65,000 people homeless (Linnenbrink, 2010).

- The 12 January, 2010 Haiti earthquake with about three million people affected. The epicenter of the magnitude 7.0 earthquake was approximately 25 km west of Port-au-Prince at a depth of 13 km. The United States Geological Survey (USGS) recorded a series of at least 33 aftershocks, fourteen of which were between magnitudes 5.0 and 5.9 (Hayes et al., 2010).

- The 2010 Chile earthquake of February 27 ranks, with a magnitude of 8.8 on the moment magnitude scale, as the sixth largest earthquake ever to be recorded by a seismograph (USGS, 2010). 370,000 homes were destroyed, and hundreds of people were reported killed with estimated damage costs of about 30 billion US dollars (Trenkamp, 2010).

- The eruption series of the Eyjafjallajökull volcano, Iceland, on 14 April 2010 affected the economic, political and cultural activities in Europe and across the world. Volcanic ash was thrown several kilometers up in the atmosphere which led to extensive air travel disruption caused by the closure of airspace in northwest Europe (BBC, 2010).

- The 2011 Tōhoku earthquake, a magnitude $M_w = 9.0$ undersea mega-thrust earthquake off the coast of Japan, occurred on Friday, 11 March 2011 and triggered destructive tsunami waves of up to 38.9 meters (USGS, 2011). In

> addition to the loss of over 15 thousand lives and a massive destruction of infrastructure, the tsunami caused nuclear accidents (meltdowns at three reactors) in the Fukushima I Nuclear Power Plant complex (Paul-Choudhury and Hooper, 2011). The overall cost could reach almost 300 billion US dollars, making it the most expensive natural disaster on record (Kim, 2011).

These examples for earthquake triggered disasters show a strong correlation between environmental hazards and social affiliation. In order to avoid or at least minimize such natural disasters both aspects, the socio-scientific and the natural scientific, have to be considered. While in the former case systematic approaches (e.g. the 'Disaster Risk Reduction') aim to identify, assess and reduce socio-economic vulnerabilities to disasters, the latter focus on the observation, statistical evaluation, physical analysis and modeling of the underlying processes that trigger them. To develop reliable forecasting, early warning systems and hazard assessment methods, the physical mechanisms need to be understood and methods need to be developed for measuring, modeling and predicting geohazards.

The focus of this work is on numerical modeling of observed natural and hazardous phenomena and identification of their underlying geophysical processes. More precisely, we consider the effects of overpressurized fluids in the lithosphere on three exceptional natural hazards that occurred during the last four years, covering statistical data analyses, conceptual physical formulation and prognostic modeling.

**Figure 1.2:** Mostly harmless fumaroles (Rotorua, New Zealand), emitting steam and gases such as carbon dioxide, sulfur dioxide, hydrochloric acid, and hydrogen sulfide, may indicate increasing magmatic activity due to changes in gas concentrations. However, $CO_2$ gas can collect in low-lying valleys because of its density larger than air, with the danger of suffocation for humans and animals.

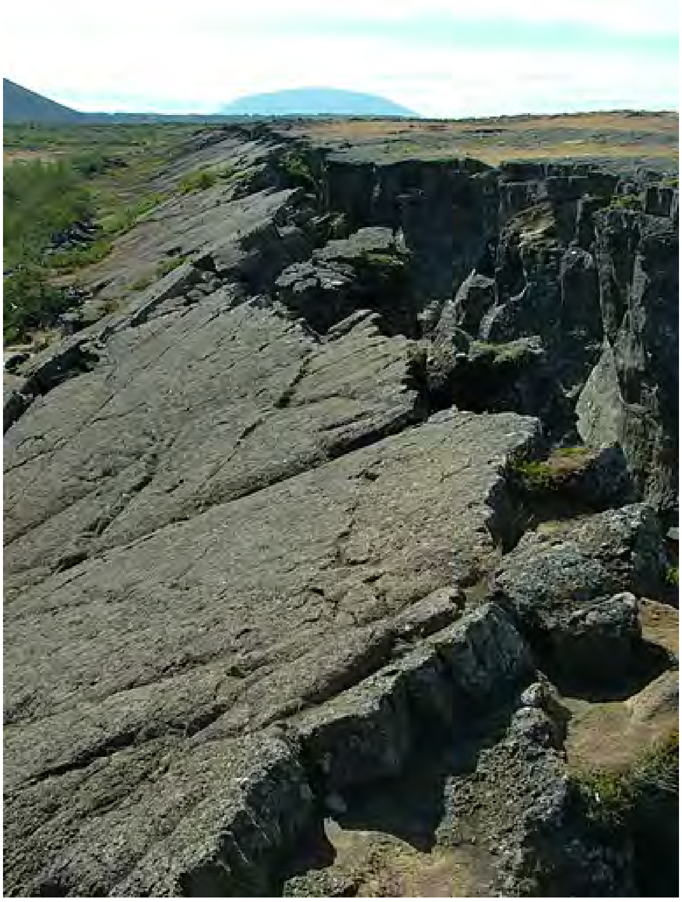

**Figure 1.3:** Living on a tectonic faulting system: the diverging Mid-Atlantic Ridge in the Mývatn district, Iceland. The location offers availability of geothermal power, but also volcanic eruptions and earthquake hazard.

Fluids play various roles in the Earth's crust. In many cases of natural hazards their existence is obvious, such as during volcanic and limnic eruptions, geysers, mud volcanoes and rain-triggered landslides. But, especially in seismology, the impact of trapped overpressurized fluids at depth is still debated. The projects included in this thesis aim to improve our fundamental understanding of fluid pressure behavior in geo-materials and the numerical modeling of their effects, and to apply the results of classical earthquake hazard mapping and analyses to formulate and assist decision-making techniques on identification of overpressurized fluids for possible earthquake triggering scenarios.

This work is sectioned as follows:

The theoretical background and a larger scientific context of the research projects are given in the next chapter, preceding the main parts of this thesis.

In chapter 3 we discuss the eruptive behavior of mud volcanoes and their activation mechanisms against the background of the LUSI eruption in Java (Indonesia) that resulted in huge commercial and cultural damages. Mud volcanoes result from gas- and water-saturated mud extrusion forced through openings in the upper crust, sometimes producing massive quantities of mud on the surface. About 1800 individual sites are reported globally (Dimitrov, 2002), but their triggering mechanism hypotheses are debated, including earthquake-triggering, fault failure, and drilling (Manga et al., 2009). Few approaches on modeling of mud volcanoes exist, mostly concentrating on mechanical investigations, although their evaluation can provide insight into eruptive behavior and contribute to hazard evaluation. In most cases the mud flow dynamics show a cyclic behavior, i.e. continuous activity with periodic seepage for extended times of observation, as well as an alternation between periods of eruption and relative quiescence. This characteristic was also recognized for LUSI, an eruption of mud and gas that started 29th of May 2006 in North east Java. It showed a clear tendency to pulsate every few hours and to erupt in changing cycles, although it was perturbed several times by earthquakes swarms (Davies et al., 2008; Mazzini et al., 2007). The observed oscillatory behavior of mud volcanoes is the focus of this part of the work. We focus on the periodic characteristics and develop a mathematical model where the solution for the material discharge rate oscillates naturally. Our simple model, describing fluid escape from an underground reservoir

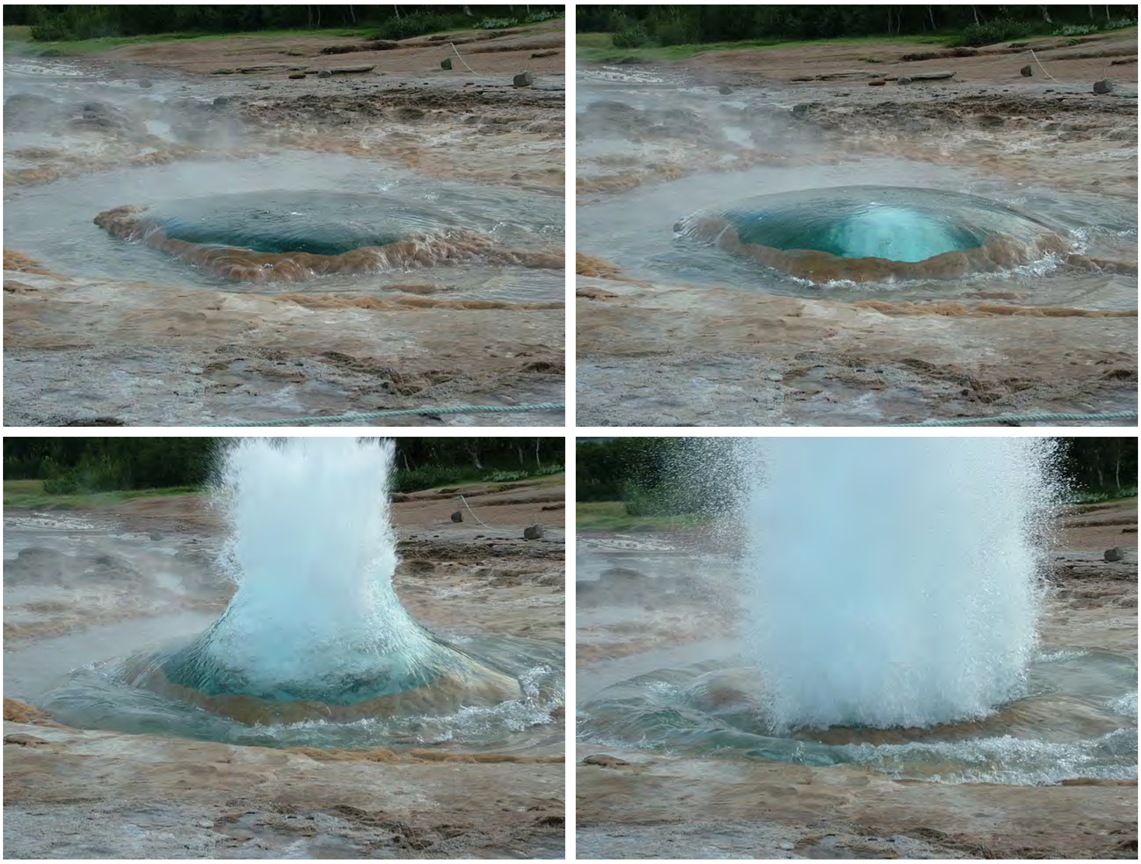

**Figure 1.4:** Strokkur geyser in the geothermic region near Hvítá River in Iceland erupts regularly every 4-8 minutes, after being unblocked in 1789 by an earthquake. Beside geysers, earthquakes ruptures are a common remote triggering mechanisms for mud pots, volcanoes, landslides, tsunamis and further seismicity.

through a conduit, resulting in a mud volcano on the surface, is then applied to the case of LUSI. We show that the conceptual and numerical model matches the observations on the one hand, and on the other hand allows conclusions on how changes in rheological properties of surrounding rock and fluid characteristics of the mud influence extrusion dynamics. When studying the long-term eruption behavior, flow cycles and decay factors provided by the model can be used to estimate the discharge rates and extruded volume, and help assess hazards for society and economics.

Chapter 4 provides an analysis of the $M_w = 6.3$ L'Aquila earthquake of April 6th 2009 and the correlation between its aftershock locations and the Coulomb failure stress change and dilatation, in order to identify the mechanisms driving the aftershock sequence. By comparing Coulomb stress changes and volumetric changes caused by various earthquake fault slip settings, the underlying aftershock trigger, i.e. whether static stress transfer (King et al., 1994) or dilatational effects (Sibson, 2007) drive aftershock sequences following the main shock, can be identified. We suggest fluid flow instead of stress transfer to be the main reason for the L'Aquila sequence, as high pressure fluids were already identified as aftershock driving mechanism for the 1997 Colfiorito sequence north of L'Aquila (Miller et al., 2004). The L'Aquila earthquake is very interesting for such an investigation, as the setting is located on a boundary of regions of diffuse $CO_2$ degassing and regions where degassing is not observed at all (Chiodini et al., 2004). Even though the focal mechanism of the main shock is consistent with the regional extensional tectonic setting (Walters

**Figure 1.5:** Laacher See in Germany is a caldera lake and a potentially active volcano, proven by seismic activities, thermal anomalies and carbon dioxide gas bubbling up from magma at the southeastern shore. A new eruption could result in a major disaster, especially because Germany is a heavily populated country and this caldera lies just 8 km from the Rhine river.

**Figure 1.6:** White Island is an active stratovolcano, situated offshore the North Island of New Zealand. Attempts on sulfur mining were stopped after the collapse of the western crater rim had created a lahar, killing 11 mining workers in 1914 (GNS, 2009).

et al., 2009), and the extensive aftershock sequences with more than 10,000 shallow events (Chiarabba et al., 2009; ISIDe, 2009) follow common earthquake decay laws (see section 4.2), the driving mechanism for the L'Aquila earthquake is not yet understood. Some proposed source models are consistent with regional changes in Coulomb stress, other fault geometry models deviate from these results (Anzidei et al., 2009; Cirella et al., 2009). Our investigation encompasses the influence of different fault geometries and slip scenarios for calculating and visualizing the impact of the $M_w = 6.3$ main shock on the regional stress field. Both map and cross-section views of the region are overlaid with aftershock data, and expected aftershock hazard regions are compared with real aftershock locations, in order to gain information about the mechanisms involved in the process. Furthermore, we analyze the statistical characteristics and possible spatiotemporal patterns of the aftershocks, to help to determine, whether the L'Aquila aftershock sequence can be explained by pure mechanical processes acting in the region or by the effects of trapped pressurized fluids at depth.

Chapter 5 merges the effects of a fluid pressure driven geohazard with the concomitant generation of earthquakes. We study cyclic seismicity associated with volcanic extrusion of a lava dome at Mount St. Helens (MSH). Since the explosive eruption of 18 May 1980 the intermittent activity of the volcano is increasingly investigated by volcanologists and seismologists. The renewed activity began with earthquake swarms of small magnitudes and the release of ash, steam plumes and magmatic gases on 23 September 2004. With the beginning of the continuous lava dome extrusion, earthquakes showed a remarkable periodicity of nearly $30 - 300$ s (Moran et al., 2008). Of course, earthquakes at volcanic settings are ubiquitous and are widely used for eruption forecasting. But the earthquake periodicity over a continuous period of 15 months indicates a persistent seismic source being present at a certain depth over an extended period, and can not be explained by conventional volcano models. Our approach is to improve upon a mechanistic model (Iverson et al., 2006) by considering the presence of fluids in the seismic source. We present a model to explain periodic earthquakes using Coulomb-type friction, concepts of effective stress and fluid pressure diffusion, with the periodicity controlled by fault gouge and fluid properties. The advantage of this formulation is that effects of degassing high pressure fluids exsolved by the magma body are incorporated into the problem, which allows the possibility to compare with observed $CO_2$ and $SO_2$ degassing events. The purpose is to set up one simplified model describing different observations and their impact on the environment by interrelating their underlying seismic and volcanic mechanisms.

Concluding remarks including an outlook on the further use of the presented models and results are given in the last chapter.

This thesis contributes to the physical understanding of fluid pressure related geohazards and their interaction in the upper 20 km of the crust. The considered cases and settings are prime examples of a diversified range of observed phenomena around the world. The models and techniques can be easily applied to other regions, and help in further developing intuition about the dominant physics controlling complex geological and geodynamical systems.

# Chapter 2

# Theoretical Background

The aim of this thesis is exploring and understanding natural systems where hydro-mechanical interactions play an important role. The theoretical and observational background for these studies are

1. mechanisms for developing fluid overpressures,
2. elasticity theory,
3. fluid mechanics, and
4. volcano-tectonic earthquakes and volcanic seismology.

In this chapter, we develop a brief theoretical review of each of these processes that form the basis of the subsequent chapters.

## 2.1 Mechanisms for developing overpressures

Fluid overpressure (in excess of hydrostatic pressure) occurs worldwide in a wide range of geological conditions, i.e. magmatic chambers, oil reservoirs, presumably at the base of seismogenic zones. Pore pressure is the in-situ pressure of fluids in the pores of subsurface formations. It equals the hydrostatic pressure, i.e. pressure exerted by a fluid at equilibrium due to the force of gravity, when the pore fluids only support the weight of overlying pore fluids (Carcione and Helle, 2002). This requires hydraulic connectivity to the free surface. Fluid overpressure can occur when the pore fluid reservoir becomes isolated from the free surface. From the basic pressure $p$ definition as force exerted normal to a control area $A$, the weight of a fluid column at depth can be calculated via

$$p(z) = \frac{1}{A}\int_{z_0}^{z} d\zeta \int\int_{A} d\xi \; d\upsilon \; \rho(\zeta) g(\zeta) = \int_{z_0} d\zeta \; \rho(\zeta) g(\zeta), \tag{2.1}$$

with density $\rho$, gravitational acceleration $g$, height of the test area $z$, height of the zero reference point of the pressure $z_0$ and variables of integration $\xi, \upsilon, \zeta$ (replacing

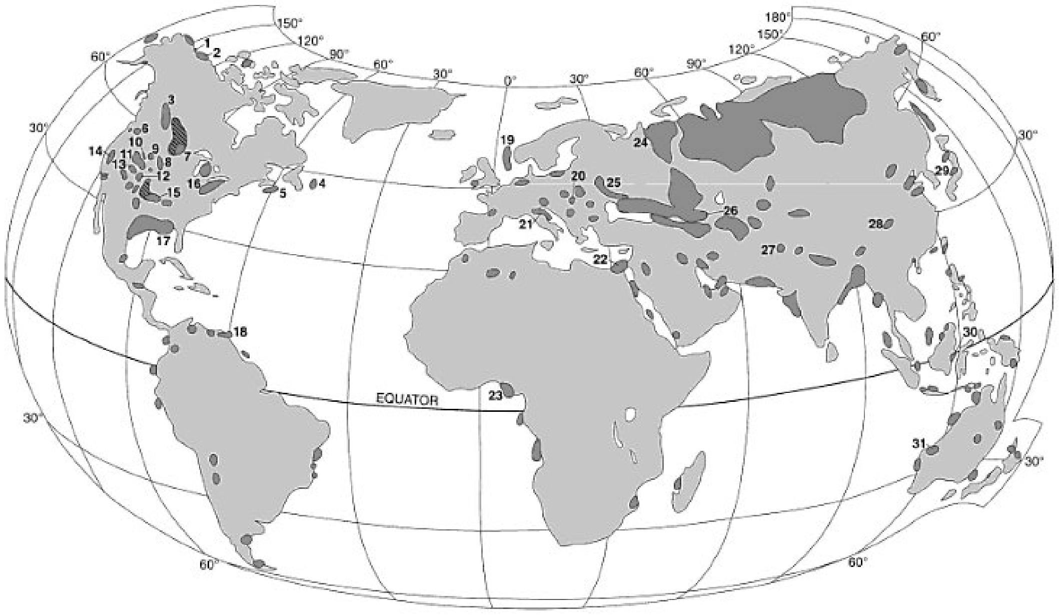

**Figure 2.1:** Global distribution of abnormal pressures (heavier shaded) taken from Law et al. (1998). The index numbers refer to selected attributes of abnormally pressured regions of the world given in the same source (e.g. no. 21 Italy, no. 30 Indonesia).

the Cartesian coordinates $x, y, z$ inside integrals) (Bar-Meir, 2010). Assuming a constant density throughout the fluid and neglecting the variation of $g$ since the height $h = z - z_0$ is negligible compared to the radius of the Earth, Equation (2.1) simplifies to

$$p = \rho g h. \tag{2.2}$$

The density distribution for the lithostatic or confining pressure due to the weight of overlying rock including pore fluids cannot be ignored. Therefore the formula is mostly given by

$$p(z) = p_{z_0} + g \int_{z_0}^{z} \rho(\zeta)\, d\zeta \tag{2.3}$$

with $p_{z_0}$ the pressure at the zero reference point. Formations at depth are said to be overpressurized when their pore pressure significantly exceeds hydrostatic pressure. In that case, we call the difference between confining pressure and pore pressure differential pressure.

There are numerous processes that can result in excess fluid pressure at depth:

1. Stress-related mechanisms including compaction, diagenesis, and tectonic loading that leads to pore volume decreases;
2. Fluid sources from devolatilizing and decarbonizing reactions, hydrocarbon generation and hydrothermal expansion;

3. Fluid flow (hydraulic head and osmosis) and buoyancy effects from density contrasts;
4. Redistribution of overpressurized fluids.

The dominant causes for overpressure in the crust are the first two listed, i.e. stress-related and volumetric processes (Law et al., 1998). Increasing stress on a rock causes a reduction of the total bulk volume of the material $V_T$ including the effective volume of the pores $V_V$ (void-space), and forces out the enclosed fluids, i.e. liquids (water or hydrocarbons) that were trapped in the pores during the sediment deposit. This process, called lithification, converts unconsolidated sediments into sedimentary rocks and is responsible for porosity destruction through compaction, where porosity is the ratio between the total bulk volume and the volume of the void-space

$$\varphi = \frac{V_V}{V_T}. \tag{2.4}$$

Furthermore, rocks can liberate fluids like $H_2O$ and $CO_2$ under certain pressure-temperature conditions, or $CH_4$ from biological reactions. This solid-state mineralogy change is called diagenesis. At higher temperatures, e.g. at deeper levels, the recrystallization is called metamorphism and its causes include orogenic events, like the collision and/or subduction of tectonic plates (regional metamorphism), magma

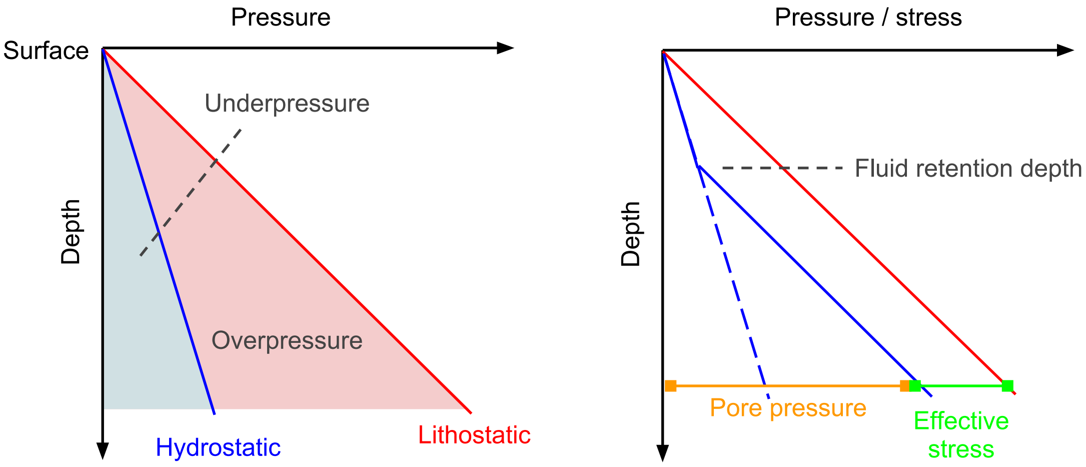

**Figure 2.2:** Left: Pressure versus depth plots for uniform density and gravity distributions. Rocks with pressure plots between the hydrostatic (blue) and lithostatic (red) gradients are termed overpressurized. Right: Pressure and/or stress versus depth plot for overpressure generated by disequilibrium compaction. Fluid retention occurs at depth where the permeability and sedimentation rate combine to prevent complete dewatering. Below the fluid retention depth the profile changes to almost constant effective stress (green), i.e. a pressure profile almost parallel to the lithostatic pressure gradient. Figure adopted from Law et al. (1998).

intrusion into colder surrounding rock (contact metamorphism) and frictional heat in fault zones (dynamic metamorphism) (Okrusch and Matthes, 2010). Both mechanisms, diagenesis and metamorphism, lead to fluid expulsion. But non-equilibrium in compaction, like fast loading or rapid deposition, and restricted rates of fluid transport due to low permeability materials result in elevated fluid pressures. Permeability describes the ability of a porous material to transmit fluids and is defined as the proportionality constant $k$ in Darcy's Law

$$v = \frac{k}{\eta}\frac{dp}{dx}, \tag{2.5}$$

where $v$ is the Darcy velocity, $\eta$ the dynamic viscosity of the fluid and $\frac{dp}{dx}$ the pressure gradient that enables flow from high to low pressures over the distance $x$. Thus, materials with fine grains and low permeabilities, like silts and clays, act as seals for fluid flow. Compared to equilibrium compaction within the sediment column and to cases of absent geological seals, where permeable materials allow fluids to escape from their pores, the trapped fluids bear a greater proportion of the load that would be held by grain contacts and higher pore pressures develop in the pore-space (Rubey and Huppert, 1959). This causes a decrease in the stress acting on the rock reference frame and is known as Terzaghi's principle of effective stress, which plays an important role in earthquake processes. A detailed discussion on this topic is given in section 2.2.

High pressure fluid compartments in the crust can be subdivided into those characterized by large volumes of low permeability rock and those bounded by seals formed by a combination of low permeability effects and high capillarity pressure due to the interfacial tension between two fluids (Iverson et al., 1994). If the reservoir is sealed

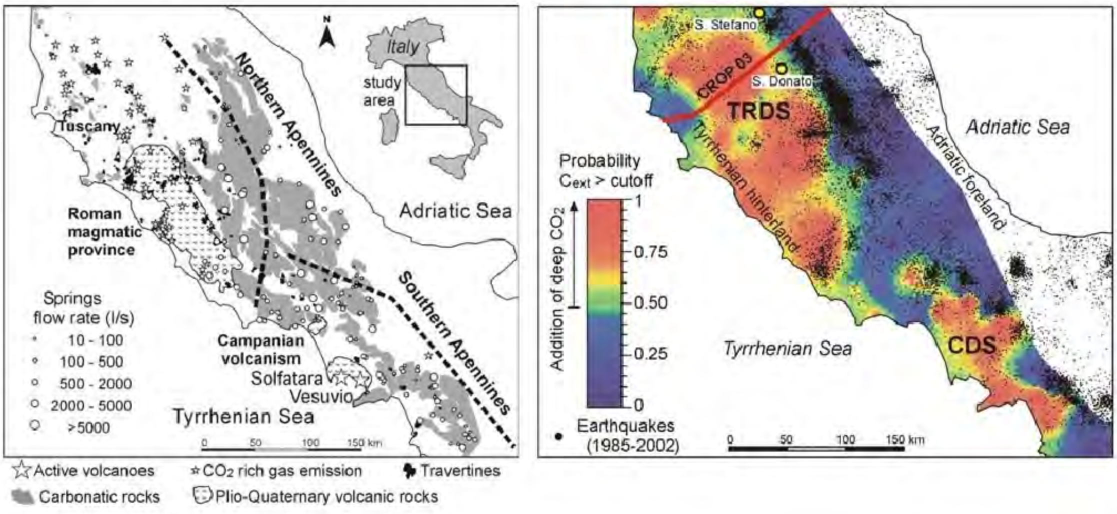
N
Italy
study area
Tuscany
Northern Apennines
Adriatic Sea
Roman magmatic province
Springs flow rate (l/s)
10 - 100
100 - 500
500 - 2000
2000 - 5000
>5000
Campanian volcanism
Solfatara
Vesuvio
Southern Apennines
Tyrrhenian Sea
0 50 100 150 km
Active volcanoes
CO2 rich gas emission
Travertines
Carbonatic rocks
Plio-Quaternary volcanic rocks
S. Stefano
CROP 03
S. Donato
TRDS
Adriatic Sea
Adriatic foreland
Tyrrhenian hinterland
Probability Cext > cutoff
Addition of deep CO2
1
0.75
0.50
0.25
0
Tyrrhenian Sea
CDS
Earthquakes (1985-2002)
0 50 100 150 km

**Figure 2.3:** Left: Location map of earth degassing processes in central south Italy. Right: Map showing the probability that a deep source of carbon is present at any location, compared with seismic activity. Figures taken from Chiodini et al. (2004). For more details we refer to captions and text given therein.

on all sides by an impermeable shale or limestone, the condition of a closed system holds. Any disturbance to the system (be it a natural effect or human action), caused by creating cracks, fractures or other ways towards the surface, results in pressure gradients and the escape of trapped fluids. The subsequent fluid flow to the surface may result in natural hazards like mud volcanoes or limnic eruptions.

Predicting overpressures at depth using Darcy's law are affected by the choice of the constitutive relations between porosity, permeability and effective stress. In exploration engineering, the knowledge of pressure distributions at depth is very important for predicting hydrocarbon reservoir locations, for drilling safety to prevent blowouts, and for optimizing the recovery rate (Dutta et al., 2002). An example of unexpected overpressure zones is the LUSI mud volcano, Indonesia, which may have been initiated by drilling in May 2006 (Manga et al., 2009). High pressure fluids can also play an important role for seismogenesis. In the Apennines, Italy, large $CO_2$ degassing areas, fed by a deep, mantle-related source associated with a subduction zone (Chiodini et al., 2004), coincide with earthquake locations (see Figure 2.3) and have been shown using numerical models to play a role in seismogenesis in the region (Collettini, 2002; Miller et al., 2004).

These examples are just two of a variety of geophysical consequences associated with overpressure. The worldwide occurrence reflects the need for analyzing these events, as understanding one process can help to improve models for detecting the presence of fluids, to develop simulations for predicting their escape from sedimentary basins at depth, and to assess risk from buried, high pressure reservoirs.

## 2.2 Stress-weakening in earthquakes and faulting

In mechanics and elasticity, stress $\sigma$ is defined as the ratio of an external deforming force applied to a body to the area over which it is applied $\frac{F}{A}$. We distinguish between perpendicular and tangential forces to the surface, leading to normal stresses and shear stresses. The stress is composed of both components, therefore it is necessary not to define the stress over a given area but at a specific point in the body (Bar-Meir, 2010). Cauchy considered a small parallelepiped being stressed by an external force and resolved the stresses on each face into components of a Cartesian coordinate system $(x, y, z)$ (Figure 2.4).

According to this concept, the stress at any point of a body is defined by the second order tensor

$$\sigma = \begin{pmatrix} \sigma_{xx} & \tau_{xy} & \tau_{xz} \\ \tau_{yx} & \sigma_{yy} & \tau_{yz} \\ \tau_{zx} & \tau_{yz} & \sigma_{zz} \end{pmatrix} \tag{2.6}$$

with normal stresses $\sigma_{ij}$, $i = j$ and shear stresses $\tau_{ij}$, $i \neq j$. In static equilibrium, the stresses on opposite faces of the body must equal, leading to symmetry of the shear components of the stress tensor with $\tau_{ij} = \tau_{ji}$. The components of the stress tensor depend on the orientation of the coordinate system, but as a physical quantity,

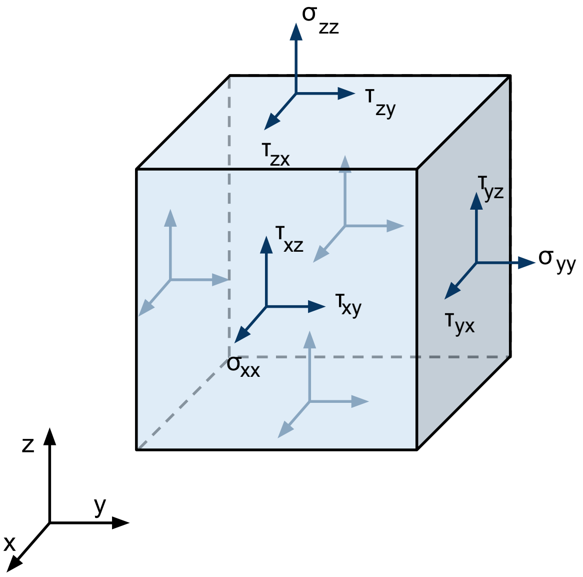

**Figure 2.4:** The stresses on the surfaces of an infinitesimal small control volume. $\sigma_{xx}, \sigma_{yy}, \sigma_{zz}$ are normal stresses, $\tau_{ij}, i, j = x, y, z, i \neq j$ indicate shear stresses.

the stress tensor is independent of the chosen coordinate system. At each point in a stressed body there are at least three planes, termed principal planes, with normal vectors $\vec{n}$, called principal directions, where the corresponding stress vector is perpendicular to the plane and where there are no normal shear stresses. These stresses, being normal to the principal planes, are called principal stresses and are determined as eigenvalues $\sigma_1$, $\sigma_2$ and $\sigma_3$ (with $\sigma_1 \geq \sigma_2 \geq \sigma_3$) of the stress tensor. Their direction vectors $\vec{n}$ are the principal directions or eigenvectors. A graphical representation of the state of stress at a point of a body is given by Mohr's circle (Figure 2.5), where the circumference of the circle is the locus of points that represent the state of stress on individual planes at all their orientations. The sign convention is that compressional stresses are positive while tensile (or extensional) stresses are negative.

When a body is subjected to stresses, it deforms, and the resulting relative change in the size and the shape of that body is called strain $\varepsilon$. Normal strains $\varepsilon_{ij}$, $i = j$ describe changes in size along the axes of the coordinate system $(x, y, z)$, and shear strains $\varepsilon_{ij}$, $i \neq j$ measure the change in shape of the body. Thus, normal strains produce dilatation (expansion in bulk) or compressions, and shear strains are responsible for rotations. Altogether, strain is a dimensionless, symmetrical tensor quantity

$$\varepsilon = \begin{pmatrix} \varepsilon_{xx} & \varepsilon_{xy} & \varepsilon_{xz} \\ \varepsilon_{yx} & \varepsilon_{yy} & \varepsilon_{yz} \\ \varepsilon_{zx} & \varepsilon_{zy} & \varepsilon_{zz} \end{pmatrix} = \begin{pmatrix} \frac{\partial u_x}{\partial x} & \frac{1}{2}\left(\frac{\partial u_x}{\partial y} + \frac{\partial u_y}{\partial x}\right) & \frac{1}{2}\left(\frac{\partial u_x}{\partial z} + \frac{\partial u_z}{\partial x}\right) \\ \frac{1}{2}\left(\frac{\partial u_x}{\partial y} + \frac{\partial u_y}{\partial x}\right) & \frac{\partial u_y}{\partial y} & \frac{1}{2}\left(\frac{\partial u_y}{\partial z} + \frac{\partial u_z}{\partial y}\right) \\ \frac{1}{2}\left(\frac{\partial u_x}{\partial z} + \frac{\partial u_z}{\partial x}\right) & \frac{1}{2}\left(\frac{\partial u_y}{\partial z} + \frac{\partial u_z}{\partial y}\right) & \frac{\partial u_z}{\partial z} \end{pmatrix}, \quad (2.7)$$

with displacements $u_x$, $u_y$ and $u_z$ in $x$, $y$ and $z$ direction. For elastic materials, stress and strain are proportional:

$$\sigma_{ij} = C_{ijkl}\varepsilon_{kl}. \tag{2.8}$$

The proportionality constant $C_{ijkl}$ is the elasticity tensor, a forth order tensor with 81 components, which reduce to two elastic constants (i.e. Young's modulus (tendency of an object to deform along an axis when opposing forces are applied along that axis), Poisson's ratio (tendency to expand in the other two directions perpendicular to the direction of compression), bulk modulus (tendency to deform in all directions when uniformly loaded in all directions) and shear modulus (tendency to shear when acted upon by opposing forces)) for an isotropic, homogeneous material.

In the lithosphere, the relative motion of tectonic plates is responsible for the build-up of stresses, and the direction of the stresses is correlated with this plate motion. When a critical stress state is reached in a region due to compression or extension, depending on the acting tectonic forces, the strength threshold is exceeded and the accumulated potential energy is released. The rock breaks and fractures are created (Fowler, 2005). Planar fractures are termed faults, and the rapid movement of the two sides of a preexisting fault, the hanging wall and foot wall, is the origin of earthquakes. The standard equations for shear stress $\tau$ and normal stress $\sigma_n$ acting on a plane lying at an angle $\theta$ to the major principle stress $\sigma_1$ are

$$\tau = \frac{1}{2}(\sigma_1 - \sigma_3)\sin 2\theta \tag{2.9}$$

$$\sigma_n = \frac{1}{2}\left((\sigma_1 + \sigma_3) - (\sigma_1 - \sigma_3)\cos 2\theta\right), \tag{2.10}$$

with least principle stress $\sigma_3$ (Gowd , 2004). Therefore, the Cauchy stress tensor and its representation in Mohr's circle is commonly used in earthquake mechanics.

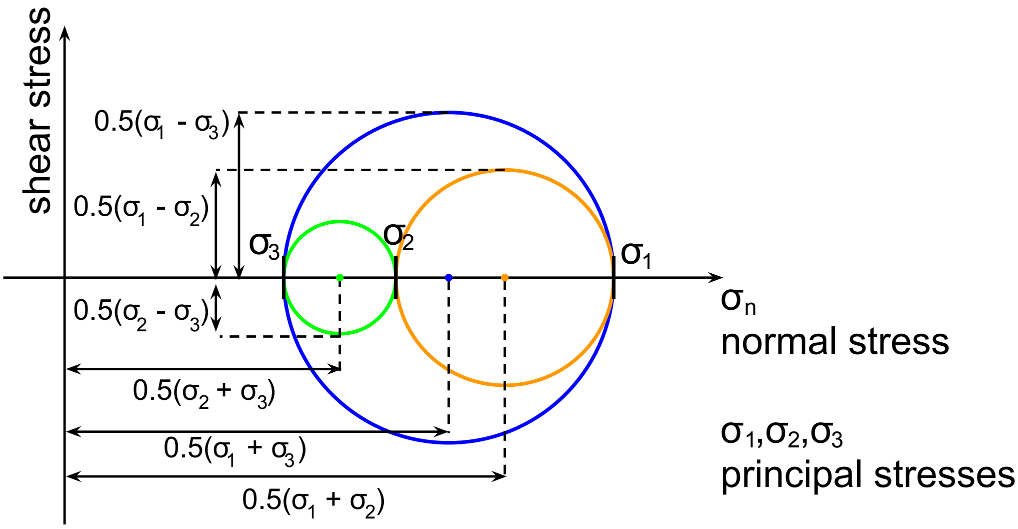

**Figure 2.5:** Mohr's circle for a three-dimensional state of stress. $\sigma_1$ is the maximum, $\sigma_3$ the minimum principle stress and $\sigma_2$ lies in between.

In compressional settings, the maximum principal stress $\sigma_1$ acts horizontally, while $\sigma_3 = \rho gh$ is the constant, vertical lithostatic load. Faults occurring in these settings are called thrust faults. In the opposite case, extensional regions are characterized by vertical maximum principle stress $\sigma_1 = \rho gh$ (constant) and decreasing minimum principle stress $\sigma_3$. Faults in these settings are called normal faults. The third possibility arises from $\sigma_2 = \rho gh$, i.e. when the vertical stress is the intermediate principle stress. In this case called strike-slip faulting, faulting occurs either when $\sigma_3$ is reduced (for $\sigma_1$ slightly greater than $\sigma_2$) or $\sigma_1$ is increased (if $\sigma_3$ is only slightly less than $\sigma_2$). The frictional strength $\tau$ of an existing fault is given by the Coulomb criterion

$$\tau = c_0 + \mu\sigma_n, \tag{2.11}$$

where $c_0$ is the cohesion strength of the fault and $\mu = \tan\theta$ is the coefficient of frictional sliding with angle of internal friction $\theta$. This relationship describes the ability of a fault to oppose stress with its internal friction from shearing. In Mohr's graphical representation, the Coulomb criterion is a linear slope, and a fault failure, i.e. an earthquake, occurs when the stress state on some fault reaches the failure condition. Therefore, from a tectonic point of view, there are three possibilities for earthquake generation: the increase of $\sigma_1$ in compressional regions, the decrease in $\sigma_3$ in tensional settings and strike-slip faulting for $\sigma_3 < \rho gh < \sigma_1$. Figure 2.6 shows that higher shear stresses $\tau$ are necessary for thrust fault failure than for normal fault failure, possibly contributing higher magnitude earthquakes in compressional regions.

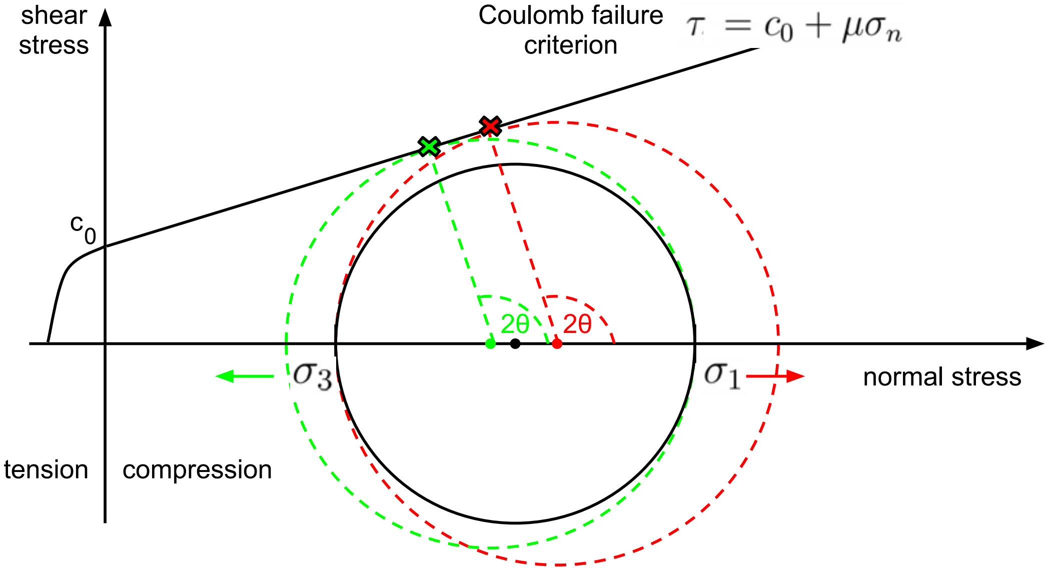

**Figure 2.6:** Mohr's circle and Coulomb failure curve. The circle increases, when increasing $\sigma_1$ or decreasing $\sigma_3$ while remaining the other constant, and hits the Coulomb failure criterion. The frictional strength of the fault is exceeded and an earthquake occurs.

The Terzaghi principle of effective stress

$$\sigma_{\text{eff}} = \sigma_n - p, \tag{2.12}$$

states that when a rock is subjected to a stress, it is opposed by the fluid pressure of pores in the rock (Terzaghi, 1943). As a consequence, increasing the pore pressure $p$ while keeping the maximum and minimum regional stresses $\sigma_1$ and $\sigma_3$ constant offers another possibility for rock failure. In the graphical representation, Mohr's circle moves left and reaches the Coulomb failure criterion curve at lower shear stresses (see Figure 2.7). Therefore the role of fluids in stress weakening and earthquake generation is crucial.

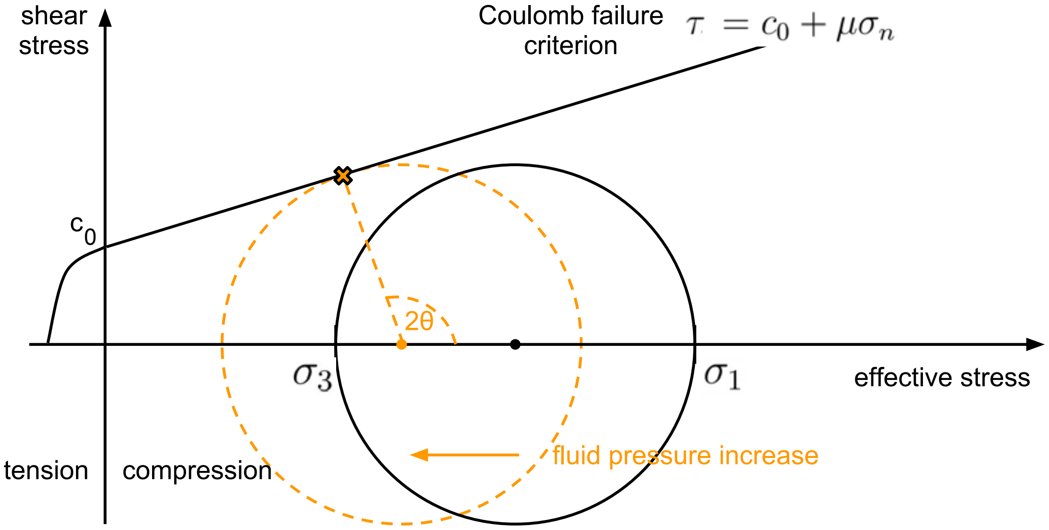

**Figure 2.7:** Mohr's circle and Coulomb failure curve for effective stress $\sigma_{\text{eff}}$. The circle moves when increasing pore pressure $p$ while remaining the other stresses constant, and hits the Coulomb failure criterion. The frictional strength of the fault is exceeded and an earthquake occurs at lower shear stresses $\tau$.

When an earthquake occurs, the average value of the shear stress is reduced on the fault that slipped, but at the same time shear stress rises near the fault tips. Additionally, strain is caused, i.e. the crust material is subjected to either dilatation or compression. The spatial extent of the crustal deformation and surface displacement can be measured by geodetic satellites (InSAR, GPS). Thus, the relief of built-up stresses along a fault during an earthquake leads to a redistribution of stress states in the surrounding region. The process is known as Coulomb stress transfer, or Coulomb failure stress change

$$\Delta CFS = \Delta\tau + \mu\Delta\sigma_n. \tag{2.13}$$

The interaction of earthquakes and aftershock generation due to off-fault failure is encouraged if $\Delta CFS$ is positive and discouraged if it is negative. A major shortcoming in the use of $\Delta CFS$ measures to predict future earthquakes is the unknown level of stress changes needed for triggering. But many aftershock triggering processes related to reactivation of inactive faults have been associated with very small stress changes, mostly just a few percent of the mean main shock stress drop (King et al., 1994; Toda et al., 2002). Nevertheless, the analysis of static stress changes from large events by calculating $\Delta CFS$ is a common and important physics-based foundation for the probabilistic earthquake hazard forecast. The USGS Coulomb 3.1 software allows a straightforward calculation of $\Delta CFS$ (see A.2). Equation (2.13) can be completed by the pore pressure change $\Delta p$ to obtain $\Delta CFS = \Delta\tau + \mu(\Delta\sigma_n + \Delta p)$ encouraged by Terzaghi's principle of effective stress (2.12), but the influence of fluid pressure is mostly neglected in stress transfer analyses (Lin and Stein, 2004; Toda et al., 2005).

## 2.3 The nature of high-pressure fluid flow

Fluid mechanics deals with the study of fluids under static and dynamic situations. As a branch of continuum mechanics, it deals with the relationship between forces, motions, and statical conditions in continuous material, and the study involves many fields that have no clear boundary between them. For example, we distinguish between laminar flow and turbulent flow, or single phase flow and multiphase flow, but as the discipline of fluid mechanics is extensive, arbitrary assumptions in some fields are common, and in certain cases, where one principle is more relevant than the other, effects are neglected (Bar-Meir, 2010). In this section we limit ourselves to definitions, properties and methods that are important for chapters that follow. For further fundamental principles needed for studying the complexity of fluid flow we refer to standard works for mechanics and thermodynamics.

The simplest situation that can occur in the study of fluids is when fluid is at rest. Under the presence of a shear stress, a fluid cannot remain at rest but exerts pressure normal to any contacting surface. From the principles of equilibrium for each point in the fluid thought of as an infinitesimally small cube it follows that the pressure on every side of this unit of fluid must be equal (isotropic pressure). Otherwise, the fluid would move in the direction of the resulting force. Due to gravity, fluids at equilibrium exert pressure known as hydrostatic pressure, which is calculated from Equation (2.1) given before in section 2.1.

The basic assumption that must be satisfied when dealing with fluid dynamics is the continuum assumption (Batchelor , 2000; Oran and Boris, 2000): Although composed of molecules that collide with one another and with solid objects, the continuum assumption considers fluids to be continuous. The fact that the fluid is made up of discrete molecules is ignored. Consequently, properties such as velocity, pressure, density and temperature are taken to be well-defined at infinitesimally small points, are assumed to vary continuously from one point to another, to be averaged values in the reference volume or control volume and to be differentiable. The continuity equation describes the transport of conserved quantities and is the local form of the conservation laws of fluid mass, linear momentum and energy. The assumption that mass is conserved implies that for any closed isolated system with finite control volume the rate of mass entering a system must be the same as the rate at which mass leaves, and thus will remain constant over time (see Figure 2.8). Generalized to all conservation laws, the Reynolds transport theorem states that the sum of changes of some property defined over a control volume must be equal to what is lost or gained through the boundaries of the volume plus what is created or consumed by sources and sinks inside the control volume. The differential form of the fluid dynamics mass continuity equation for a single phase is

$$\frac{\partial \rho}{\partial t} + \nabla \cdot (\rho \mathbf{v}) = 0, \tag{2.14}$$

where $\rho$ is fluid density, $t$ time, $\mathbf{v}$ the flow velocity vector field and $\nabla = (\frac{\partial}{\partial x}, \frac{\partial}{\partial y}, \frac{\partial}{\partial z})$ the vector differential operator for the three-dimensional Cartesian coordinate system with coordinates $(x, y, z)$. Here $\nabla \cdot$ gives the divergence, i.e. the vector operator that measures the magnitude of a vector field's source or sink at a given point in terms of a signed scalar. For the case of steady-state, the mass balance reduces to

$$\nabla \cdot (\rho \mathbf{v}) = 0, \tag{2.15}$$

and if the fluid is incompressible, we get $\nabla \cdot \mathbf{v} = 0$, where compressibility $\beta$ (or its reverse the bulk modulus), as the measure of the relative volume $V$ change of a fluid as a response to a pressure $p$ (or mean stress) change, is given as

$$\beta = -\frac{1}{V}\frac{\partial V}{\partial p}. \tag{2.16}$$

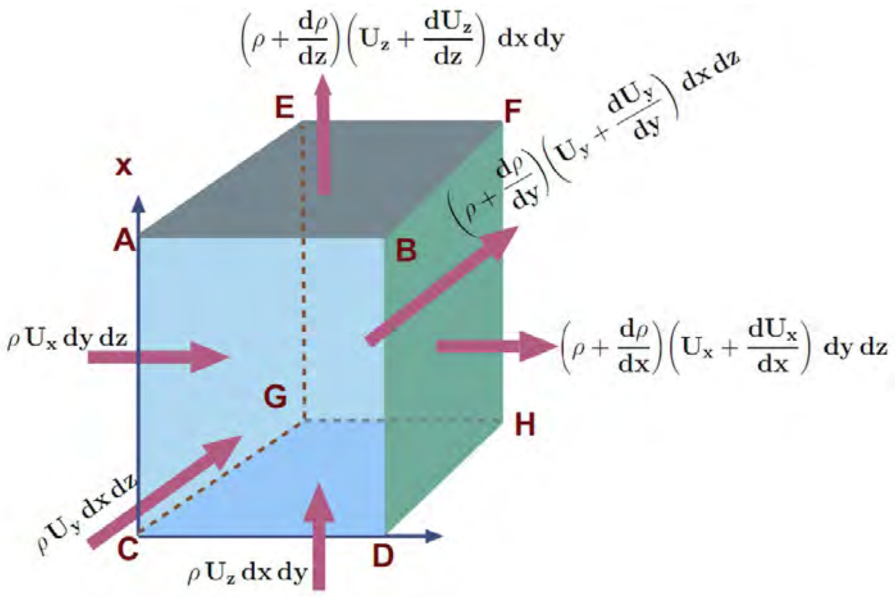
$\left(\rho + \frac{d\rho}{dz}\right)\left(U_z + \frac{dU_z}{dz}\right) dx\, dy$
E
F
$\left(\rho + \frac{d\rho}{dy}\right)\left(U_y + \frac{dU_y}{dy}\right) dx\, dz$
x
A
B
$\rho U_x\, dy\, dz$
$\left(\rho + \frac{d\rho}{dx}\right)\left(U_x + \frac{dU_x}{dx}\right) dy\, dz$
G
H
$\rho U_y\, dx\, dz$
C
$\rho U_z\, dx\, dy$
D

**Figure 2.8:** The mass balance in Cartesian coordinates on the infinitesimal control volume. Figure taken from Bar-Meir (2010, p. 228).

The conservation of linear momentum for fluid dynamics is derived from Newton's Second Law of Motion and is given by the general form of the Navier-Stokes equation

$$\rho\left(\frac{\partial \mathbf{v}}{\partial t}+\mathbf{v}\cdot\nabla\mathbf{v}\right)=-\nabla p+\nabla\cdot\mathbb{T}+\mathbf{f} \tag{2.17}$$

with $t$, $\mathbf{v}$, $\rho$, $\nabla\cdot$ as given before and $p$ pressure, $\mathbf{f}$ body forces per unit volume acting on the fluid (such as gravity $\mathbf{f}=\rho g$) and $\nabla$ the gradient, i.e. the vector derivative, of a scalar field. $\mathbb{T}$ gives the deviatoric stress tensor, as the stress tensor $\sigma_{ij}$ can be expressed as sum of a mean hydrostatic stress tensor (or volumetric stress tensor), which tends to change the volume of a stressed body, and a deviatoric component, which tends to distort it:

$$\begin{aligned}\sigma_{ij}&=\begin{pmatrix}\sigma_{xx}&\tau_{xy}&\tau_{xz}\\ \tau_{yx}&\sigma_{yy}&\tau_{yz}\\ \tau_{zx}&\tau_{yz}&\sigma_{zz}\end{pmatrix}\\ &=-\begin{pmatrix}p&0&0\\0&p&0\\0&0&p\end{pmatrix}+\begin{pmatrix}\sigma_{xx}+p&\tau_{xy}&\tau_{xz}\\ \tau_{yx}&\sigma_{yy}+p&\tau_{yz}\\ \tau_{zx}&\tau_{yz}&\sigma_{zz}+p\end{pmatrix}\\ &=-p\mathbb{I}+\mathbb{T},\end{aligned} \tag{2.18}$$

where $\sigma_{ij}$, $i=j$ are normal stresses, $\tau_{ij}$, $i\neq j$ are shear stresses and $\mathbb{I}$ is the $3\times 3$ identity matrix. Thus, the left hand side of Equation (2.17) describes acceleration, and may be composed of time dependent or convective effects, while the right hand side is summation of body forces and derivatives of stress (pressure and shear stress). In addition, an equation for the conservation of energy is needed:

$$\rho\left(\frac{\partial H}{\partial t}+H\cdot\nabla H\right)=\frac{\partial p}{\partial t}+p\cdot\nabla p+\nabla\cdot(k\nabla T)+\Lambda. \tag{2.19}$$

Here $H$ is the enthalpy (total energy of a thermodynamic system), $T$ is the temperature, $\Lambda$ is a function representing the dissipation of energy due to viscous effects, and $k$ is Boltzmann's constant relating temperature and energy via the ideal gas law ($N$ is the number of particles in the gas)

$$pV=NkT, \tag{2.20}$$

used as equation of state.

This system of equations together with functions for the dependence of parameters (such as viscosity) on the variables can describe the dynamics of all known gases and most liquids. But in general, simplifications can be applied in order to be able to solve the Navier-Stokes equation. Assumptions, mostly based on observations on the specific behavior of a fluid, are made and applied in order to simplify the stresses in terms of the other flow variables, such as velocity and density. For example, for a fluid at rest, $\nabla\cdot\mathbb{T}$ must be zero in Equation (2.17) so that hydrostatic pressure results. Or, for an incompressible flow of a Newtonian fluid, the deviatoric stress

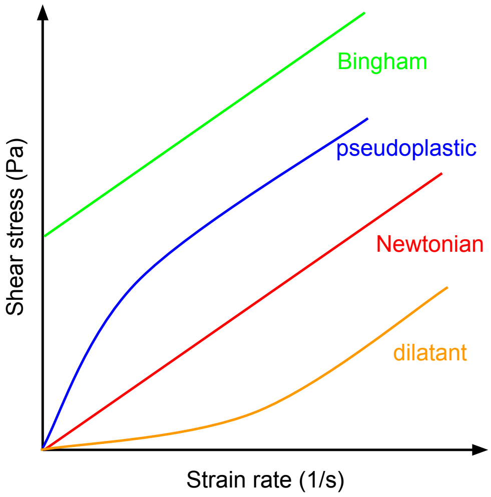

**Figure 2.9:** Illustration (no scale) of the shear stress $\tau$ versus strain rate $\dot{\varepsilon}$ behavior for Newtonian and non-Newtonian fluid properties.

tensor $\nabla \cdot \mathbb{T}$ can be replaced with $\mu \nabla^2 \mathbf{v}$, with $\mu$ constant dynamic viscosity and $\nabla^2$ the vector Laplace operator, while for compressible Newtonian fluids, estimations on $\nabla \cdot \mathbb{T}$ result in

$$\rho \left( \frac{\partial \mathbf{v}}{\partial t} + \mathbf{v} \cdot \nabla \mathbf{v} \right) = -\nabla p + \nabla \cdot (\mu \cdot (\nabla \mathbf{v} + (\nabla \mathbf{v})^T)) + \nabla(\lambda \nabla \cdot \mathbf{v}) + \mathbf{f}, \tag{2.21}$$

with dynamic viscosity $\mu$ and the second coefficient of viscosity $\lambda$, which produces a viscous effect associated with volume change (bulk viscosity). Here,

- flow is called incompressible (or isochoric), when the material density is constant within an infinitesimal volume that moves with the velocity of the fluid, and

- a fluid is called Newtonian, when the shear stress $\tau$ exerted by the fluid (drag) versus strain rate $\dot{\varepsilon} = \frac{dv}{dx}$ (or velocity gradient perpendicular to the direction of shear) curve for a fluid is linear and passes through the origin

  $$\tau = \mu \frac{dv}{dx} \tag{2.22}$$

  with viscosity $\mu$ as proportionality constant. (A Bingham Plastic fluid, i.e. a material that behaves elastically as a rigid body at low stresses but flows as a viscous fluid and behaves plastically when reaching the yield stress, is an example for the several types of non-Newtonian fluids and is not discussed in detail.)

Note that the incompressible flow assumption often holds even when dealing with compressible fluids (Oran and Boris, 2000).

There are many further methods to specify the deviatoric stress tensor in Equation (2.17). Last mentioned, a widely-used condition for cylindrical flow is the Poiseuille condition

$$\Delta p = \frac{8\pi\mu\mathbf{v}}{A}. \tag{2.23}$$

It describes the pressure drop $\Delta p$ in a laminar viscous and incompressible fluid flowing through a cylindrical pipe with constant cross-section $A$ that is essentially longer than its diameter. Laminar flow occurs when a fluid flows in parallel layers, with no disruption between the layers (Batchelor , 2000). It is the opposite of turbulent flow which occurs at higher velocities where eddies (swirling of a fluid) or small packets of fluid particles form leading to lateral mixing (Figure 2.10).

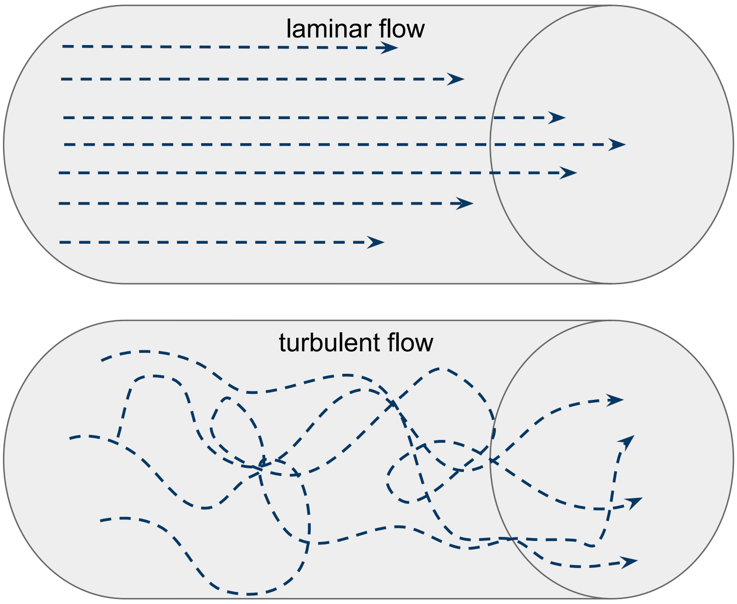

**Figure 2.10:** Illustration of laminar and turbulent flows through a cylindrical pipe. For laminar viscous flows the Poiseuille flow condition (2.23) holds.

More simplifications include

- the ideal fluid assumption with zero viscosity, where - as a consequence - the acceleration (the rate of change of velocity) is proportional to the derivative of internal pressure, or
- the isothermal assumption, where temperature can be ignored.

When changes with position can be ignored, the partial differential form simplifies to an ordinary differential equation or linear expressions. But in general, the equations describing fluid dynamics are non-linear differential equations and can just be solved numerically by applying appropriate boundary conditions and initial values. These conditions describe physical situations that are believed or should exist and can be categorized by the velocity, pressure, or in more general terms as the shear stress conditions.

However, many fluid dynamic problems from geosciences do not allow simplifications. An important aspect for geophysical modeling is the topic of multi-phase flow: Calculations of many kinds of flow deal with more than one phase or material. In volcanic eruptions for example, the melt and exsolved gas can be handled as two separated phases for certain dynamical investigations (Barmin et al., 2002; Melnik and Sparks, 1999, 2005), or as one phase with inhomogeneous material properties, which is very difficult to handle. Thus multi-phase flows require solving a whole system of equations, consisting of the conservation law for the total system as well as of the conservation law for each of the system's components (solid, liquid and gaseous components), and furthermore, of characteristics describing their interaction. Additional forces, like the buoyancy force and the drag force in solid-liquid flows, must be considered as they can accelerate the flow or reduce its speed.

The complexity of a given fluid dynamical problem is the crucial factor when choosing the modeling approach. The two basic approaches for describing fluid flows for applications in geosciences are either taking the Navier-Stokes equation with appropriate boundary conditions or deriving the whole set of governing equations from the fundamental conservation laws for mass, momentum and energy. The second method may seem circuitous, but it assures that the resulting system of equations is physically sound and can be easily reproduced and transfered to other real world problems.

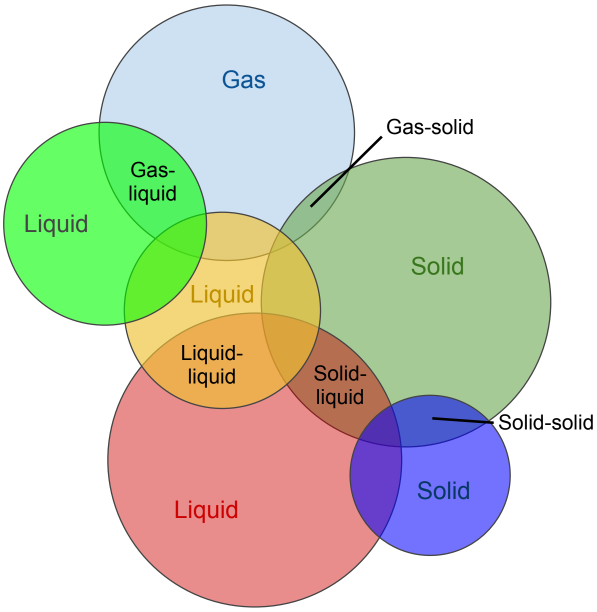

**Figure 2.11:** Illustration of multi-phase flows. Gas-liquid, liquid-liquid and liquid-solid flows occur very often in geoscientific settings.

## 2.4 Earthquakes at volcanic settings

The simultaneous occurrence of earthquakes and volcanoes provides the foundation for studies of interactions between seismicity and volcanic eruptions. The interaction modes are generally based on dynamic stress triggering, viscoelastic stress triggering and static stress triggering (Harris, 1998).

Models for dynamic stress triggering include hydraulic surge of high-pressure fluids from the plastic crust into the fracture mesh of the brittle crust, relaxing magma body either by cooling or by partial melting of previously solid matrix supporting accumulating tectonic stresses in the region, and excitation of volatile bubbles through advective overpressure, rectified diffusion (Brodsky et al., 1998) or convection of crystal-rich and crystal-poor magma. Viscoelastic relaxation of shear stresses in the upper mantle and lower crust that were induced by a redistribution of stresses during an earthquake or due to changing pressure conditions in a magma chamber,

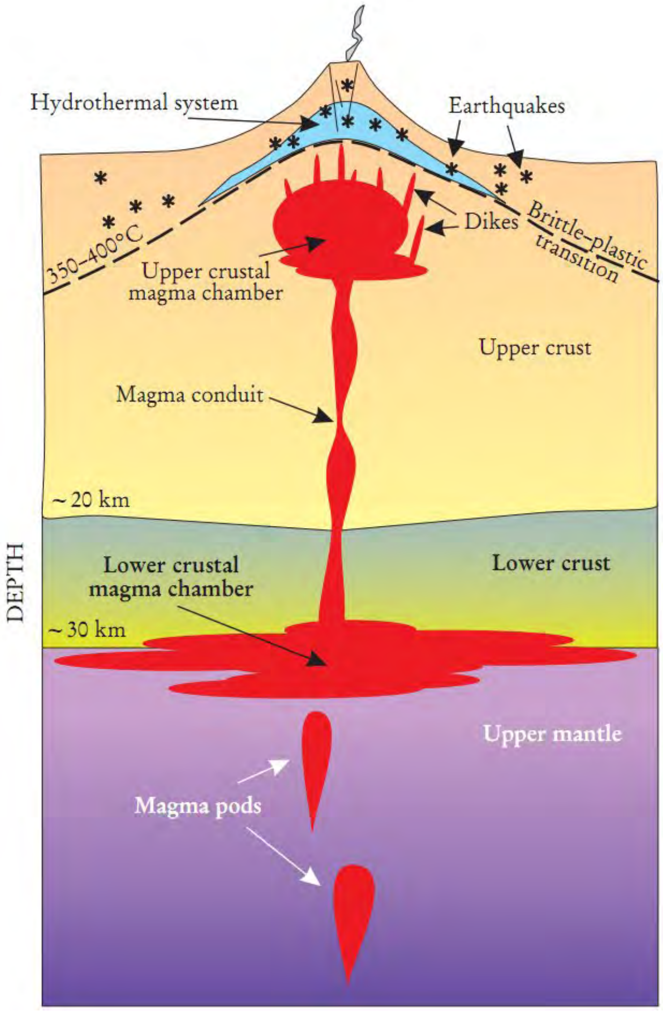
Hydrothermal system
Earthquakes
350–400°C
Dikes
Brittle–plastic transition
Upper crustal magma chamber
Upper crust
Magma conduit
~20 km
DEPTH
Lower crustal magma chamber
Lower crust
~30 km
Upper mantle
Magma pods

**Figure 2.12:** Illustration (no scale) of a continental volcanic system showing the local occurrence of earthquakes. Figure taken from Hill et al. (2002).

is the quasi-static diffusion of stresses with time through deformation of the elastic crust until the viscoelastic system reaches a new state of equilibrium.

Static stress transfer as interaction mode appears to explain both, earthquake-volcano and volcano-earthquake interactions (Hill et al., 2002). Changes in the dilatational component of the stress field caused by the slip of a fault during an earthquake can trigger a response in a nearby magma body. For example, the increase in compressional stress can pressurize an already fully charged magma body, or the decrease in compressional stress may promote vesiculation, bubble formation, and the opening of conduits, both breeding volcanic eruptions. In the other case, volcano-earthquake triggering due to static stress changes in the elastic crust can be caused by an inflating or deflating magma body, changing shear stresses (Coulomb failure stress $\Delta CFS$) in the vicinity of a fault and bringing the fault closer to the threshold of slip. This triggering mechanism can be applied to volcanoes, mud volcanoes and geysers (Manga and Brodsky, 2006), and was suggested for the eruption of Mt. Vesuvius, Italy, followed by magnitude $M \approx 7$ earthquakes at distances of approx. 100 km (Nostro et al., 1998).

But the understanding of local, near field volcano-earthquake interactions is more important for the assessment of eruptive behavior and its hazardous impacts. Figure 2.12 shows the anatomy of a continental volcano. Partial melting of the upper mantle at depths of about 100 km produces basaltic magma that rises buoyantly into the base of the crust and partially melts surrounding rocks. Moving upward through the crust in dike-like cracks, volatile components (mainly water, carbon dioxide, sulfur dioxide) dissolved in the magma at high pressures deep in the crust exsolve to form bubbles at lower pressures (in the shallow crust). Formation and rise of bubbles pressurize magma chambers, forces the magma to ascent, both inducing small earthquakes in the brittle upper $\leq$ 15 km of the crust (Hill et al., 2002). With methods of volcanic seismology mapping the signals of these events, active magmatic systems and their configuration can be characterized, the extent and evolution of magmatic source regions can be determined and insights into the mechanical properties of volcanic fluids and sub-volcanic mass-transport dynamics can be gained (Chouet, 2003).

Volcanic seismicity can be sub-divided into the following major forms (McNutt, 2000):

**Short-Period (SP) earthquakes,** also known as volcano-tectonic (VT) or high-frequency (HF) events, are like tectonic earthquakes generated by the slip of faults. They are caused by the fracturing of rock material as magma forces its way through the crust towards the surface. The VT events with frequencies above 10 Hz signify the growth of a magma body near the surface. Their signal sources are dominated by brittle failure and not by fluid dynamical processes like in the remaining cases.

**Long-Period (LP) earthquakes** indicate increased gas pressure in the shallow parts of a volcano's plumbing system, and are excited by degassing or boiling of volatile-rich magmas within fluid-filled cracks. LP signals are decaying harmonic oscillations equivalent to acoustic vibrations within a resonator. Therefore, the properties of the fluids inside the magmatic (resonator) system at the source of LP events may be inferred from the frequencies, typically in the range from 0.5 to 5 Hz, of the decaying harmonic oscillations of the signal.

**Volcanic tremor** is often the result of underground movement or venting of magma and volcanic gases, pushing against the overlying rock. It is also known as harmonic tremor, as its signal shows a characteristic long-duration release of seismic energy with distinct spectral, harmonic lines. In some cases, harmonic tremor evolves from a sequence of overlapping LP earthquakes and may persist with relatively steady to strongly fluctuating amplitude levels for minutes to hours.

**Very-Long-Period (VLP) earthquakes** are a clear indication of the repeated action of a non-destructive volumetric source. Associated with variations in magma transport rate through cracks or dikes within or beneath the volcanic edifice, VLP events may be used to map the geometry and location of magma conduits and volumetric budget of magma bodies. Their frequency spectra have dominant peaks at periods of tens of seconds.

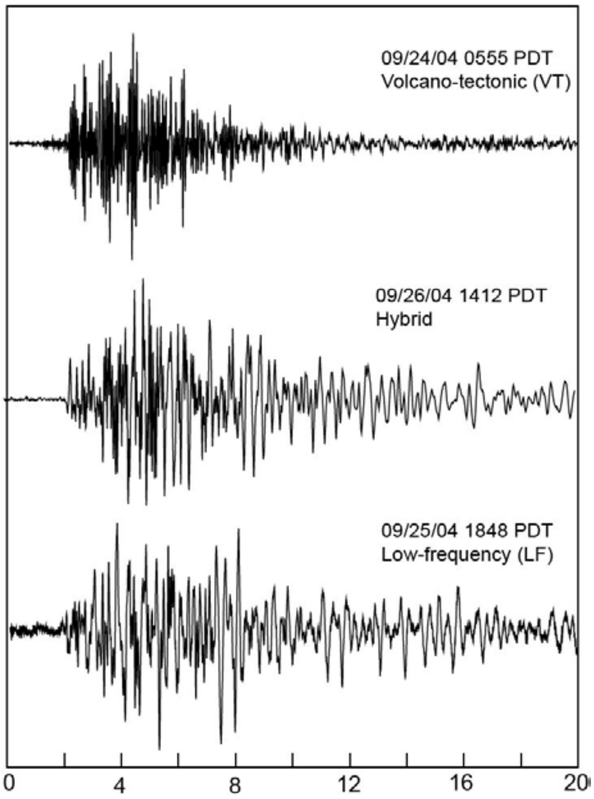

**Figure 2.13:** Waveforms for typical volcano-tectonic, hybrid and low-frequency events recorded at Mount St. Helens, Washington, during first four days of renewed activity in 2004. Time in seconds. Figure source: Moran et al. (2008).

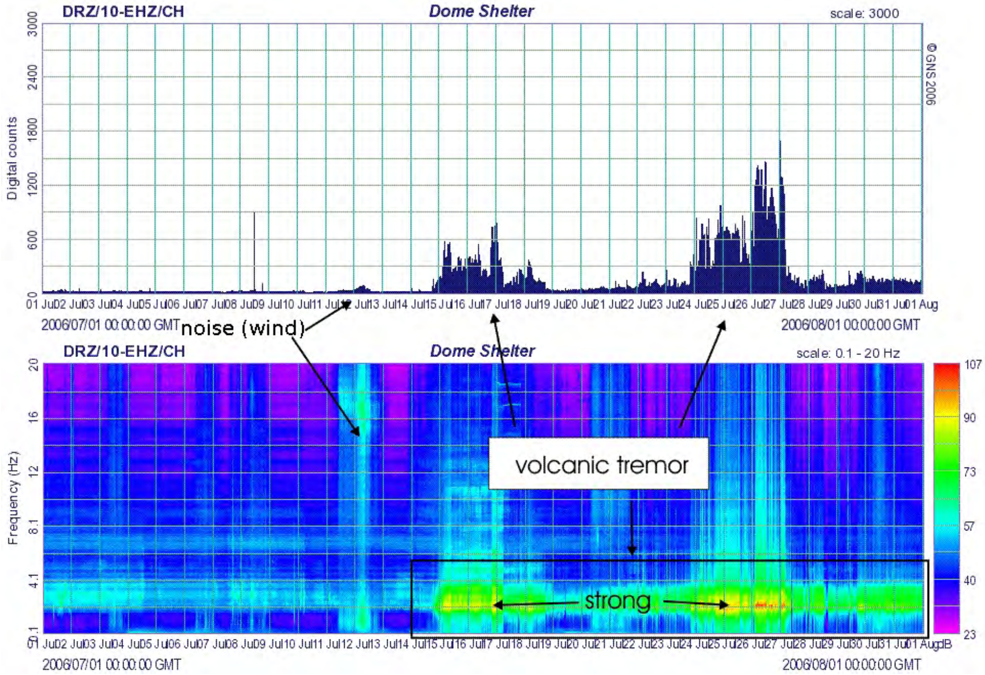

**Figure 2.14:** Real-time seismic-amplitude measurement plot (overall signal size over periods of 10 minutes, top) and seismic spectral-amplitude measurement plot (relative signal size in different frequency bands, bottom) showing volcanic tremor at Mt. Ruapehu, New Zealand, 2006. Volcanic tremor tends to have energy in a limited range of frequencies (a narrow-band signal). Figure source: GeoNet (2006).

Low-frequency (LF) earthquakes with sources dominated by fluid dynamic processes, i.e. LP and VLP earthquakes and harmonic tremor, are almost exclusively limited to active volcanic areas and geothermal settings. Therefore, they are often referred to as volcanic earthquakes.

Especially the spatiotemporal properties of the mapped seismicity in the upper 5 km of the crust are useful for volcanic hazard assessment, because the increase of shallow LP events and the amplification of harmonic tremor are good indicators for an increasing eruption risk. The quantification of source mechanisms and mass transport phenomena associated with eruptive activity by analyzing VLP earthquakes helps to evaluate the eruption energy. But the understanding of the actual fluid dynamics and attendant pressure fluctuations underlying the excitation of LP and VLP events and volcanic tremor is still poor (Chouet, 2003). Additionally, hybrid earthquakes, i.e. seismicity intermediate in character between high-frequency earthquakes and volcanic earthquakes, are common on active volcanoes, and they result from a variety of processes. For example, an initial brittle failure high-frequency event can trigger resonance in a fluid-filled crack, resulting in a mixed signal. Or, at extremely shallow depths less than 2 to 3 km high-frequency signals may be scattered by strong heterogeneities in the crust or attenuated by propagation through a fluid body, and appear as low-frequency event in the seismograph. Thus, conceptual and numerical modeling of seismic sources at volcanic settings allow both approaches for improving

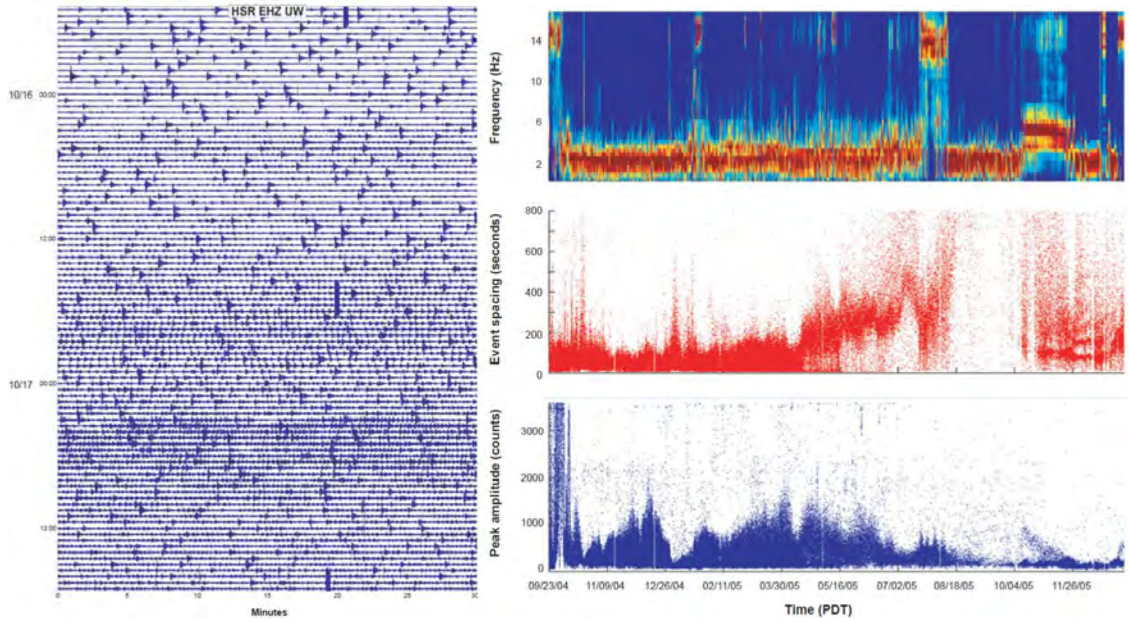

**Figure 2.15:** Left: Seismic record from 1700 on October 15 through 1800 on October 17, 2004, showing onset of small, regularly spaced events occurring between larger events at MSH. Right: Plot showing spectral-amplitude (dominating LF band, top), inter-event spacing (period of approx. 150 s, middle), and peak amplitudes (bottom) for detected events at MSH between September 23, 2004, and December 31, 2005. Figure taken from Moran et al. (2008).

the physical understanding of volcano-earthquake interactions: brittle failure concepts for describing volcano-tectonic seismicity sources and fluid dynamic processes for modeling the origin of volcanic earthquakes.

The conceptual model proposed by Iverson et al. (2006) for the occurrence of periodic earthquakes during the 2004-2006 Mount St. Helens (MSH) lava dome building activity is an outstanding example for a brittle failure approach in modeling the seismic source during a volcanic eruption. But beside significant volcano-tectonic events in the beginning of the renewed activity, seismic records showed clear frequency bands typical for volcanic tremor and hybrid earthquakes (see Figure 2.15), and Waite et al. (2008) were even able to identify the VLP source underneath the newly extruded lava dome in a later study.

Thus, models based on pure brittle failure seismicity cannot sufficiently mimic the complexity of earthquake generation at volcanic settings. Because high-pressure fluids play an obvious role in magmatic systems, involving the nature of fluid flows is particularly important and essential in modeling volcanic seismicity. This forms the basis for chapter 5.

# Chapter 3

# Modeling Eruption Cycles and Decay of Mud Volcanoes

(Published 2009, Marine and Petroleum Geology, Vol. 26, Issue 9, pp. 1879-1887)

Recent debates about the eruptive behavior of mud volcanoes and their activation mechanisms has been driven particularly by the LUSI eruption in Indonesia that resulted in huge commercial and cultural damages. Numerical modeling of mud volcanoes, of which few exist, can provide insight into eruptive behavior and contribute to hazard evaluation. In this chapter, we present a simple model to describe fluid escape from an underground reservoir through a conduit, extruded as a mud volcano at the surface. The governing equations result in oscillatory behavior, and we study the influence of changes in rheological properties of surrounding rock and fluid characteristics of the mud on extrusion dynamics. We focus on understanding long-term eruption behavior, flow cycles, and decay factors. Model results can be used to estimate the discharge rates and extruded volume from assumptions on the mud reservoir and conduit, or conversely, the reservoir or conduit properties from discharge rates.

## 3.1 Introduction

Mud volcanoes result from the extrusion of gas- and water-saturated mud both in sub-aerial and in sub-marine environments. This semi-liquid is forced through openings in the upper crust, sometimes producing massive quantities of mud on the surface, as evidenced by the recent LUSI mud volcano in Java, Indonesia. Globally, the distribution of mud volcanoes shows about 1800 individual sites (Dimitrov, 2002), and extraterrestrial occurrences are also documented (Fortes and Grindrod, 2006; Skinner and Tanaka, 2007; Skinner and Mazzini, 2009). The basic mechanism of mud volcano formation is the release of high-pressure mud trapped at depth. Triggering mechanisms of the volcanoes are still debated, but various hypotheses include earthquake-triggering, fault failure, and drilling (Manga et al., 2009, and references therein).

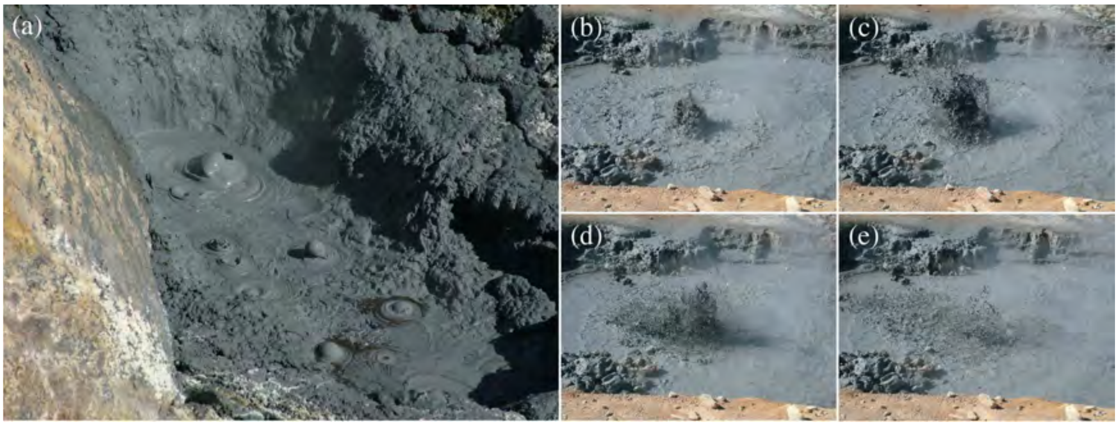

**Figure 3.1:** (a) Mud volcanoes belonging to a mud pool near Krafla volcano. (b)-(e) Detailed view on an eruption. Námaskarð region, Iceland.

The morphology of mud volcanoes varies, and includes conical vents and bubbling mud pools (Figure 3.1(a)). Some mud sources are shallow $< 1$ km, while others are fed by reservoirs at depths of up to 6 km. Vents range from the centimeter scale to several hundreds of meters (Aslan et al., 2001; Mazzini et al., 2009). Extruded material can include mud, gas, boulders of clay or other solid material, indicating that dike-like conduits form in response to overpressurized fluids flowing along permeable fractures, eroding the wall rock and evolving to an open vent (Bonini, 2007).

This study investigates mechanical considerations of mud volcanism. While some mud fields are continuously active (with ongoing substantial seepage for more than 60 years of observation), other areas exhibit an alternation between periods of eruption and relative quiescence. The time intervals between significant material escape during dormant stages vary from minutes to several days, but in many cases show a cyclic behavior. For example, the Dashgil mud volcano in Azerbaijan is characterized by continuous pulsating venting of mud, water and gas (Hovland et al., 1997; Mazzini et al., 2009). Onshore in Trinidad, it has been shown that the vertical conduits allow the escape of gas-charged methane-rich cold seeps. The mud volcanoes have cyclic phases of eruptions, where the initial sedimentary mobilization could have occurred from pore water in deep sandy reservoirs (Deville et al., 2006). For the mud field along the Pede-Apennine margin, fault failure cycles (tectonic loading and unloading) are hypothesized to promote a long-term fluid release cycling, during which overpressurized fluids are periodically discharged from a reservoir through the creation or the reactivation of fractured systems (Bonini, 2007). A highly studied case is the eruption of mud and gas called LUSI that started 29th of May 2006 in North east Java (Davies et al., 2008; Mazzini et al., 2007). The discharge rate rose from 5000 to 120,000 $m^3/d$ during the first eleven weeks, flooding large areas of the Sidoarjo village. The mud flow then was observed to pulsate, and the extruded volume again increased dramatically following earthquake swarms. Although LUSI was perturbed several times, the mud flow shows a clear tendency to pulsate every few hours and to erupt in changing cycles - an important characteristic that has lasted for more than two years and continues still.

The observed oscillatory behavior of mud volcanoes is the focus of the conceptual and mathematical model proposed here. We focus on the periodic characteristics and develop mathematical model equations where the solution for the material discharge rate oscillates naturally. Results are presented that describe the solution and its dependence on initial conditions and physical parameters such as fluid properties and characteristics of the mud volcano. In the case where an eruption or seepage process decays over time, results show the evolution towards an oscillatory state about equilibrium. Integration of the calculated discharge rate provides information about the volume extruded at the surface, allowing comparisons and observational constraints on processes occurring at depth as well as estimates on societal hazards.

## 3.2 Conceptual model

Figure 3.2 shows the conceptual model. We assume that a mud volcano consists of two components; a mud reservoir with volume $V$ at a certain depth beneath the surface, and a vertical cylindrical conduit with cross-sectional area $A$ and height $h$.

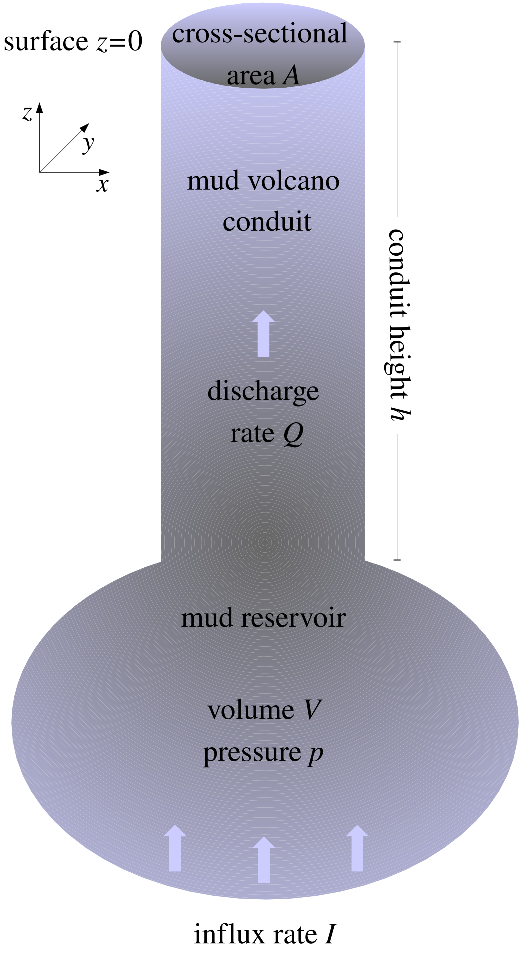
surface z=0
cross-sectional area A
z
y
x
mud volcano conduit
conduit height h
discharge rate Q
mud reservoir
volume V
pressure p
influx rate I

**Figure 3.2:** Schematic illustrating the basic concept of our two-component mud volcano model (not to scale).

The choice of a two-component system is not arbitrary, but arises from the observation that mud eruptions are activated and influenced by pressure or rheological changes at depth (Bonini, 2007; Manga et al., 2009; Mazzini et al., 2009). As a first approach, we investigate a scenario where the reservoir is filled with mud of pressure $p$ and density $\rho$, related through an adiabatic condition for mud compressibility $\beta$. Material enters the reservoir across its surface $S$ with a volumetric influx rate $I$, producing a pressure increase inside the reservoir. In addition, we allow a possible secondary pressurization of the system due to a reservoir deflation. The overpressure forces the mud to leave the system with a volumetric discharge rate $Q$ via mud ascent inside an open cylindrical conduit. More realistic scenarios should encompass different types of observed mud volcano conduit styles, for example, conical vents (Deville et al., 2006; Dimitrov, 2002), fracture zones filled with permeable rock (Ingebritsen and Rojstaczer, 1993) or the combination of fractured systems ending up in open conduits near the surface.

This model set-up contains many parameters that influence the behavior. Instead of a detailed study of all possible parameter combinations, we choose to make some simplifications to reduce the mathematical complexity. We investigate the evolution of the discharge rate function of a mud volcano in time, after the fluid escape has already been initiated by an unidentified triggering mechanism (Mazzini et al., 2009), and after a conduit evolved from an initial venting process (Gisler, 2009). Although this simple model ignores potentially important details of an eruption, this formulation results in essential characteristics of the mud volcano system, most importantly the long-term oscillatory behavior.

The primary constraints are the geometry of the reservoir and conduit. We assume a cylindrical conduit, and ignore variations in cross-sectional area due to erosion of the conduit wall. For the reservoir, we adopt models developed for magma chambers (Denlinger and Hoblitt, 1999; Iverson et al., 2006; Iverson, 2008). For instance, the fluid inside the reservoir balances pressure changes via density changes, the geometry is assumed spherical or cubic, the influx velocity of additional material is constant, and the reservoir volume change is either zero (non-deflating case) or negative (deflating reservoir).

Second, we make simplifications on the mud properties. In general, mud most likely behaves as a compressible non-Newtonian fluid, requiring the use of density and viscosity functions (Mazzini et al., 2009). Compressibility effects are important when compaction exceeds percolation effects (Gisler, 2009). Therefore, we regard mud compressibility inside the pressurized reservoir, but inside the conduit we adopt an isochoric flow condition for the mud discharge rate. Thus, velocity and density changes with position are negligible, implying zero density changes with time. This simplification generally may not be applied when analyzing velocity profiles or when determining resonance effects due to the flow of fluids with Mach numbers over 0.3 (the dimensionless ratio of flow velocity to speed of sound in the material), but regarding global solutions of compressible flow problems this adoption is feasible (Desjardins and Grenier, 1998; Lions and Masmoudi, 1998). Therefore density changes may be neglected and thus mud density $\rho$ is taken constant in our conduit model. We also assume a constant dynamic viscosity because, after the onset of eruption, the temperature gradients are low between the source and the surface. (In the case of LUSI, the exit mud temperature was about 100°C, close to the temperature at the source (Mazzini et al., 2009)). More advanced models should include a temperature-dependent viscosity, but this is beyond the scope of the present study. Under certain conditions, mud can behave thixotropically, but this property is more relevant for the triggering process at depth than for influencing the ongoing discharge. For discussion on the influence of non-constant viscosity values on the discharge rate behavior, we refer to Melnik and Sparks (1999, 2005); Wylie et al. (1999) and Yoshino et al. (2007).

## 3.3 Mathematical formulation

The governing equations for the model are conservation of mass and momentum for the mud inside reservoir and conduit. The constitutive model is described below. Temperature is assumed to play a minor role in mud volcanoes, and we introduce an adiabatic condition for mud compressibility $\beta$. Within the vertical system leading to the surface, we treat mud ascent as an isochoric flow of a Newtonian fluid with constant density $\rho$ and dynamic viscosity $\mu$. We ignore variations of mud properties and conduit geometry with depth. Discharge velocity $u$ is driven by reservoir pressure, and is resisted by the mud weight and a drag force depending on conduit characteristics. We present two constraints on the reservoir, where differences in its behavior imply different influx functions $I$, and combine these reservoir models with the conduit set-up to deduce equations describing a wide range of mud volcano eruption systems. All symbols with units are listed in Table 3.1.

### 3.3.1 Governing equations

For ascending mud during a mud volcano eruption with density $\rho$ inside a cylindrical conduit with constant cross-sectional area $A$, conservation of mass in the one-dimensional case is:

$$\frac{d\rho}{dt} + \frac{d\rho u}{dz} = 0, \tag{3.1}$$

and the conservation of momentum is described by the 1D Navier-Stokes equation with negligible convection:

$$\frac{d\rho}{dt}u + \frac{du}{dt}\rho = -\frac{dp}{dz} - \rho g - \frac{8\pi\mu u}{A}, \tag{3.2}$$

where $u$ denotes the mud ascent velocity, $p$ is the mud pressure, $g$ is gravitational acceleration, $z$ is the vertical direction (positive upwards), $t$ is the time and the last term denotes a drag resistance that depends on conduit characteristics. Here, for an open vertical system, this drag force is inferred from Poiseuille flow assumptions with constant dynamic viscosity $\mu$ and conduit cross-sectional area $A$, geared to models derived for volcanic settings (Barmin et al., 2002; Costa et al., 2007; Dobran, 2001).

Rearranging Equations (3.1) and (3.2), replacing the pressure gradient by a linear pressure increase with depth $h$, and integrating over the constant cross-sectional area $A$, we formulate an ascent equation as a function of discharge rate $Q$:

$$\frac{dQ}{dt} = \frac{A}{\rho h} p - Ag - \frac{8\pi\mu}{\rho A} Q \tag{3.3}$$

for mud flow inside an open conduit. The advantage of this equation is that estimates of the extruded mud volume at the surface can be obtained by time integration.

We assume the following boundary conditions for Equation (3.3):

$$\begin{aligned} z = 0: &\qquad p &&= 0, &(3.4)\\ z = -h: &\qquad \frac{dp}{dt} &&= \frac{1}{\beta V}\left(I - Q - \frac{dV}{dt}\right), &(3.5)\end{aligned}$$

where $V$ is the reservoir volume, $I$ is the volumetric mud influx rate into the reservoir, $Q$ is the volumetric mud discharge rate into the conduit and $h$ is the conduit height (being equal to the reservoir depth). Equation (3.5) is derived from the equation for conservation of fluid mass inside the reservoir

$$\rho\frac{dV}{dt} + V\frac{d\rho}{dt} = \rho(I - Q), \tag{3.6}$$

combined with the mud compressibility

$$\beta = \frac{1}{\rho}\frac{d\rho}{dp} \tag{3.7}$$

that describes the density response due to pressure changes.

For $dV/dt < 0$ in the last term of Equation (3.5), the boundary condition provides a reservoir deflation process, whereas for the case of a non-deflating reservoir the volume $V$ is constant, thus the last term of Equation (3.5) is zero, and the boundary condition at $z = -h$ reduces to

$$\frac{dp}{dt} = \frac{1}{\beta V}(I - Q). \tag{3.8}$$

This formulation shows that, inside the reservoir pressure decreases due to the mud discharge rate $Q$, and increases due to the mud influx rate $I$ or alternatively by the reservoir deflation $dV/dt$.

### 3.3.2 Supplementary equations

We make two assumptions regarding the conditions inside the mud reservoir beneath the vertical conduit. First, we assume a constant reservoir volume $V$, and second we allow the reservoir to deflate linearly with its radius $r$. These are strong assumptions, but they show how the model is affected by constant and decreasing fluid sources.

A more likely case is a combination of the two, and can be constrained by the mud volcano of interest. For example, in cases of observed subsidence (such as the LUSI eruption) it is reasonable to assume a deflating reservoir (Mazzini et al., 2007).

For a steady-state condition of the reservoir volume $V$, we assume a constant material influx at velocity $v =$ constant and $dV/dt = 0$. Since the influx rate $I$ depends on the influx velocity $v$ times the reservoir surface $S$, the influx rate $I$ is constant, and we denote it by $I_{const}$.

For a deflating mud-filled reservoir we use the elementary relations between the reservoir surface $S$ and reservoir volume $V$ (for instance, a spherical or cubic reservoir geometry yield the dependencies $dV = Sdr$ and $S \propto \sqrt[3]{V^2}$, to within a numeric factor), and we assume a constant, negative radius decrease with time $dr/dt < 0$, resulting in the volume change function

$$\frac{dV}{dt} = S\frac{dr}{dt}, \tag{3.9}$$

with $|S(dr/dt)| \leq Q$, since we restrict the reservoir deflation to a smaller rate than the discharge rate. Retaining a constant material influx velocity $v =$ constant, and assuming again the continuity equation $I = vS$ for the volumetric flow rate $I$ of mud through the reservoir surface $S$, the decreasing reservoir surface has a direct impact on the influx rate. The change rate of $I$ is related to the change rate of $S$ via $SdI/dt = IdS/dt$, which can be used to substitute $I$ or $S$ where necessary. For instance, we obtain

$$\frac{dI}{dt} = c \cdot \frac{I^2}{V}, \tag{3.10}$$

where the negative constant $c < 0$ contains $dr/dt$, $v$ and fundamental spherical (or cubic) geometry parameters from the relation between surface, volume and radius of the reservoir. We point out that other influx functions are possible, since many approaches already exist to the problem of fluid influx into a chamber, e.g. allowing periodic supply rates by making stronger assumptions on influx velocity or rate (Dobran, 2001; Georgiou, 1996). We proceed using Equation (3.10), to avoid arbitrary and non-physical assumptions on the influx rate, and to keep the model transparent.

### 3.3.3 Results

In order to make estimates on the extruded volume at the mud volcano surface, we reformulated the fundamental model Equations (3.1)-(3.2) to obtain Equation (3.3) for the mud propagation through an open conduit. The meaning of this equation becomes apparent after differentiation with time and combination with Equation (3.5), yielding the physical implication of the discharge rate function

$$\frac{d^2Q}{dt^2} = \frac{A}{\rho h \beta V}\left(I - Q - S\frac{dr}{dt}\right) - \frac{8\pi\mu}{\rho A}\frac{dQ}{dt}. \tag{3.11}$$

Equation (3.11) is a second order differential equation with the form of damped, forced oscillators. This implies that the discharge rate $Q$ has a natural tendency to oscillate with the period and damping controlled by the particular choice of parameters.

The general form of damped, forced harmonic oscillators is mostly given by

$$\ddot{x} + 2\gamma\dot{x} + \omega^2 x = F, \tag{3.12}$$

where $x$ is the oscillator, $\dot{x}$ and $\ddot{x}$ its time derivatives, $2\gamma$ denotes the damping constant, $\omega$ is the characteristic, natural, angular frequency (giving the frequency of the oscillation via $f = \omega/(2\pi)$), and $F$ is an external force (Iverson, 2008, and references therein). Compared to Equation (3.11), we can extract some preliminary estimates on the effects caused by constant parameters. For instance, the root of the term $A/(\rho h\beta V)$ can be associated with the angular frequency of an oscillator. Therefore, we expect the conduit geometry, the mud compressibility, and the mud density to affect the frequency of the discharge rate solution $Q$. The factor $8\pi\mu/(\rho A)$ in Equation (3.11) correspond to $2\gamma$ in Equation (3.12). That means that viscosity, density and conduit cross-section modifications are responsible for the damping of the oscillation for the mud volcano model. Finally, the expression $A(I - S(dr/dt))/(\rho h\beta V)$ is the external force acting on the oscillator Equation (3.11), controlling the amplitude and the forced oscillation frequency (generally different from $\omega$) of the solution. Here again, the conduit geometry and mud density occur, but the mud influx rate and the reservoir deflation become relevant for the discharge rate solution. This shows that by applying arbitrary equations for the influx rate $I$ or the reservoir deflation $dV/dt$, respectively, the model can be extended to mimic external factors controlling the system behavior. For example, seismicity triggered pore-pressure or permeability changes (Miller et al., 1996; Miller and Nur, 2000) influence the hydrological properties of the system (Rojstaczer et al., 1995), i.e. flow path or flow velocity changes, resulting in an eruption recharge or seepage reinforcement (Manga and Brodsky, 2006).

This formulation gives the possibility to constrain parameter values in order to ensure oscillation of the system. The harmonic, damped system oscillates, if $\gamma^2 < \omega^2$ (under-damping), i.e. parameter combinations must be chosen carefully (over-damped and critically damped systems $\gamma^2 \geq \omega^2$ are not covered in this work). Furthermore, the model proposed here requires a minimum initial influx rate, as part of the external force $F$ acting on the system. We do not include an explicit discussion of this here, because values of $0.1 - 2$ m$^3$/s provide satisfactory results and are more than 4 orders of magnitude larger than the minimum influx rate.

## 3.4 Numerical results

We solve the system Equation (3.3) using the boundary conditions (3.5) and (3.8) with a fourth order Runge-Kutta solver for ordinary differential equations with constant $I_{const}$ or the solution to Equation (3.10).

Parameter values listed in Table 3.1 are taken from the literature concerning mud volcanoes (Aslan et al., 2001; Bonini, 2007; Hovland et al., 1997), mud mobilization

**Table 3.1:** Parameter symbols, description and their values or conversion used for numerical computation.

| Symbol | Value | Unit | Definition |
|---|---|---|---|
| $A$ | $0.1 - 10^3$ | $\mathrm{m}^2$ | conduit /column cross-sectional area |
| $\beta$ | $10^{-2} - 10^{-8}$ | $\mathrm{Pa}^{-1}$ | mud compressibility inside reservoir |
| $c$ | $c < 0$ | none | dimensionless number for influx rate solution |
| $g$ | $9.81$ | $\mathrm{m\ s}^{-2}$ | gravitational acceleration |
| $h$ | $500 - 4000$ | m | conduit /column height |
| $I_0$ | $0.1 - 2$ | $\mathrm{m}^3\ \mathrm{s}^{-1}$ | initial mud influx rate |
| $I_{const}$ | $0.1 - 2$ | $\mathrm{m}^3\ \mathrm{s}^{-1}$ | constant mud influx rate |
| $\mu$ | $10^{-6} - 10^2$ | Pa s | mud viscosity |
| $Q_0$ | $0 - 2$ | $\mathrm{m}^3\ \mathrm{s}^{-1}$ | initial mud discharge rate |
| $r_0$ | $\propto \sqrt[3]{V_0}$ | m | initial reservoir radius |
| $\rho$ | $500 - 2000$ | $\mathrm{kg\ m}^{-3}$ | mud density in conduit |
| $S_0$ | $\propto \sqrt[3]{V_0^2}$ | $\mathrm{m}^2$ | initial reservoir surface |
| $u_0$ | $Q_0/A$ | $\mathrm{m\ s}^{-1}$ | initial mud velocity |
| $v_0$ | $I_0/S$ | $\mathrm{m\ s}^{-1}$ | initial mud influx velocity |
| $V_0$ | $10^6 - 10^{12}$ | $\mathrm{m}^3$ | initial reservoir volume |

and eruption processes (Deville et al., 2006; Dimitrov, 2002; Mazzini et al., 2007), and drilling research (Wojtanowicz et al., 2001).

### 3.4.1 Mud flow with deflating reservoir

For the deflating reservoir case, we investigate the influence of physical parameters on the discharge rate $Q$, i.e. dynamic viscosity $\mu$, conduit cross-sectional area $A$ or the initial reservoir volume $V_0$. Figures 3.3 and 3.4 show representative solutions to the discharge rate function $Q$. The influx rate $I$ (initialized by an external triggering mechanism) causes an increase in reservoir pressure $p$ and the beginning of mud discharge $Q$ towards the surface. At the same time, the reservoir volume and its surface deflate, effecting a decrease in $I$. Consequently, $Q$ decays over time in an oscillatory behavior with a constant period, reaching its equilibrium $Q = 0$ after certain characteristic times.

Further insights on the model behavior are provided by close-up views of the period of discharge rate oscillations depending on parameters and initial conditions. First, we discuss the changes on discharge rate behavior due to changes in the initial conditions shown in Figure 3.3. Decreasing initial reservoir volume $V_0$ by one order of magnitude leads to a faster decay (from 3 years down to 6 months) of $Q$ towards

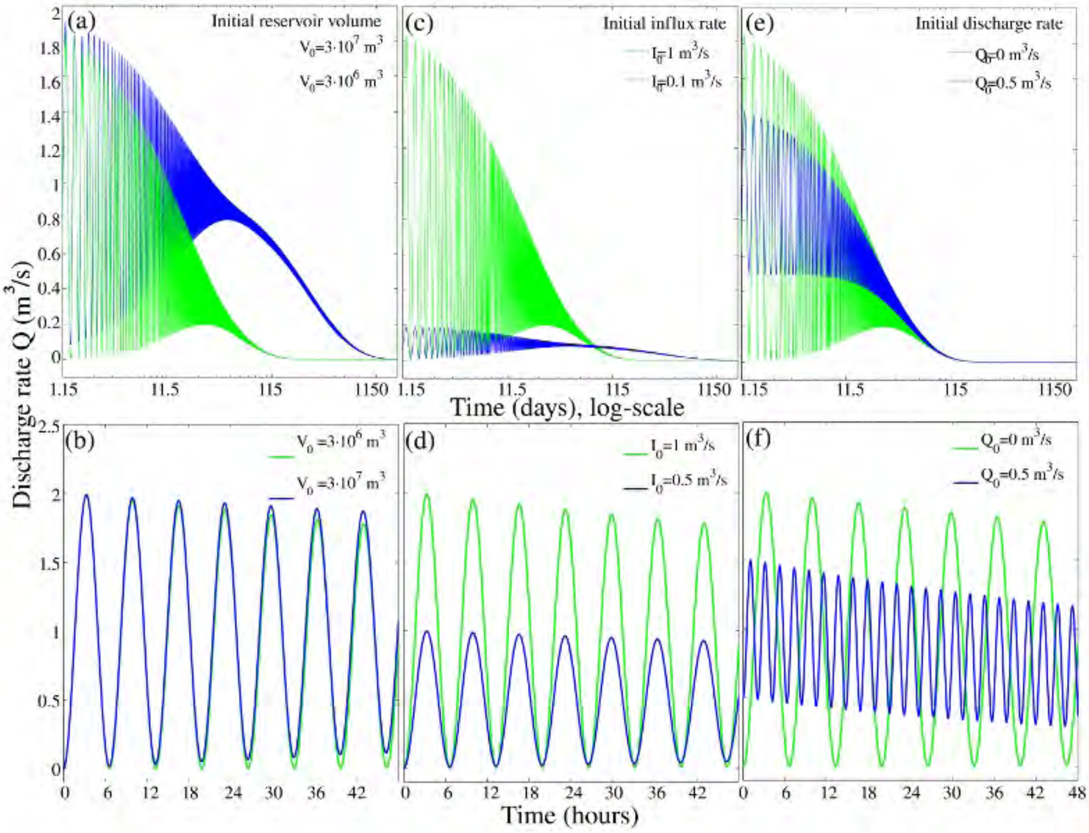

**Figure 3.3:** Discharge rate $Q$ solutions for a change in initial conditions. (a) Decreasing $V_0$, a faster decay can be seen. (b) Close-up, no period changes. (c) A decrease in $I_0$ changes the extrusion intensity and decay. (d) Detailed view shows amplitude changes by factor 0.5, while period remains the same. (e) Long-term $Q$ solution for increase in initial discharge rate $Q_0$. (f) The period between oscillation peaks drops to approx. 2 hours.

zero. This result is reasonable as a larger reservoir needs more time to deflate. The discharge rate period, however, is not affected (Figure 3.3(b)).

Tests on the initial mud influx rate into the reservoir and discharge rate into the conduit are relevant for ongoing mud flows. Observations in Indonesia for example show that an ongoing mud extrusion can be disturbed, stimulated or damped by outside factors (Mazzini et al., 2007). Changes in the initial influx rate $I_0$ are plotted in Figures 3.3(c) and 3.3(d). The extrusion period remains the same, but the amplitude decreases for smaller initial influx rates. The decay of mud discharge occurs at a later time. For an initial influx of 2 m$^3$/s, the maximum discharge rate $Q$ is 4 m$^3$/s and reaches zero two months earlier than for $I_0 = 1$ m$^3$/s, taken for most calculations. In general, we solve the system of equations with $Q_0 = 0$ m$^3$/s. The consequences on the solution for an increase are shown in Figure 3.3(e) for long term behavior and in Figure 3.3(f) as a close-up view. Discharge decays at the same time, but the oscillation amplitude and period change radically.

In the following, variations in parameter values are presented. A change in mud

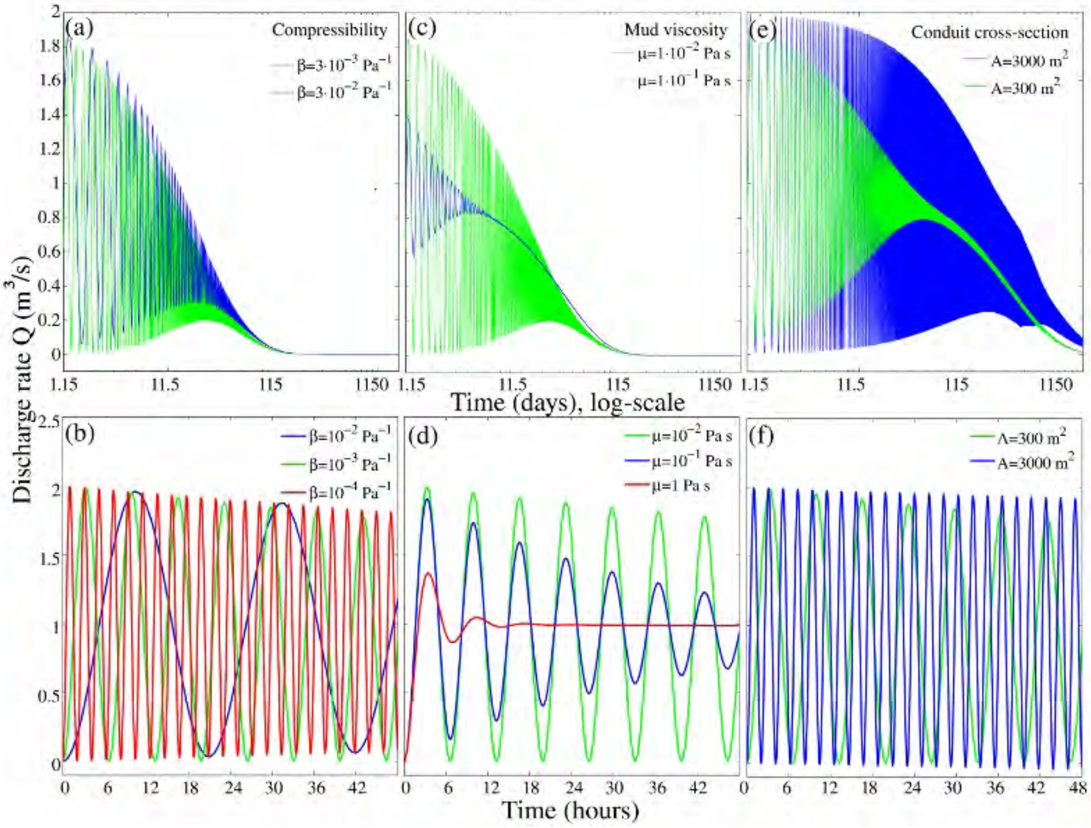

**Figure 3.4:** Discharge rate $Q$ for changes in parameter values. (a) Long-term behavior of mud compressibility $\beta$, decay occurs already after six months. (b) The smaller $\beta$, the shorter the discharge rate period. (c) Long-term discharge rate $Q$ for increase in mud viscosity $\mu$. Eruption period remains the same, oscillation amplitude decreases. (d) Reaching $\mu = 1$ Pa s, constant mud extrusion is observed following one significant discharge peak, decaying later on towards zero (not visible here). (e) Long-term discharge rate $Q$ evolution for increase in $A$ and (f) zoomed detail. Same effects can be seen for decrease in height $h$.

compressibility $\beta$ or density $\rho$ (not shown here) changes what is expected from damped oscillator equations. The decrease affects shorter periods (Figure 3.4(b)), but the decay time remains the same (Figure 3.4(a)). This result is intuitive; the lower the mud compressibility, the less mass per unit volume has to be extruded, ending up in shorter periods.

A comparison of plots in Figures 3.4(c), 3.4(d) shows the effect of increasing viscosity $\mu$. The period remains the same (approximately 6 hours between discharge rate peaks), but the stronger damping effect leads to a smaller oscillation amplitude. As the reservoir volume $V$ and influx rate $I$ are the same, the discharge rate reaches zero after six months like in the case shown in Figure 3.4(a). Changes in the conduit geometry produces similar results to the solution with different mud characteristics. Either an increase in cross-sectional area $A$ or a decrease in conduit height $h$, respectively, shortens the period between discharge rate peaks, while maintaining the decay time. Figures 3.4(e) and 3.4(f) show the result for changing $A$.

Results from this model provide many physically meaningful scenarios for comparisons with observations of mud eruption processes (and geothermal geyser behavior (Ingebritsen and Rojstaczer, 1993)) as related to different parameters and initial conditions. However, a possible extension of this model from observations is to allow flow through fractured media, ending up in a full opening of the conduit (Gisler, 2009). This is an important aspect and will be the subject to future investigations.

### 3.4.2 Comparison with non-deflating reservoir

We conclude with solutions for a constant reservoir volume $V$ (thus the reduced form of the boundary condition (3.8)), and a constant material influx rate $I_{const}$. In addition to the discharge rate solution plots, we show the consequences on the amount of volume extruded at the surface due to the differences in the influx rate function.

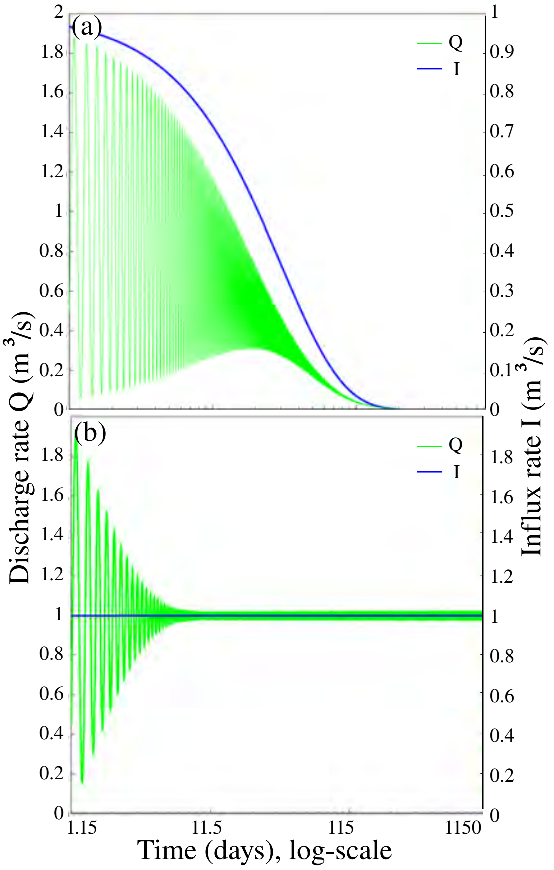

**Figure 3.5:** (a) Solutions for the influx $I$ and discharge $Q$ functions calculated from Equations (3.3, 3.5 and 3.10) given in previous paragraphs. As the mud reservoir deflates, $I$ decreases, and $Q$ decays towards zero following the solution graph of $I$. (b) Long-term discharge $Q$ and influx $I_{const}$ rates behavior. $Q$ decays towards the value of $I_{const}$. Logarithmic time scale.

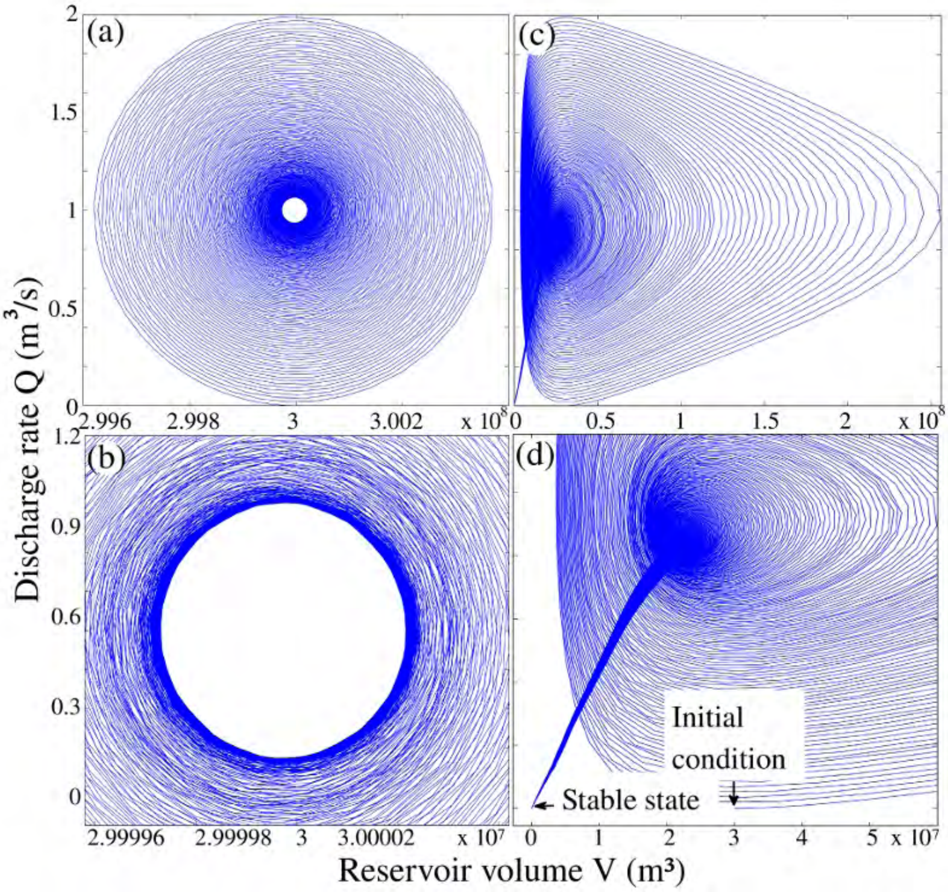

**Figure 3.6:** (a) Limit cycle and (b) detailed view for constant influx rate. Stable state of $Q$ is reached, when oscillating about the value of $I_{const} = 1$ m$^3$/s. Plotted versus fluctuating reservoir volume $V$. (c) Limit cycle, discharge rate $Q$ vs. reservoir volume $V$, for an open mud conduit with deflating source. (d) Zoomed detail of Figure c, showing up the initialization and equilibrium points. Periodic behavior with stable state in (0,0).

Figure 3.5(a) shows the influx rate function $I$ and resulting discharge rate $Q$ for an open conduit combined with a deflating reservoir, and Figure 3.5(b) shows $Q$ as result of a constant $I$. While in the first case the discharge rate decays towards zero, here the discharge rate decays to an oscillation about a constant equilibrium. This is confirmed by the limit cycles of both processes, where the discharge rate $Q$ is plotted versus the reservoir volume $V$. For the non-deflating case, the discharge rate decays to oscillate about a constant equilibrium volume (Figures 3.6(a), 3.6(b)), while the cycle concentrates and reaches its final stable state at zero discharge rate $Q$ and zero reservoir volume $V$, when considering deflating reservoirs (Figures 3.6(c), 3.6(d)).

Variations in $I_{const}$ result in differences in final discharge rate values (see Figures 3.7(a), 3.7(b)), and additional parameter modifications affect changes in oscillation period and / or amplitude as seen previously. The long-term graphs for changes in viscosity $\mu$ are plotted as representative examples in Figure 3.7(c). Plots for the remaining parameter changes are not included. However, they yield similar results in period and amplitude changes as presented for the case of a deflating reservoir, with the difference that the discharge rate $Q$ decays towards, and oscillates around the constant influx rate $I_{const}$.

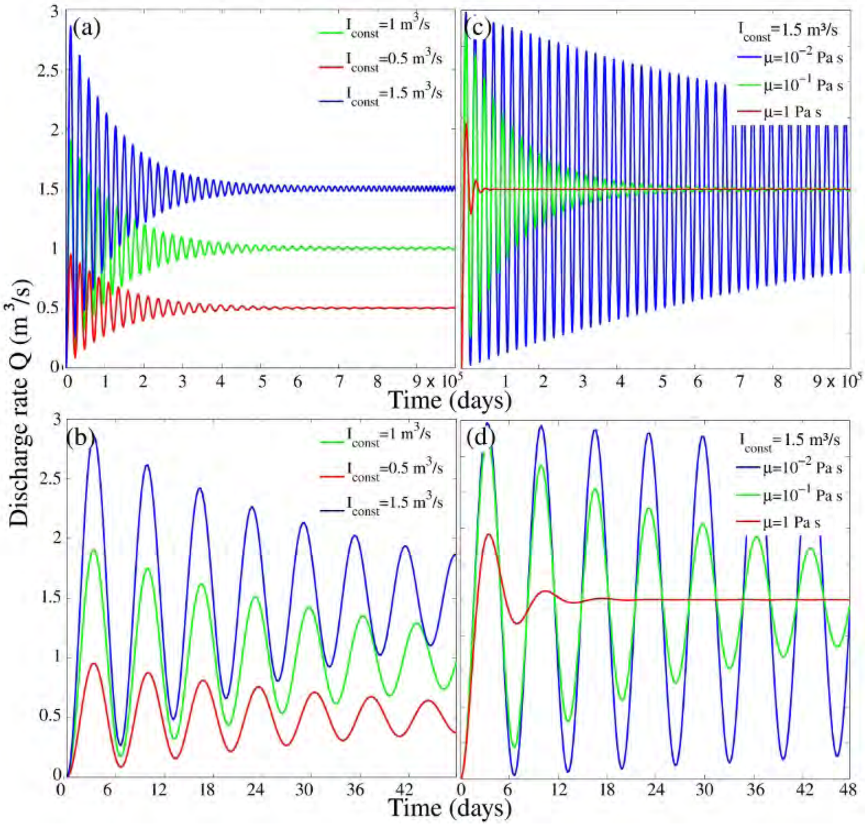

**Figure 3.7:** Discharge rate $Q$ functions for different values of $I_{const}$, (a) Long-term behavior and (b) zoomed detail. (c) Discharge rate $Q$ for constant $I$ and additional changes in $\mu$. (d) As expected, the discharge rate oscillation amplitude changes.

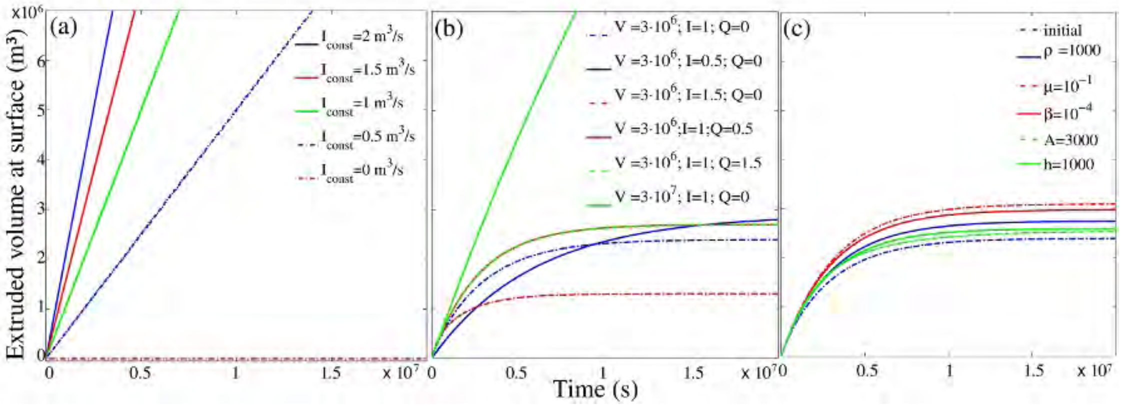

**Figure 3.8:** Extruded volume at surface of the mud volcano. (a) Dependence on a constant influx $I_{const}$. (b) Dependence on initial conditions, when $I$ is not constant. (c) Dependence on parameter choices, when $I$ and $Q$ decay to zero.

Finally, we examine the differences on the extruded mud volume at the surface caused by variations in model assumptions. Figure 3.8(a) shows the estimated mud volume at the surface after 3 years of significant activity. Due to the constant influx $I_{const}$ and non-changing source conditions, the extruded volume increases linearly with time. For the case where the reservoir deflates and consequently the mud source is finite, we expect a saturation of the extruded mud volume. Indeed, this effect can be seen in Figures 3.8(b) and (c), where different constant mud volumes are reached depending on changes in initial conditions and parameters.

## 3.5 Discussion and conclusions

We have developed a simple model to describe periodic mud volcano extrusion processes. One conduit geometry and two mud reservoir estimates were investigated. Our results demonstrate the dependence of the discharge rate and extruded mud volume solutions on the initial conditions and parameter choices. We interpret the oscillation period of the discharge rate as time between eruptions or maximum seepage, and the oscillation amplitude as the eruption or seepage intensity. In addition, we presented solutions for the estimated mud volume extruded at the surface.

Using a deflating mud source reservoir, the initial reservoir volume was identified as the main influence on the decay time of the discharge process. The initial influx rate also affects the decay of the process, but the differences are less significant. However, the amplitude is strongly driven by the influx rate, which we presume to be initialized by a triggering event that we do not attempt to identify. Other oscillation amplitude driving forces are the initial discharge rate, interesting for cases of disturbance of ongoing fluid flows, and the mud viscosity. Other parameters such as the conduit cross-sectional area, height and mud compressibility mainly influence the oscillation period and therefore the time between eruption peaks.

Investigations of a non-deflating reservoir (e.g. persistent supply and influx rates) show similar dependence of the initial conditions and parameters, but revealed an important modification possibility for seepage settings lasting for decades, as a continuous influx of material produces a pulsating discharge rate around a non-zero equilibrium.

Neglecting the initial triggering and conduit opening process, we examined mud ascent through an open mud volcano conduit. For application to real mud volcanoes, a combination of this approach with fractured rock models is more reasonable. That is, a fractured system at depth ending up in an open conduit in shallow regions close to the surface. This will be addressed in future studies.

Direct comparison with observations is difficult because of the lack of parameter constraints such as density, viscosity and discharge rates. The discharge rates of the LUSI mud volcano are reasonably well-constrained, but other parameters are not. For certain parameter combinations the oscillator equation is over-damped, i.e. the discharge rate function loses its periodic characteristic. Therefore our models do not only cover cyclic mud volcano behavior, but can also be used for single eruption investigations (not included here). However, cyclic behavior is very common, and our model can be adjusted to different mud volcano settings.

This simple model captures the basic dynamics of an eruption or seepage process, particularly the controls on the periodicity and decay time. Recognizing that initial values such as the influx rate function $I$ and reservoir volume estimates, and that parameters influence the system behavior, this model can mimic a wide range of mud volcano eruption situations. Possible extensions of this model would be to include fully compressible flow, the use of a non-constant viscosity, conduit erosion, and introducing various (possibly arbitrary) influx rate rules. We suggest that this model forms the basis for comparisons with data on mud volcano discharge rates and mud extrusion to the surface.

# Chapter 4

# Fluid Pressure Driven Aftershocks Following the 2009 L'Aquila Earthquake

This study expands on results published in Terakawa, Zoporowski, Galvan and Miller, Geology, Vol. 38(11), pp. 995-998, 2010. We analyze the correlation between aftershock locations and the Coulomb failure stress change $\Delta CFS$ and dilatation due to the 2009 L'Aquila earthquake, in order to identify the mechanism driving the aftershock sequence following the $M_w = 6.3$ main shock of April 6th. Our results establish that none of the tested earthquake fault slip settings causes Coulomb stress changes that can explain entirely the aftershock sequence. On the other hand, the aftershock locations coincide well with the highest fluid pressure gradients, which is known as mechanism of enhancing permeability and fluid flow. The diffusion of high pressure fluids as aftershock driving mechanism was shown for the 1997 Colfiorito sequence to the north of L'Aquila, both lying in the Apennines, Central Italy, on a boundary of regions of diffuse $CO_2$ degassing and regions where degassing is not observed. Furthermore, the time pattern of the aftershocks evolving towards Campotosto shows a breaking-seals-like formation. For these reasons, we consider the presence of fluids in the L'Aquila earthquake generation, and suggest the aftershock sequence to be driven by the diffusion of high pressure fluids from a deep source.

## 4.1 Introduction

The $M_w = 6.3$ L'Aquila earthquake occurred at 1:32 UTC on April 6, 2009 in the Apennines, Central Italy as an intra-plate event. The focal mechanism of the main shock (Figure 4.1) shows a NW-SE striking and southwest dipping slip fault with a hypocentral depth of about 9.5 km (Anzidei et al., 2009; Cirella et al., 2009; Walters et al., 2009), consistent with the regional extensional tectonic setting (Walters et al., 2009). The earthquake was preceded by foreshocks with magnitudes up to $M_w = 4.0$ on March 30, 2009, and was followed by extensive aftershock sequences with more than 10,000 events in shallow regimes (Chiarabba et al., 2009; ISIDe, 2009). This earthquake has been studied in some detail, and will be investigated

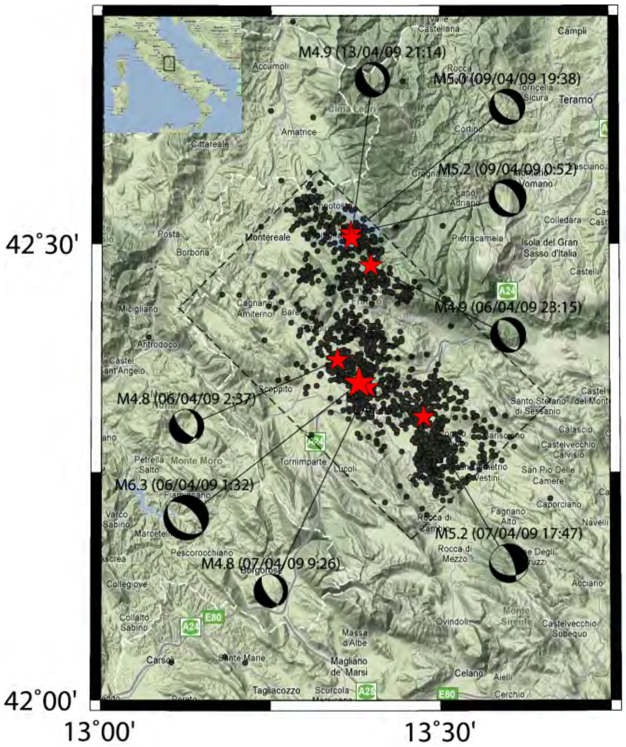

**Figure 4.1:** Map view of the L'Aquila region, Apennines, Italy, showing the location of the April 6 main shock and $M_w > 2$ aftershocks for a total of three months.

further in the future, but to date this sequence is not well-understood. Walters et al. (2009) proposed a source model obtained from InSAR and body-wave seismology, which shows consistency of nearby fault slip to stress changes. But recent fault geometry models deviate from these results (Anzidei et al., 2009; Cirella et al., 2009). Beside static stress change (King et al., 1994) hypothetical models for aftershock generation include poroelastic effects (Nur and Booker, 1972), post-seismic release of trapped high pressure fluids (Cox, 2010; Miller et al., 2004; Sibson, 2007) and rate-state dependent friction changes (Toda et al., 2002). As L'Aquila is situated at the boundary of a region of diffuse $CO_2$ degassing (Chiodini et al., 2004), and the 1997 Colfiorito aftershock sequence, which was shown to be driven by degassing of a high-pressure fluid source at depth (Miller et al., 2004), occurred in the same tectonic setting to the north (Collettini and Barchi, 2002), the involvement of fluids in the aftershock generation mechanism is likely.

In this study, we analyze the stress change and the dilatation caused by the L'Aquila earthquake main shock fault in order to identify the mechanism driving the aftershock sequence. The impact of the $M_w = 6.3$ main shock fault slip on the regional stress field is calculated and visualized with Coulomb 3.1 provided by the USGS (Lin and Stein, 2004; Toda et al., 2005). Our investigation encompasses the influence of various fault geometries and slip scenarios (Anzidei et al., 2009; Cirella et al., 2009; Herrmann and Malagnini, 2009; Walters et al., 2009) on the $\Delta CFS$ and dilatation in different calculation depths and cross-sections normal to the fault. The map views and cross-section views are overlaid with aftershock data (Chiarabba et al., 2009) for a total of three months, for the purpose of comparing expected aftershock hazard regions (positive $\Delta CFS$) with real aftershock locations. Additionally, we analyze the time pattern of the aftershocks evolving towards Campotosto to the north of L'Aquila, and we determine the aftershock decay rate $p$ in the modified Omori's Law (Utsu et al., 1995), whose decay rate coefficients may give information about stress weakening mechanisms involved in the process (Lindman et al., 2006). Our results help to determine whether the L'Aquila aftershock sequence can be explained by pure mechanical processes acting in the region, i.e. static stress transfer, or whether some additional mechanisms might also be operating.

## 4.2 Statistical analysis, Omori's Law

To find the coefficients of the aftershock power law decay rate for the modified Omori's Law (Utsu et al., 1995)

$$R(t) = \frac{k}{(c+t)^p}, \tag{4.1}$$

we investigate how the number of earthquake events per day $R(t)$ decreases with time $t$ after the 06/04/2009 $M_w = 6.3$ L'Aquila main shock. We examine a total of 11,026 seismic events with all magnitudes in the geographic area of 12.92-13.86 longitude and 42.04-42.75 latitude ($30 \times 30$ km$^2$) during the time period from April 6th until August 24th 2009 provided by the Italian Seismological Instrumental and Parametric Data-Base ISIDe (2009).

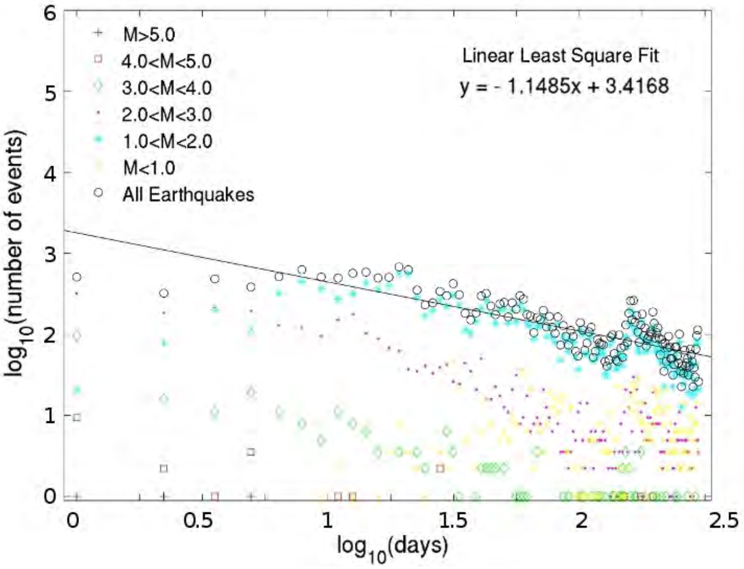

**Figure 4.2:** Aftershocks number per day plotted versus time in logarithmic scale. Black circles show earthquake number for all magnitudes plotted versus time in days together with the linear decay rate fitting. Additionally, colored marks give the number of earthquakes broken down according to their magnitude.

From the fitting results and its residuals for steps of $c = c + 1$ in days for the first 120 hours after the main shock, we recognize that deviations from the linear fit become significantly larger for temporally advanced data. The reason is an increase in seismicity following a $M_w = 4.5$ earthquake to the north of L'Aquila on June 22nd at 20:58 UTC at a depth of 11 km. Looking at the aftershock number through time broken down according to their magnitude (Figure 4.2), we see that the decay rate

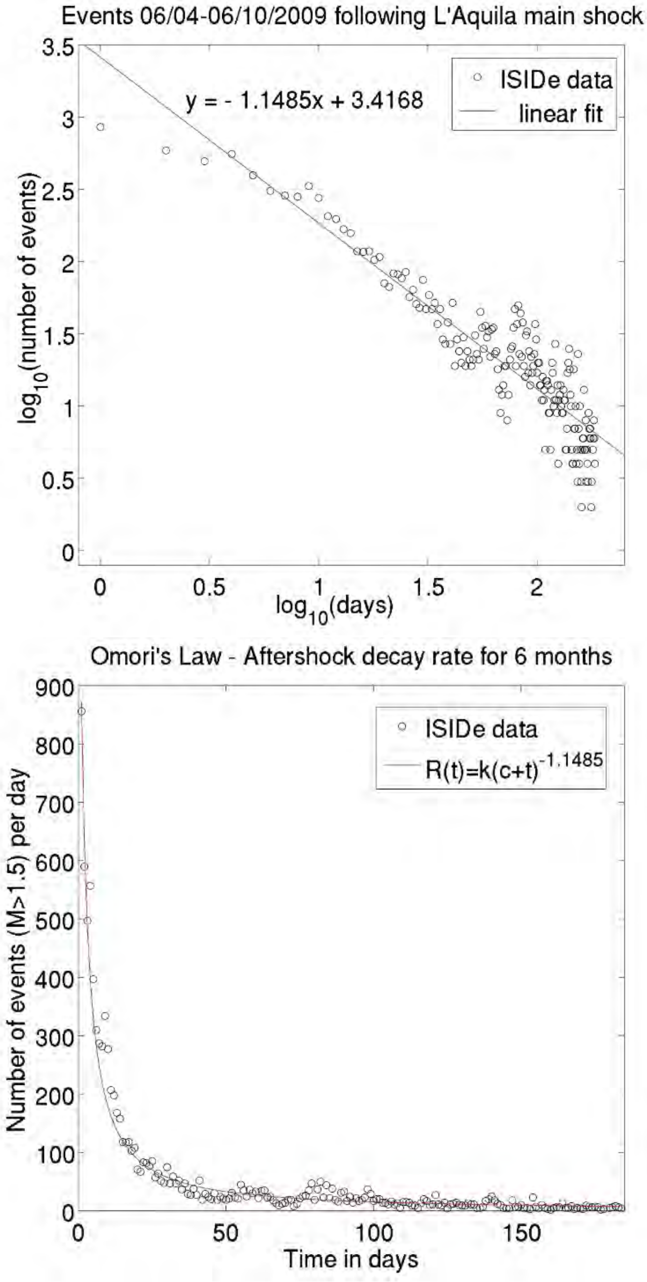

**Figure 4.3:** The aftershock decay rate data-fitting. Black circles show earthquake number for all magnitudes plotted versus time in days. Left: Aftershocks number per day plotted versus time in logarithmic scale. Right: The Omori's Law decay rate function is given as red line ($p = 1.14$ for $c = 0$).

is almost the same throughout the magnitudes. Therefore we are able to specify a magnitude independent resulting decay rate function $R(t)$. The least-square fit to the decay rate data including all earthquake magnitudes (black circles) yields the decay rate $p = 1.14$ for $c = 0$. The according function $R(t)$ is shown as red line in Figure 4.3. The $p$-value close to 1 indicates that the L'Aquila aftershock sequence does not disagree with empirically-observed decay rates.

## 4.3 Spatiotemporal patterns

A total of 20 $M_w > 3.9$ events in the Apennines region are taken as source faults (Table 4.1) for the spatial distribution analysis. These source fault planes were specified in Coulomb 3.1 according to focal mechanism information based on moment tensor solutions provided by Herrmann and Malagnini (2009). Aftershock locations

**Table 4.1:** Events used for stress and dilatation calculations for the multi-fault system. Data based on moment tensor solutions provided by Herrmann and Malagnini (2009).

| Date, Time | Longitude | Latitude | Depth | M | Strike | Dip | Rake |
|---|---|---|---|---|---|---|---|
| 2009-03-30 13:38:38 | 13.3772 | 42.3348 | 11.53 | 4.1 | 10 | 45 | -35 |
| 2009-04-05 20:48:54 | 13.3818 | 42.3398 | 10.20 | 3.9 | 10 | 45 | -35 |
| 2009-04-06 01:32:39 | 13.3340 | 42.3340 | 9.46 | 6.3 | 126 | 35 | -97 |
| 2009-04-06 02:27:46 | 13.3447 | 42.3720 | 0.07 | 4.1 | 175 | 65 | -75 |
| 2009-04-06 02:37:04 | 13.3483 | 42.3727 | 9.62 | 4.8 | 0 | 35 | -50 |
| 2009-04-06 03:56:45 | 13.3367 | 42.3532 | 11.52 | 4.3 | 335 | 30 | -81 |
| 2009-04-06 16:38:09 | 13.3397 | 42.3785 | 9.31 | 4.3 | 0 | 40 | -55 |
| 2009-04-06 23:15:37 | 13.3640 | 42.4510 | 10.80 | 4.9 | 330 | 40 | -90 |
| 2009-04-07 09:26:28 | 13.3930 | 42.3430 | 7.82 | 4.8 | 355 | 30 | -65 |
| 2009-04-07 17:47:37 | 13.5317 | 42.2810 | 14.31 | 5.4 | 340 | 70 | -60 |
| 2009-04-07 21:34:29 | 13.3050 | 42.4087 | 9.45 | 4.2 | 330 | 45 | -70 |
| 2009-04-08 04:27:41 | 13.4692 | 42.3055 | 9.00 | 3.9 | 137 | 73 | -108 |
| 2009-04-09 00:52:59 | 13.3515 | 42.4993 | 10.44 | 5.2 | 145 | 40 | -90 |
| 2009-04-09 03:14:52 | 13.4480 | 42.3455 | 14.25 | 4.2 | 330 | 90 | -55 |
| 2009-04-09 04:32:44 | 13.4438 | 42.4530 | 7.23 | 4.1 | 5 | 55 | -45 |
| 2009-04-09 19:38:16 | 13.3683 | 42.5120 | 10.10 | 4.9 | 135 | 45 | -95 |
| 2009-04-13 21:14:24 | 13.3690 | 42.5063 | 5.77 | 4.9 | 335 | 30 | -80 |
| 2009-04-23 21:49:00 | 13.4943 | 42.2392 | 9.59 | 4.0 | 345 | 35 | -65 |
| 2009-06-22 20:58:40 | 13.3515 | 42.4515 | 11.41 | 4.4 | 320 | 90 | -75 |
| 2009-07-12 08:38:00 | 13.3888 | 42.3382 | 9.64 | 4.1 | 350 | 40 | -65 |

(orange circles) and source faults (red and yellow rectangles) viewed from south-east and north-east on the L'Aquila region are shown in Figure 4.4 (Chiarabba et al., 2009). Most aftershocks cluster near the L'Aquila $M_w = 6.3$ main shock fault, but a second region with significant seismicity can be recognized to the north near the city of Campotosto. For the first cluster at 10 km depth underneath L'Aquila, the aftershock number is very large. Therefore we cannot identify an unambiguous pattern for the time-sequence without arbitrary data filtering.

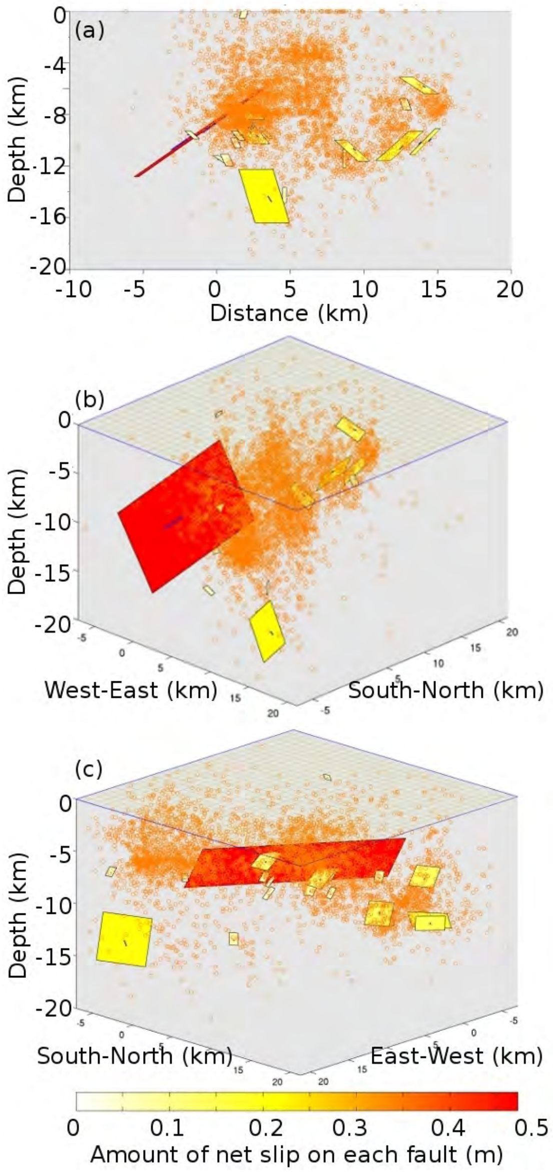

**Figure 4.4:** Spatial distribution of aftershocks. The horizontal axis gives the distance from the red fault center, representing the $M = 6.3$ L'Aquila main shock on 06/04/2009 1:32, the vertical axis is the depth. The smaller events propagate to the north, clustering near Campotosto. Different fault colors give the net slip in meters, estimated from earthquake magnitude-area relations. Cross section view (a) perpendicular to the main fault, (b) from south-east and (c) from north-east.

But the smaller earthquake cluster region underneath Campotosto shows a pattern in the temporal sequence. Screen-shots for the spatiotemporal pattern can be seen in Figure 4.5. After a large earthquake, smaller events occur above the slipped fault.

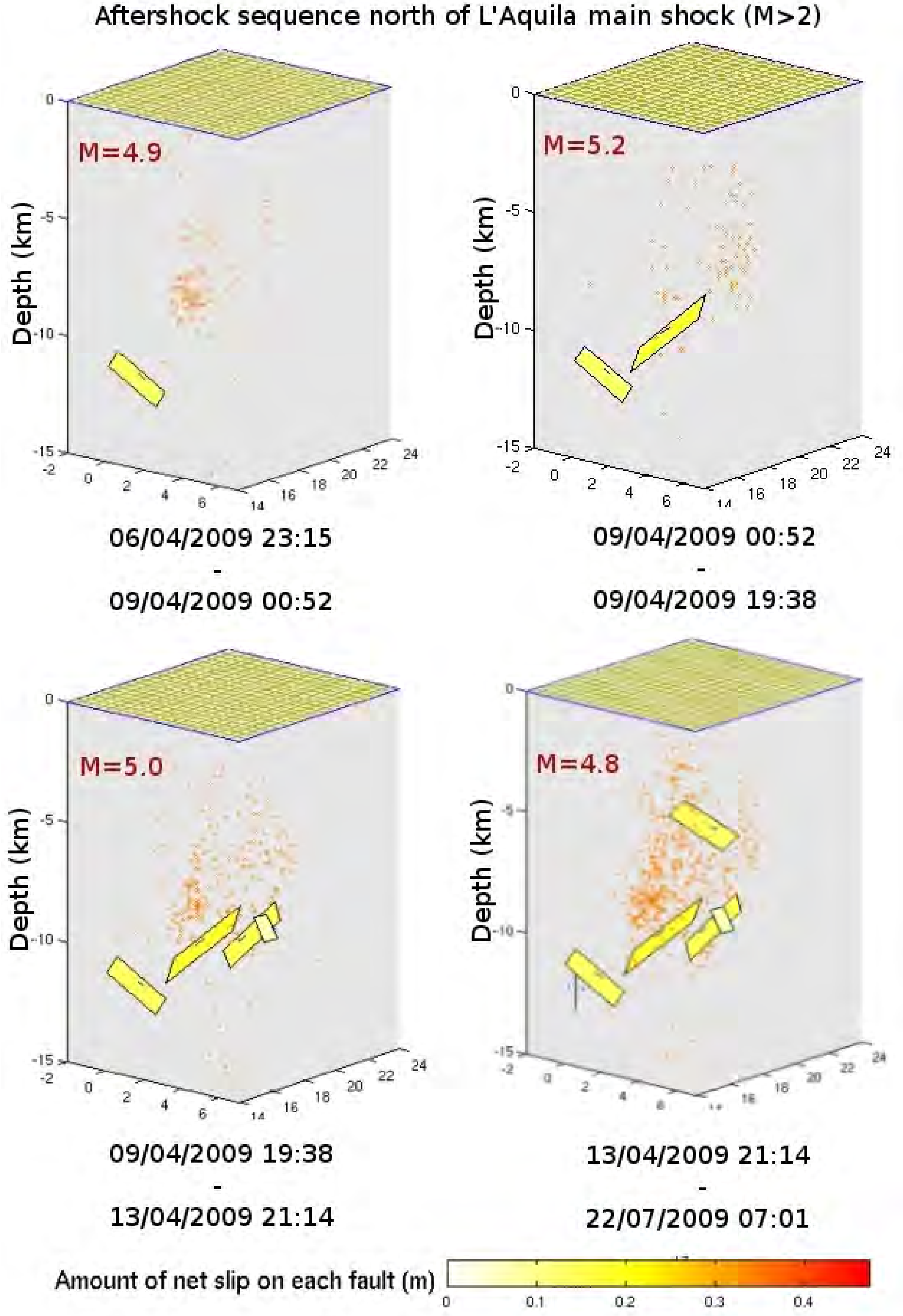
Aftershock sequence north of L'Aquila main shock (M>2)
M=4.9
M=5.2
M=5.0
M=4.8
Depth (km)
0
-5
-10
-15
-2
0
2
4
6
14
16
18
20
22
24
06/04/2009 23:15 - 09/04/2009 00:52
09/04/2009 00:52 - 09/04/2009 19:38
09/04/2009 19:38 - 13/04/2009 21:14
13/04/2009 21:14 - 22/07/2009 07:01
Amount of net slip on each fault (m)
0
0.1
0.2
0.3
0.4

**Figure 4.5:** The spatiotemporal pattern of the Campotosto aftershock cluster (not equal time steps). Aftershocks with $M > 4$ (yellow rectangles) trigger smaller events (orange dots) in the hanging wall. Video screen-shots created with the data overlay tool Jzeemap0.3 (Schaefers, 2009).

## 4.4 Stress and dilatation calculations

For Coulomb stress change and dilatation investigation we use the Coulomb 3.1 software (Lin and Stein, 2004; Toda et al., 2005) provided by the United States Geological Survey, which calculates static stress and strain changes caused by fault slip in an elastic half-space with uniform isotropic elastic properties (Okada, 1992). As input parameters we use $\nu = 0.25$ for Poisson's ratio, $E = 80$ GPa for Young's modulus, so the shear modulus is $G = \frac{E}{2(1+\nu)} = 32$ GPa, and an effective friction coefficient of $\mu = 0.6$. We calculate Coulomb stress change

$$\Delta CFS = \Delta\tau + \mu\Delta\sigma_n, \tag{4.2}$$

with shear stress $\tau$ and normal stress $\sigma_n$, and dilatation

$$\varepsilon_{xx} + \varepsilon_{yy} + \varepsilon_{zz} \tag{4.3}$$

caused by four different fault scenarios (Anzidei et al., 2009; Cirella et al., 2009; Herrmann and Malagnini, 2009; Walters et al., 2009) on the predominating south-east striking, south-west dipping normal faults in this region (Boncio et al., 2004).

We avoid including arbitrary regional stress state assumptions. Strike, dip, and rake are defined following the conventions of Aki and Richards (2002), and the fault plane slip $u$ and dimension $A$ is estimated from empirical moment magnitude-area relations $M_0 = GuA$, except as otherwise stated.

In order to find correlations between expected and real aftershock locations, relocated $M_w > 2.5$ aftershock hypocenters for the period 06/04/2009-22/07/2009 (Chiarabba et al., 2009) within 1 km within each calculation plane are imposed on the obtained $\Delta CFS$ and dilatation model regions.

### 4.4.1 Fault geometry from InSAR

The first L'Aquila fault geometry analysis has been provided by Walters et al. (2009) from InSAR data and body-wave seismology. The $10.75 \times 12.2$ km$^2$ fault was recognized as a 144° striking, 54° south-west dipping fault with a rake of -105° and an average slip of 0.66 m. In that study, Coulomb stress change calculations were shown to support the suggested earthquake source model, as the positive $\Delta CFS$ to the north-west of L'Aquila could explain the influence on the Campotosto region.

In our calculations, we find similar results for aftershocks to the north and south very close to the main fault (Figure 4.6). But the aftershocks directly above the hypocenter cannot be explained entirely as they are in negative $\Delta CFS$ regions.

We also find that the Campotosto fault system is too far distant to be directly influenced by the main shock. Our calculations on the dilatation due to the main shock fault, which is independent of the regional stress state, show that the aftershock locations coincide well with borders of maximum and minimum dilatation.

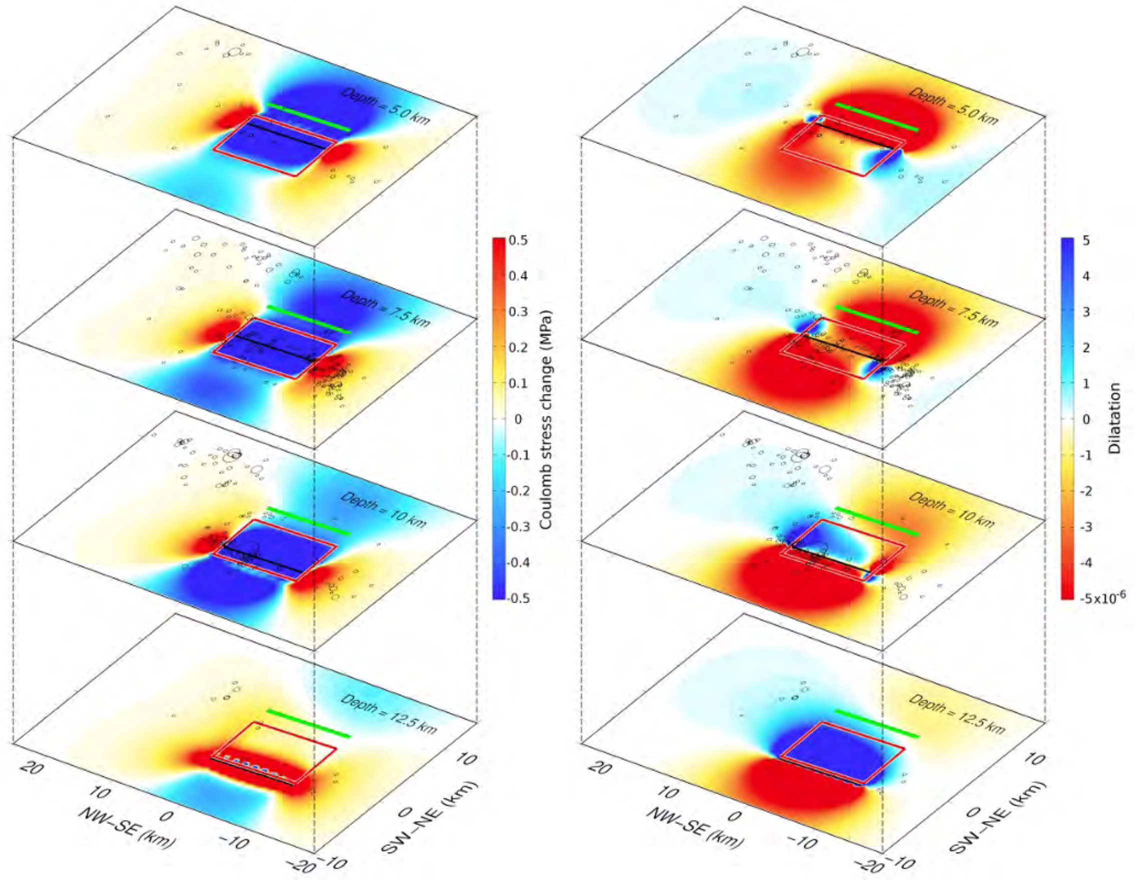

**Figure 4.6:** Fault source model inferred from InSAR and its influence on the Apennines region. Sliced views on the Coulomb stress change (left) and dilatation (right) in 5, 7.5, 10 and 12.5 km depth. Aftershocks to the east and west are in decreased stress regions and are situated on borders between high and low dilatation.

Walters et al. (2009) fault geometry is appropriate to explain aftershock triggering by static stress transfer, but the results on dilatational effects also allow the presence of fluids in the process.

### 4.4.2 GPS source modeling

Anzidei et al. (2009) suggest a source model for the L'Aquila earthquake due to co-seismic deformations gained from GPS data. The main shock fault is given with strike 130°, SW-dip 55.3° and rake -98°. The size of the fault is estimated as 13 km length and 15.7 km width with an average slip of 0.49 m.

Figure 4.7 shows the Coulomb stress changes and dilatation results using these parameters. The lower strike angle produces results clearly different from these shown above. The aftershocks are located in regions with negative $\Delta CFS$, except for very shallow regions (see depth=5 km) and the fault edges. Thus, static stress transfer as aftershock generation process is not appropriate for this fault geometry.

On the other hand, the results on the dilatation show up similarities to the former case. Here, the aftershocks also cluster in regions between significantly high and low dilatation.

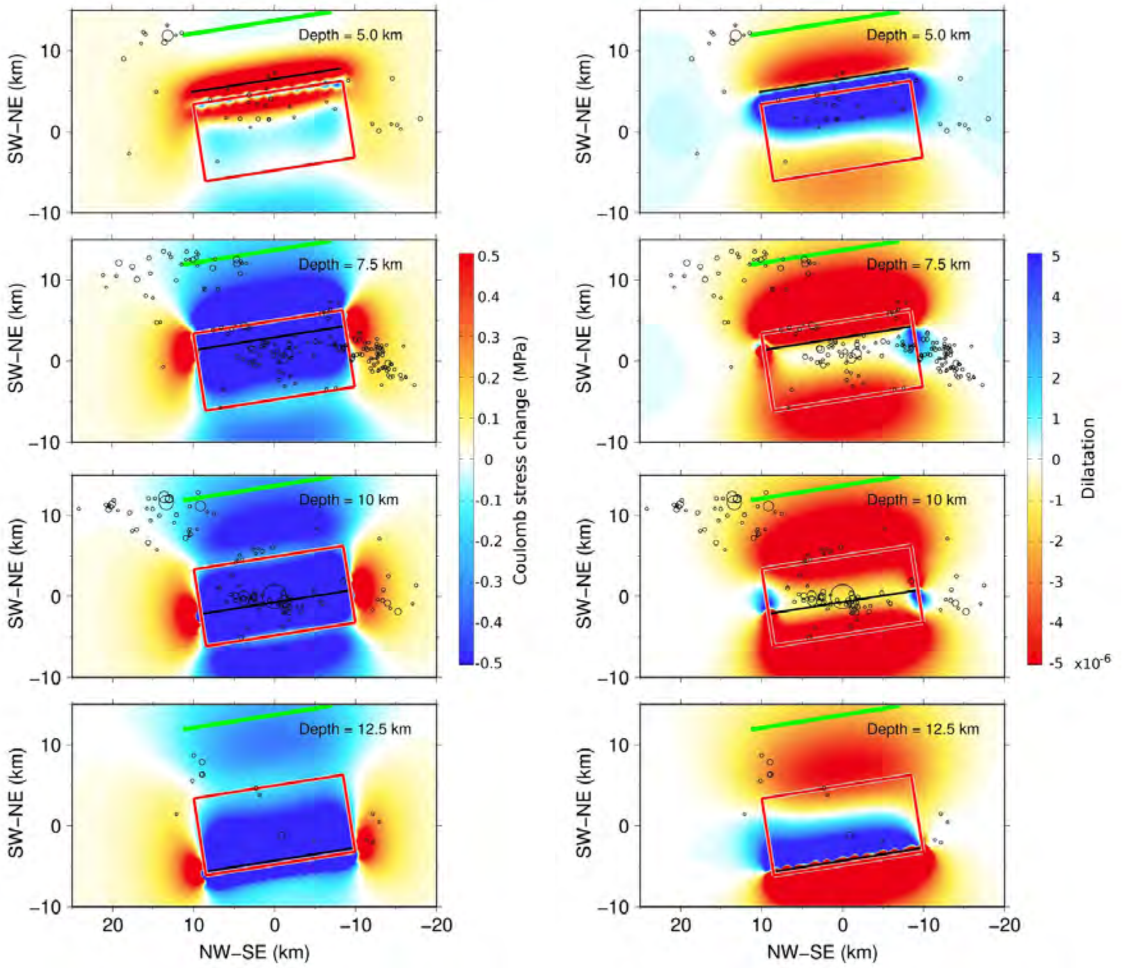
Depth = 5.0 km
Depth = 7.5 km
Depth = 10 km
Depth = 12.5 km
SW–NE (km)
NW–SE (km)
10
0
−10
20
10
0
−10
−20
Coulomb stress change (MPa)
0.5
0.4
0.3
0.2
0.1
0
-0.1
-0.2
-0.3
-0.4
-0.5
Dilatation
5
4
3
2
1
0
-1
-2
-3
-4
-5
x10-6

**Figure 4.7:** Fault source model inferred from GPS data. Top views of stress (left) and dilatational (right) effects in depths of 5, 7.5, 10 and 12.5 km are superposed with $M_w > 2.5$ aftershocks. Most aftershocks lie in negative $\Delta CFS$ regions and occur between max. and min. dilatation values.

### 4.4.3 Fault with non-uniform slip distribution

The most realistic, but most complicated source models arise from non-uniform slip fault models. We investigate the geometry suggested by Cirella et al. (2009) and subdivide the fault in five regions with different slips, decreasing towards the fault edges. The fault size and location was gained from non-linear joint inversion of strong motion and GPS data. The adopted fault is 133° striking, 54° SW-dipping with dimensions of 17.5 times 28 km. The maximum slip at the main shock hypocenter is 1.1 m and decreases towards the edges of the fault.

Our calculations show that for a non-uniform slip fault, the positive $\Delta CFS$ regions coincide well with aftershocks at depth. More shallow events with depths $< 10$ km occur in regions with positive as well as in regions with negative stress change. The results for dilatational effects again underline the former results - locations are obviously on borders of maximum and minimum dilatation.

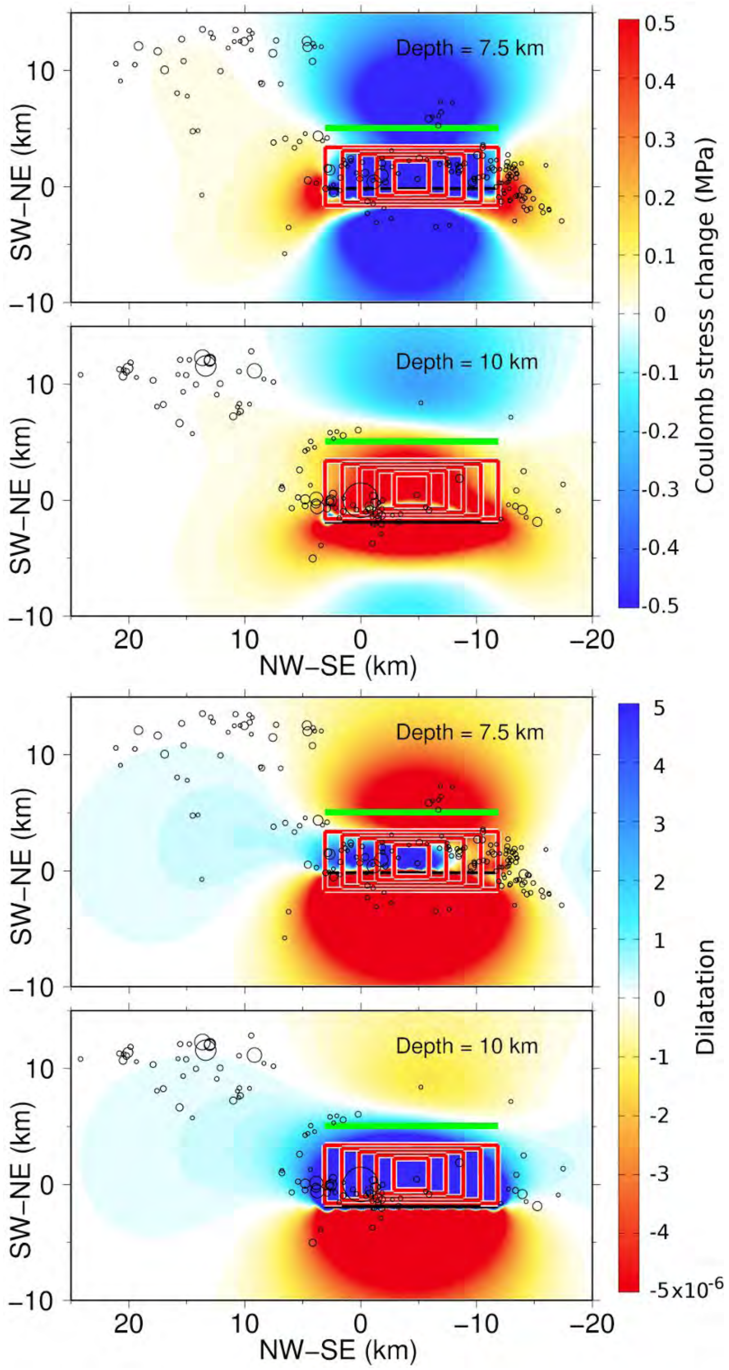

**Figure 4.8:** Fault source model with non-uniform slip adopted from Cirella et al. (2009). Views for 7 and 10 km depth. Only deep earthquakes match well with static stress transfer assumptions (left). Earthquakes occur between high and low dilatation regions (right).

### 4.4.4 Multi-fault system

We analyze the $\Delta CFS$ and dilatation for the L'Aquila earthquake specified according to focal mechanism information based on moment tensor solutions provided by Herrmann and Malagnini (2009). A total of 20 $M_w > 3.9$ events in the Apennines region (including the south-west dipping $M = 6.3$ L'Aquila main shock) are taken as source faults with uniform slip (Table 4.1).

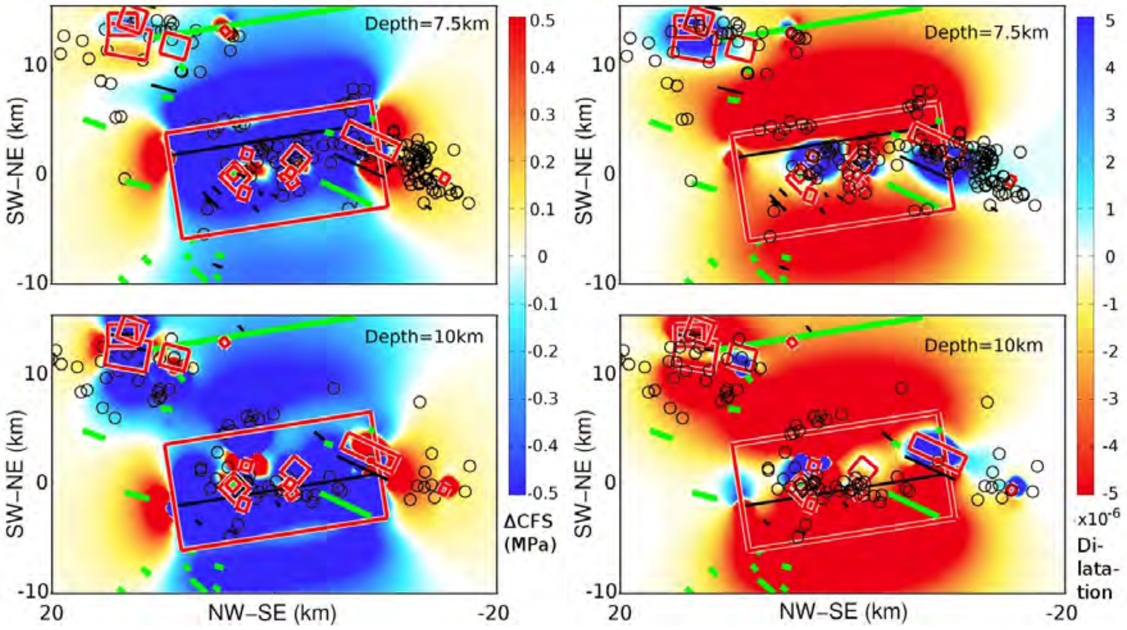

**Figure 4.9:** Coulomb stress change $\Delta CFS$ (left) and dilatation (right) as map view of the region produced by the multi-fault system at 7.5 km and 10 km depth. Red rectangles show the locations and sizes of the source faults, black circles indicate the aftershock locations.

Our results are shown in Figure 4.9 for the map view calculated at depth of 7.5 km and 10 km. Aftershocks are located in regions with positive as well as negative $\Delta CFS$. Significantly, however, aftershocks appear to lie on the boundary between maximum and minimum dilatation. Viewed as cross-section perpendicular to the fault strike in the direction of NE-SW passing the hypocenter of the main-shock (Figure 4.10), we cannot recognize, except for the shallow events, any correlations between aftershocks and positive Coulomb stress change. For dilatation, however, the earthquakes tend to cluster in compressional regions, especially the larger seismic events with $M \geq 4.0$.

### 4.4.5 Results at depth

Finally, we analyze Coulomb stress changes and dilatation for the L'Aquila main fault with respect to depth. The different fault models and geometries yield similar results. Due to space reasons, we present cross section views for the multi-fault system, exemplifying all cases above.

Figure 4.10 shows cross-sections of the $\Delta CFS$ and the dilatation perpendicular to the fault in the direction of NE-SW, passing through the hypocenter of the main shock. The view is from south-east towards north-west. Red lines show the fault, orange circles are the aftershock locations within 5 km from the cross-section. The horizontal axis gives the distance from the $M = 6.3$ L'Aquila main shock epicenter, the vertical axis is the depth.

We find that static stress transfer does not satisfactorily explain this aftershock sequence. Only shallow earthquakes, lying in the elongation of the main shock fault, match the positive stress changes. Most events are located in regions where $\Delta CFS$ decreases. The dilatation result features the same characteristics as seen in the results for the top views. The aftershocks cluster in regions where diffusion of fluids is probable.

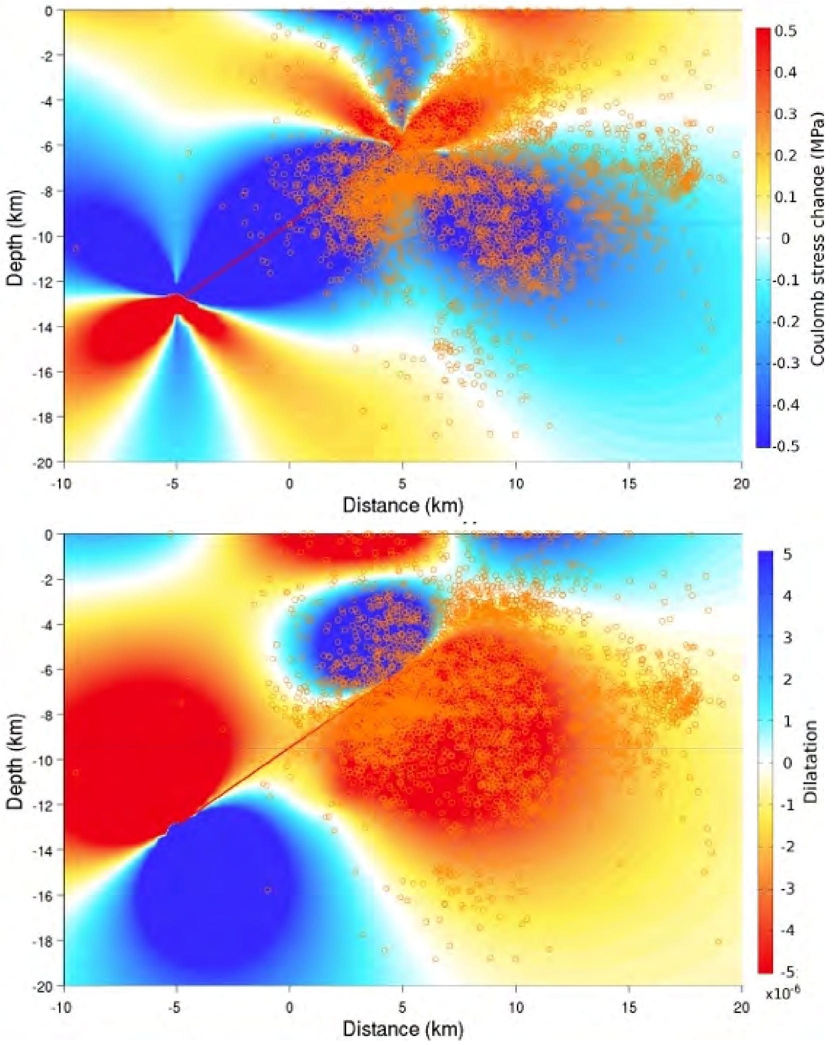

**Figure 4.10:** Cross-section view from south-east on the regional changes caused by the multi-fault system. Coulomb stress change on left and dilatation on right.

## 4.5 Discussion and Conclusions

In this study, we estimated the spatiotemporal distribution of aftershocks and the expected Coulomb stress change and dilatation due to different fault scenarios for the L'Aquila 2009 earthquake (Italy). Our results show a magnitude independent aftershock decay rate that obeyed a typical Omori Law with an expected decay rate ($p$-value) close to $p = 1$. The spatiotemporal pattern of the aftershock location significantly cluster in the L'Aquila and Campotosto region. Especially the Campotosto cluster shows a breaking-seals-like formation through time. Except for the fault source model suggested by Walters et al. (2009), the aftershock hypocenter locations do not significantly correlate with positive Coulomb stress changes caused by the underlying main shock fault scenarios. Events occur in areas with elevated stresses as well as in regions with negative $\Delta CFS$. But earthquakes following the April 6th main shock show a very strong correlation with regions between positive and negative dilatation.

These findings do not support Coulomb stress transfer as a driving mechanism for the L'Aquila earthquake. The evolution of aftershock locations indicate that aftershocks behave similar to the 1997 Colfiorito earthquake sequence, lying in the same geological setting, known for being driven by trapped high pressure fluids (Miller et al., 2004). We suggest the L'Aquila aftershock sequence to be driven in part by fluid flow associated with volumetric compression and by the diffusion of high pressure fluids from a deep source, initialized by fracturing due to the main shock. For these reasons, the presence of fluids in the L'Aquila earthquake generation should be considered in future studies (Nur and Booker, 1972; Bosl and Nur, 2002).

# Chapter 5

# Coupling Degassing with Lava Dome Extrusion and Periodic Seismicity for the 2004 Eruption of Mount St. Helens

Observing seismic events at the Cascade Volcanic Arc in western North America is not unusual since volcanic activity is mostly accompanied by earthquakes. But the continuous shallow “drumbeat” seismicity associated with volcanic extrusion of a lava dome at Mount St. Helens was exceptional. Occurring over a 15 month period, the magnitude $M \approx 2$ earthquakes showed a striking periodicity suggesting a continuous source. This process was previously modeled as a dry system with highly non-linear friction to simulate the observed periodic behavior (Iverson et al., 2006). More recent studies of the seismic source associated with these events show that they are related to the generation of long-period earthquakes due to volumetric changes (Waite et al., 2008), suggesting that fluids play an important role in their genesis. We expand the model of Iverson to include the effects of fluids using simple Coulomb friction and effective stress. We demonstrate that since the governing equations have the form of an oscillator, periodicity is a natural result. Period, amplitude and damping are controlled by fault gouge characteristics, fluid properties and initial conditions on the plug. The advantage of this formulation is that complex rheological models are not necessary, and allows the effects of trapped fluid overpressure generated by degassing magmas into the problem. Including effects of fluids also allows for potential relationship to observed $CO_2$ and $SO_2$ degassing events.

## 5.1 Introduction

After years of relative rest since the 1980 explosive eruption of Mount St. Helens (MSH), its revived activity intensified monitoring and research in the region (Scott et al., 2008). Renewed MSH activity began on September 23, 2004 with a shallow earthquake swarm $0 - 2$ km beneath the old lava dome surface. Over the next two weeks, seismicity increased in magnitude and event rate, resulting in five phreatic eruptions from October 1-5, 2004 (Dzurisin et al., 2005), releasing ash, steam plumes and magmatic gases ($CO_2$, $H_2S$ and $SO_2$). By October 11, with the beginning of the new lava dome growth, earthquakes again decreased in magnitude, but showed remarkable periodicity of nearly $30 - 300$ s between the events (Moran et al., 2008). Their origin at depths $< 1$ km was situated directly beneath the new emerging dome. For the next 14 months, this shallow low-frequency seismicity remained

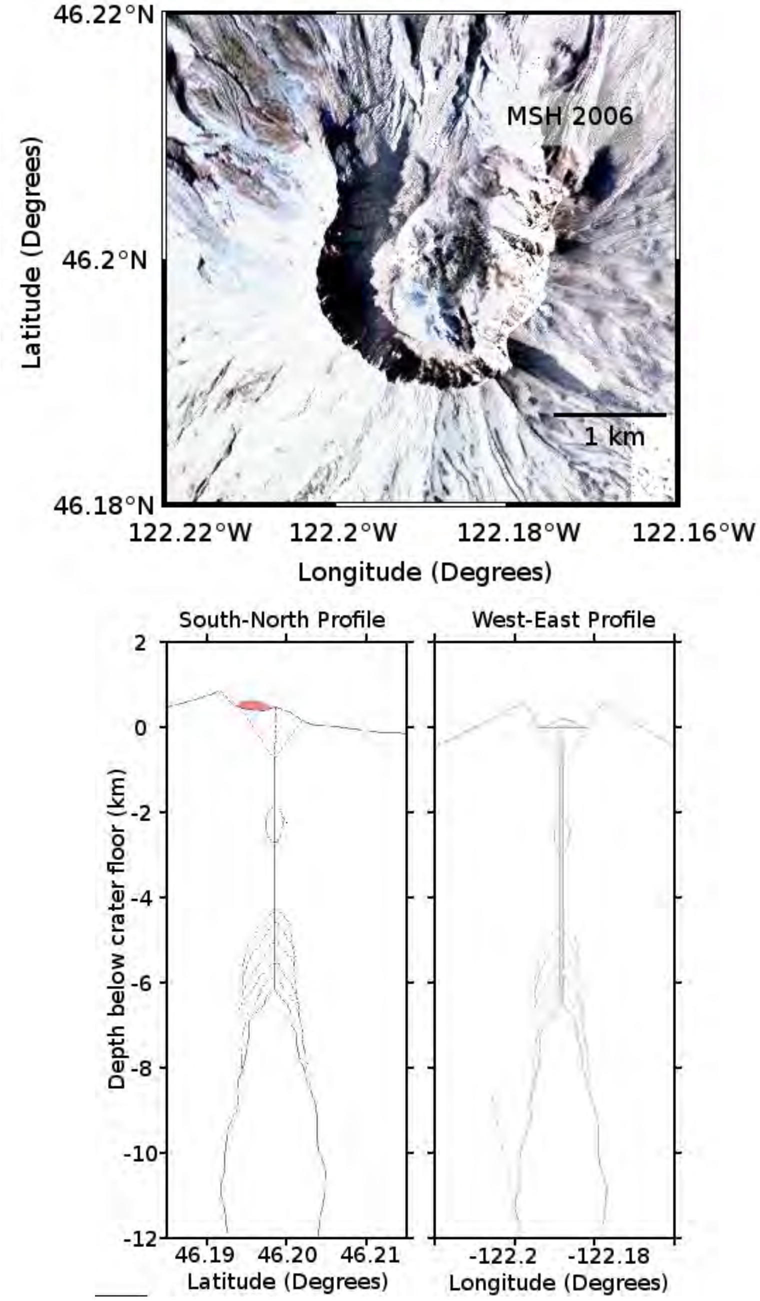
46.22°N
MSH 2006
Latitude (Degrees)
46.2°N
1 km
46.18°N
122.22°W
122.2°W
122.18°W
122.16°W
Longitude (Degrees)
South-North Profile
West-East Profile
2
0
-2
-4
-6
-8
-10
-12
Depth below crater floor (km)
46.19
46.20
46.21
Latitude (Degrees)
-122.2
-122.18
Longitude (Degrees)

**Figure 5.1:** Top view of Mount St. Helens crater and north-south and east-west conduit profiles. The new 2006 lava dome is accentuated. Figures adopted from PNSN (2010).

unchanged (incidental larger earthquakes did not disturb this behavior), and the extrusion rate remained almost constant ($1 - 2$ m$^3$ s$^{-1}$) with the formation of the new lava dome (Iverson, 2008). The average gas emission rate reached 750 td$^{-1}$ (Dzurisin et al., 2005). The striking earthquake periodicity, which does not follow a Gutenberg-Richter magnitude-frequency distribution, indicates a persistent seismic source present at a certain depth over an extended period.

Iverson et al. (2006) proposed a model for the observed volcanic activity in 2004-2005 and coined the acronym SPASM: "Seismogenic Plug of Ascending Solidifying Magma". The model, describing the motion of a plug of solidified magma inside the conduit driven by magma volume and pressure, linked the simultaneous characteristics of periodically occurring seismic events and the linear extrusion rate of the lava dome. An empirical rate-dependent friction rule was proposed to damp the system of equations, which have a natural tendency to oscillate. The computational results produced a regular stick-slip plug displacement behavior with time cycles, reproducing the seismicity period and amplitudes, and good fits to the rate of lava dome growth. However, in later studies the shallow seismic events were identified as long-period (LP) earthquakes with dilatational first motions (Waite et al., 2008), indicating a volumetric source to account for the drumbeat response generation. These LP sources were modeled as a fluid-filled crack and dike/sill system, and although this model generally fits observations, other complexities to the source such as degassing along dendritic paths at plug-conduit boundary were also identified as potentially important. Cyclicity at the Soufrière Hills Volcano (SHV), Montserrat (Lensky et al., 2008) was modeled as a depressurizing/repressurizing system similar to our approach, but did not consider extrusion of a lava dome in the problem.

In this study, we revisit the SPASM model (Iverson et al., 2006) to determine whether the observations might also be explained by an alternative model that includes fluid pressure variations combined with a simple friction law. We show that fluid pressure and effective normal stress changes, combined with a simple friction model, also reproduces the observed cyclicity. This alternative mechanistic explanation for the drumbeat seismicity allows for the migration of trapped high pressure fluids (e.g. magmatic gas) towards the surface, consistent with the observation of degassing events at MSH during the activity period (Dzurisin et al., 2005).

## 5.2 Conceptual model and system equations

The long time-scale cyclicity in lava dome extrusion related to degassing of magma bodies was modeled by Barmin et al. (2002) or Melnik and Sparks (1999) for open conduit systems and ascending magmas, where the seismic response was mainly produced by fragmentation processes. Lensky et al. (2008) proposed a set-up similar to the SPASM model for the plugged conduit at Soufrière Hills Volcano (SHV), showing that exsolution of water-rich magma produces periodic pressurization in cycles of 36 hours. However, at SHV the seismic cyclicity was often interrupted and changed repeatedly over time, making the comparison between observation and model results difficult. In the model proposed here, we include a simple model of magmatic gas migration to the mechanical plug extrusion model of Iverson et al. (2006), thereby including effective stress concepts and simple Coulomb friction. The results show periodic behavior, with time ranges of seconds and minutes for plug displacement and seismicity cycles.

Figure 5.2 shows the modified model set-up based on the SPASM model (Iverson et al., 2006). We use the subscripts *m* for magma, *f* for fluid and *s* for solid plug throughout this chapter to distinguish between magma, fluid and solid properties.

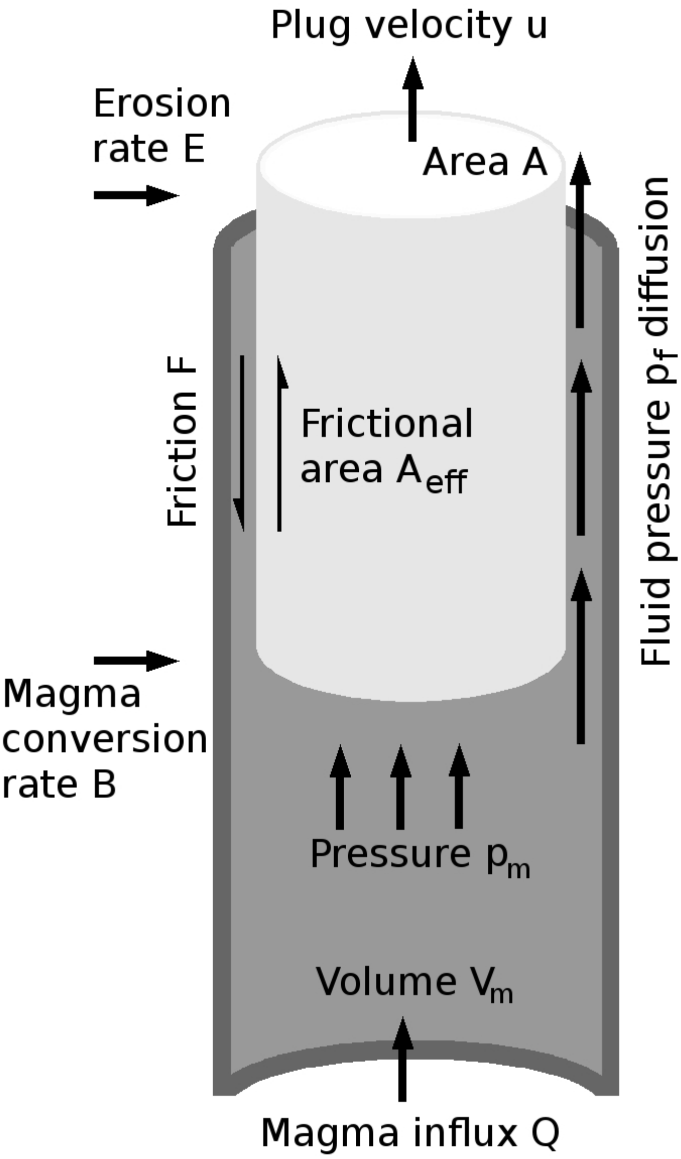
Plug velocity u
Erosion rate E
Area A
Fluid pressure $p_f$ diffusion
Friction F
Frictional area $A_{eff}$
Magma conversion rate B
Pressure $p_m$
Volume $V_m$
Magma influx Q

**Figure 5.2:** The model sketch (not to scale, based on (Iverson et al., 2006)) showing the upper 2 km of a volcanic conduit, plugged by solidified magma. The magma pressure driven plug ascend is resisted by a friction force, including the concept of effective stress.

The volcanic conduit of 8 km depth is filled with ascending magma of volume $V_m$, entering from a lower source at a constant influx rate $Q$. In the upper part of the conduit, the magma exerts pressure $p_m$ on the horizontal bottom cross-sectional area $A$ of a dacide plug with density $\rho_s$ of solidified magma, forcing the plug to move upwards. The velocity $u$, observed as extrusion rate at the vent, is resisted by the plug weight $mg$ and the friction force $F$ along the conduit wall, where $m$ is the plug mass and $g$ acceleration due to gravity. The initial plug mass $m_0$ is allowed to increase linearly with time $t$ at a constant rate $\kappa$ due to magma solidification and accretion at the bottom of the plug $B$, and to decrease from surface erosion $E$. For magma of density $\rho_m$, the magma compressibility is defined as

$$\alpha_1 = \frac{1}{\rho_m}\frac{d\rho_m}{dp_m}, \tag{5.1}$$

and, for the special case $u = 0$ and $B = 0$, the elastic compliance of the conduit walls is

$$\alpha_2 = \frac{1}{V_m}\left[\frac{dV_m}{dp_m}\right]_{u=0,B=0}. \tag{5.2}$$

The resulting system of equations for the evolution of the state variables for plug velocity $u$ and magma pressure $p_m$ and volume $V_m$ is described by

$$\frac{du}{dt} = -g + \frac{1}{m_0 + \kappa t}\left(p_m A - \kappa u - F\right) \tag{5.3}$$

$$\frac{dp_m}{dt} = -\frac{1}{V_m\left(\alpha_1 + \alpha_2\right)}\left(Au + \left(1 - \frac{\rho_m}{\rho_s}\right)B - Q\right) \tag{5.4}$$

$$\frac{dV_m}{dt} = \frac{\alpha_1}{\alpha_1 + \alpha_2}\left(Au + \left(1 - \frac{\rho_m}{\rho_s}\right)B - Q\right) + Q - B. \tag{5.5}$$

The derivation of this system of equations from mass and momentum conservation laws for solid plug and magma is given in Iverson (2008) and is not repeated here. We introduce fluids into the system of equations by considering degassing of magma body as fluid source, and therefore (1) consider changes to the continuity equations for plug and magma, (2) complete the system by conservation laws for the gaseous fluid and (3) introduce an appropriate friction rule $F$ in Equation (5.3). In Equations (5.4) and (5.5), we use the convex combination $B = \lambda S + (1-\lambda)G$, where $0 \leq \lambda \leq 1$, instead of the constant volumetric magma conversion rate $B$ in order to distinguish between the liquid/solid $S$ and the liquid/gas $G$ phase changes. With the explicit relationship

$$\frac{1}{\rho_m} = \frac{1-\lambda}{\rho_f} + \frac{\lambda}{\rho_s} \tag{5.6}$$

between magma, fluid and solid densities in a volcanic system (Huppert and Woods, 2002; Wilson et al., 1980), we replace $(1 - \frac{\rho_m}{\rho_s})B$, given as the instantaneous liquid/

solid magma phase change with concomitant mass accretion at the base of the plug, with

$$\Big(1-\frac{\rho_m}{\rho_f}\Big)(1-\lambda)G+\Big(1-\frac{\rho_m}{\rho_s}\Big)\lambda S. \tag{5.7}$$

The chosen shorthand for the constant plug mass change rate $\kappa$ in Equation (5.3) becomes

$$\kappa=\rho_m\lambda S-\rho_s E. \tag{5.8}$$

Note that $S=B$ follows from the non-degassing case $\lambda=1$, and all equations take the original form. Keeping these adjusted terms constant as proposed by Iverson (2008), we avoid arbitrary assumptions on the new quantities.

We combine mass conservation for the fluid, produced by magma degassing underneath the solidified plug with mass production rate $[\rho_m(1-\lambda)G]_{v=0}$ at no-flow-conditions, with momentum conservation given by Darcy's Law

$$v=-\frac{k}{\eta}\frac{dp_f}{dz} \tag{5.9}$$

for vertical viscous fluid flow with velocity $v$ through the permeable gouge material between the solidified plug and conduit walls towards the free surface. This results in a diffusion type equation with a source term (Miller and Nur, 2000):

$$\frac{dp_f}{dt}=\frac{k}{\eta\beta_f}\frac{d^2p_f}{dz^2}+\left[\frac{\rho_m(1-\lambda)G}{\beta\rho_f V_f}\right]_{v=0}. \tag{5.10}$$

Here, $p_f$, $\eta$ and $\beta_f=\frac{1}{\rho_f}\frac{d\rho_f}{dp_f}$ are the fluid pressure, viscosity and compressibility, respectively, $k$ is the gouge material permeability, $z$ is the vertical coordinate and the last term represents the fluid pressure source term with fluid density $\rho_f$ and volume $V_f$ at no-flow-conditions ($v=0$). As simplifications, we assume steady-state fluid volume and gouge material properties and no changes in fluid density and gouge permeability with position. Furthermore, Dalton's Law of partial pressures $p_f=\sum_i^n p_{f,i}$ allows to examine the fluid pressure without distinguishing between its different components (i.e. $CO_2$, $H_2S$, $SO_2$ etc.).

When fluid flow towards the surface is zero, the conduit beneath the solidified plug represents a closed system and a vapor-liquid-equilibrium for the phase transition between magma and magmatic fluid can be assumed, resulting in the isothermal relationship $[p_f]_{v=0}=[p_m]_{v=0}$ (Poling et al., 2000). At the same time, the diffusion term in Equation (5.10) disappears reducing to $\left[\frac{dp_f}{dt}\right]_{v=0}=\left[\frac{\rho_m(1-\lambda)G}{\beta\rho_f V_f}\right]_{v=0}$, and therefore we can replace the fluid source term with magma pressure change rate where necessary.

For the friction rule in Equation (5.3), we replace the empirical nonlinear rate-dependent dry friction function given by Iverson et al. (2006) with a generalized Coulomb-type friction law including fluid pressure via Terzaghi's effective stress (Terzaghi, 1943)

$$\sigma_{\text{eff}}=\sigma_n-p_f. \tag{5.11}$$

In this model, cyclicity arises naturally from the dynamical nature of fluid pressure variations. That is, fluid pressure increases from the degassing magma reduce the effective normal stress, triggering frictional failure. Slip at failure is accompanied by dilation, which reduces the fluid pressure and cycle repeats. This principle has been used previously in numerical earthquake models (Freed, 2005; Miller, 2002; Miller et al., 1996), and is also feasible for slip and extrusion of the magmatic plug. The fluid pressure dependent Coulomb-type friction rule is

$$F = \mu A_{\text{eff}} \left(\sigma_n - p_f\right) \tag{5.12}$$

with normal stress $\sigma_n$, i.e. the lateral stress acting perpendicular to the plug and conduit walls, constant friction coefficient $\mu$ and effective frictional area $A_{\text{eff}}$ between plug and conduit wall. The normal stresses acting on conduit walls are not easy to constrain, so we assume an earth pressure coefficient $K$ (Fang and Daniels, 2006; Powrie, 2004), and substitute the stress normal to the friction failure plane $\sigma_n$ with the vertical stress $\sigma_n = K\sigma_z$, produced by the lithostatic pressure $\sigma_z = \rho_r g z$ per unit area. We complete Equation (5.3) with

$$F = \mu A_{\text{eff}} \left(K\rho_r g z - p_f\right) \tag{5.13}$$

as friction rule.

With these changes, we can study the effects on the SPASM model by introducing a degassing component as an additional physical process of the MSH volcanic extrusion.

## 5.3 Model results

In order to compare the results shown in Iverson (2008) with these produced here, we use the same parameter values for the governing equations as stated there. Further MSH quantities are based on Moore et al. (2008), Pallister et al. (2008) and Scott et al. (2008). All parameters are listed in Table 5.1.
About 8000 s into the simulation, we obtain negative velocity solutions, and therefore negative displacements (Figure 5.4(a)). However, the long term velocity behavior is not affected because the velocity oscillation increases with time and finally saturates at $t \approx 1.14\times10^6$ s, with values between $u \approx 8.27\times10^{-4}$ m s$^{-1}$ and $-6.93\times10^{-4}$ m s$^{-1}$ (Figure 5.4(b))). The mean of the average extrusion rate of about $\bar{u} = 6.67 \times 10^{-5}$ m s$^{-1}$ is in agreement with the observations at MSH.

We calculate and present the results for the displacement of the solid plug as a function of time, which we assume is the underlying mechanism responsible for the observed drumbeat earthquakes. As shown below, our model qualitatively reproduces the results of Iverson (2008) and also permits the full range of observed drumbeat frequencies to be generated by variations in solid and fluid properties.

Figure 5.3(a) shows the calculated plug displacement for the entire period of observed periodic earthquakes of 15 months, i.e. $40 \times 10^6$ s, obtained by (time-)integration

**Table 5.1:** Parameter symbols, description and their values used in modeling and for numerical computation. Adopted or calculated from values given in (Iverson, 2008; Moore et al., 2008; Pallister et al., 2008; Scott et al., 2008).

| Symbol | Value | Unit | Definition |
|---|---|---|---|
| $A$ | $3 \times 10^5$ | $m^2$ | max. plug cross-section area |
| $A_{\text{eff}}$ | $6 \times 10^5$ | $m^2$ | max. effective frictional area |
| $\alpha_1$ | $10^{-8} - 10^{-6}$ | $Pa^{-1}$ | magma compressibility |
| $\alpha_2$ | $10^{-9}$ | $Pa^{-1}$ | conduit wall compliance |
| $B$ | $0 - 10$ | $m^3\ s^{-1}$ | volumetric magma phase change rate |
| $\beta_f$ | $10^{-10} - 10^{-9}$ | $Pa^{-1}$ | fluid compressibility |
| $\eta$ | $10^{-5}$ | Pa s | fluid viscosity |
| $g$ | 9.81 | $m\ s^{-2}$ | gravitational acceleration |
| $k$ | $10^{-21} - 10^{-16}$ | $m^2$ | fault gouge permeability |
| $K$ | $0.1 - 1$ | - | earth pressure coefficient |
| $\kappa$ | 4000 | $kg\ s^{-1}$ | max. plug mass change rate |
| $\lambda$ | $0 - 1$ | - | liquid/solid mass fraction |
| $m_0$ | $2 \times 10^9 - 7 \times 10^{10}$ | kg | initial plug mass |
| $\mu$ | $0.4 - 0.6$ | - | coefficient of friction |
| $p_0$ | $10^7 - 10^8$ | Pa | initial conduit pressure |
| $Q$ | $1 - 2$ | $m^3\ s^{-1}$ | magma influx rate |
| $\rho_m$ | $1200 - 2400$ | $kg\ m^{-3}$ | magma bulk density |
| $\rho_s$ | $1600 - 2400$ | $kg\ m^{-3}$ | plug bulk density |
| $u_0$ | $2 \times 10^{-5} - 2 \times 10^{-4}$ | $m\ s^{-1}$ | initial plug velocity |
| $V_0$ | $10^8 - 10^{11}$ | $m^3$ | initial magma volume |

of the plug velocity solution $u$. We observe that the total displacement of the plug is more than 2500 m (considered from a reference point on the earth surface), corresponding to an average extrusion rate velocity $\bar{u} = 6.67 \times 10^{-5}$ m s$^{-1}$ and a total lava dome volume of $74 \times 10^6$ m$^3$, as measured at MSH (Iverson et al., 2006). In the close-up Figures 5.3(b) and 5.3(c), the displacement behavior for two different time intervals can be compared: Figure 5.3(b) shows that in the beginning the plug moves up abruptly some 9 mm at each motion cycle with a constant period of about 130 s, consistent with the range of recorded earthquake periodicity and with the results obtained by Iverson et al. (2006, Figure 5(a)). Figure 5.3(c) shows quite different behavior: the plug moves up, but then falls slightly, while retaining the period and upward displacement differences as seen above. This deviation from the original SPASM behavior becomes clear when examining the velocity solution shown in Figure 5.4.

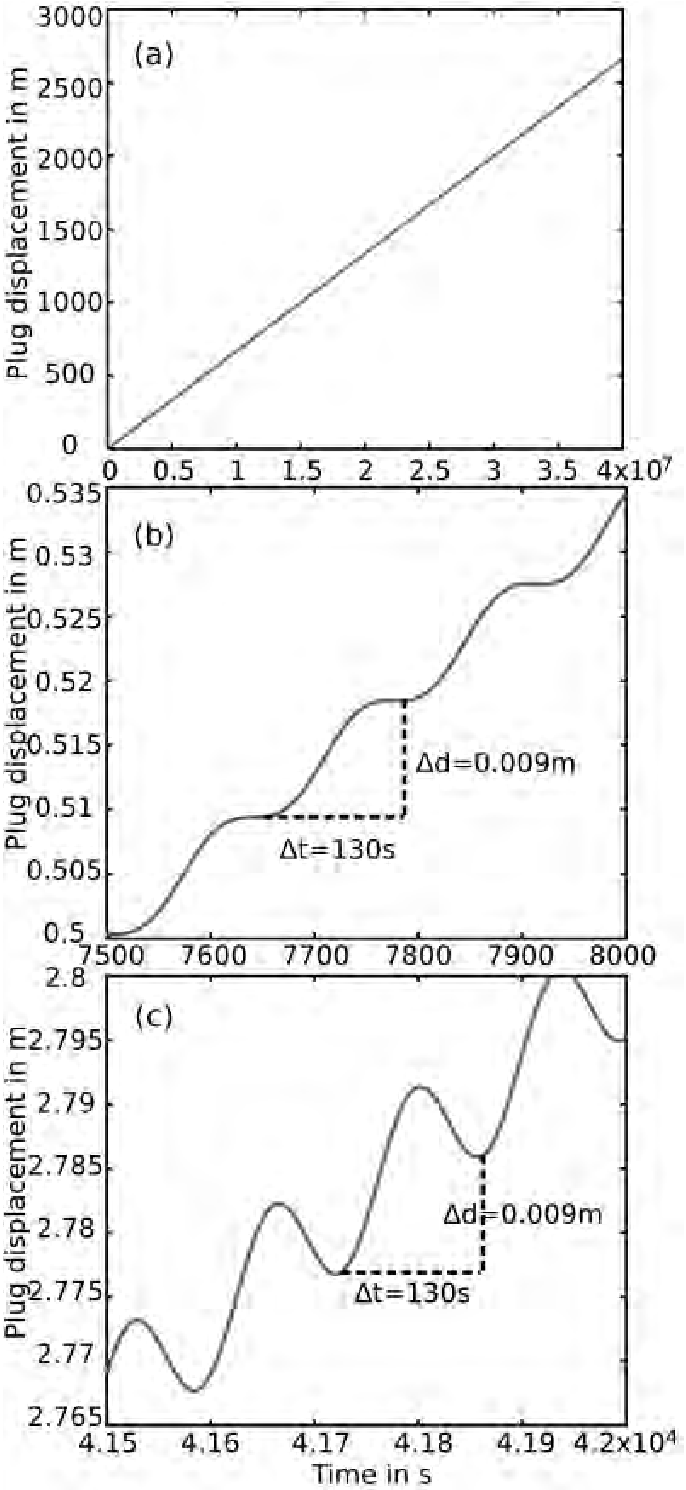

**Figure 5.3:** (a) Plug displacement calculation for 15 months of MSH activity. Plot indicates the linearity of the extrusion rate. (b) Stepwise motion characteristics, indicating underlying stick-slip mechanism for drumbeat creation ($t < 8000$ s). (c) Oscillating motion characteristics due to up- and downward plug motion ($t > 8000$ s).

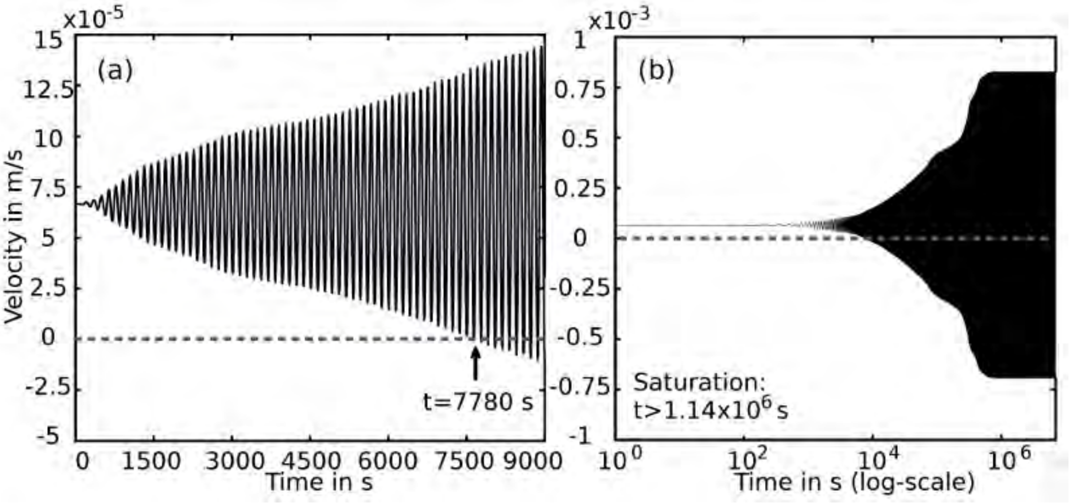

**Figure 5.4:** (a) Calculated velocity evolution during the first 8000 s (2.5 hours). (b) Extrusion velocity calculation for 15 months of MSH activity. Logarithmic scale.

We present six representative solutions for estimating the displacement behavior due to changes in parameter values and initial conditions (Figure 5.5). The dependence of the system on variations in the remaining parameters such as compressibility, fluid viscosity, etc. yield similar results and are not discussed in detail.

The behavior of the system is primarily controlled by the initial velocity $u_0$ and the plug mass $m_0$. Changes in the mass change rate $\kappa$ of the solidifying plug are shown in Figure 5.5(a). Increasing $\kappa$ leads to differences in the slip distance and therefore the long-term extrusion rate decreases. Characteristics due to the change in the coefficient of friction $\mu$ differ just slightly (Figure 5.5(b)). For changes in the fault gouge permeability $k$ the period between slip events remain constant, but here, too, the slip distance decreases for more permeable gouge material. Figure 5.5(d) yields most insights on system control: Both, the amplitude and frequency of plug displacement depend strongly on the initial plug mass $m_0$. The more massive the plug is the bigger are the stick-slip steps. The slope of all solution graphs remains the same. The change in the initial plug velocity $u_0$ is presented in Figure 5.5(e). The variation results in large amplitude differences for different $u_0$ while the period between each slip event remains constant. Finally, displacement due to the change in the initial magma volume $V_0$ (Figure 5.5(f)) controls the slope of the displacement function. The more magma is assumed, the steeper the function, i.e. the faster the plug is extruded.

Although our results mimic well the observations at MSH and are consistent with results obtained for the original SPASM model developed by Iverson et al. (2006), both models have to be used with care. Since the system of equations has a natural tendency to oscillate, certain parameter combinations can damp, force or break down this behavior. Possible extensions and limits of the conceptual and mathematical formulation are discussed in the next section.

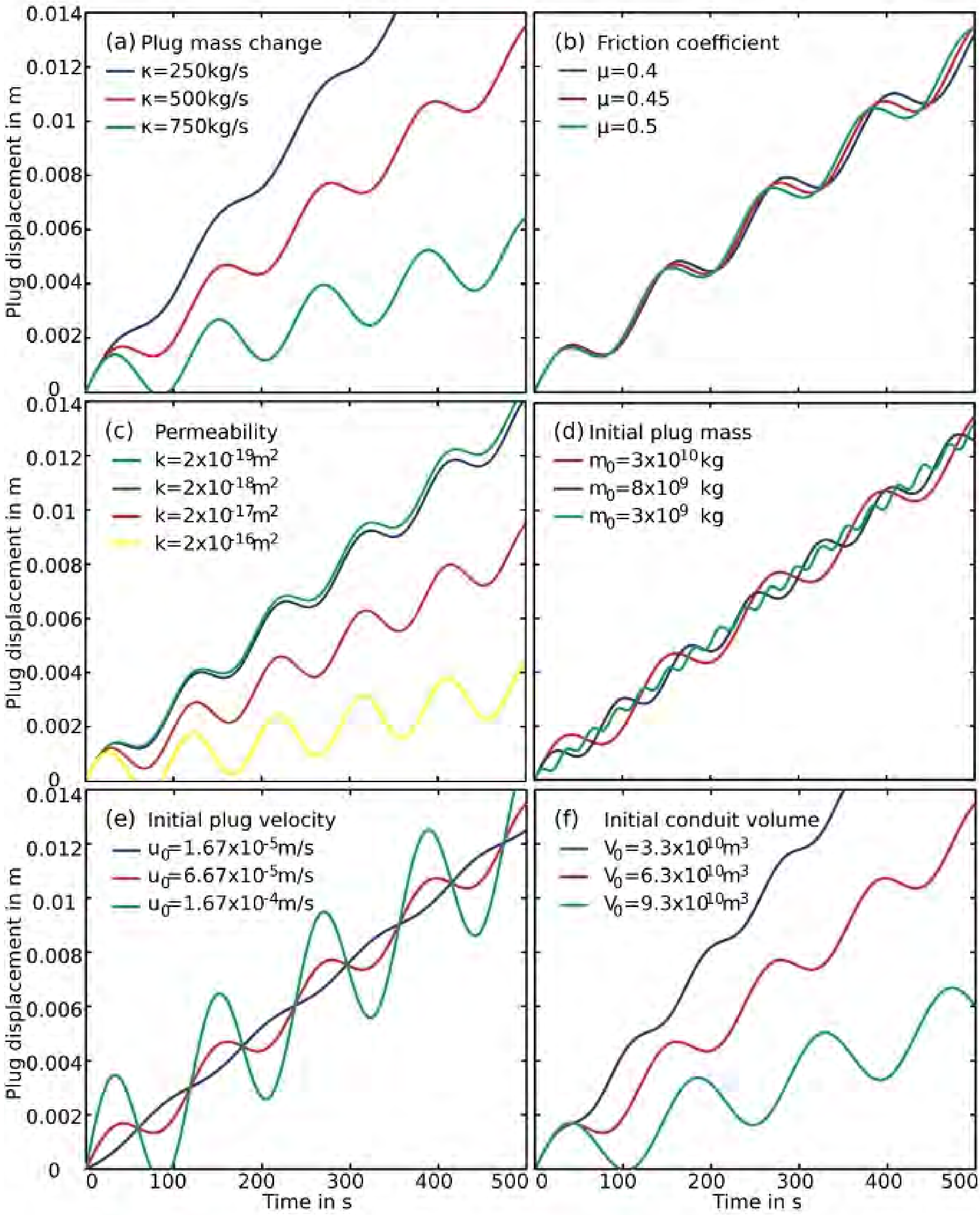

**Figure 5.5:** Plug displacement depending on parameter variations. Characteristics due to (a) plug mass change rate $\kappa$, (b) the change in the coefficient of friction $\mu$ and (c) in the fault gouge permeability $k$. For increases in $\kappa$ and $k$ the period between slip events remains the same, but the slip distance decreases. Changes in $\mu$ do not yield significant result differences. (d) The amplitude and frequency of plug displacement depends strongly on the initial plug mass $m_0$ and (e) the change in the initial velocity $u_0$ effects large amplitude differences. (f) Plug displacement depending on the change in the initial magma volume $V_0$ results in solutions similar to 5.5(a).

## 5.4 Discussion: Extensions and limitations

As inferred by Moran et al. (2008), the period of occurring earthquakes during the 2004-2006 eruption was nearly constant between $30 - 300$ s, but shifted slowly over time. Also, in the beginning of the renewed MSH activity the lava dome extrusion rate accompanied by the outflow of magmatic gases showed intermittent nonlinear characteristics (Dzurisin et al., 2005). Our results exhibit just constant displacement periods and linear extrusion rates. As variations in certain parameter values provide the possibility to change the slope and period of displacement solutions, the introduction of non-constant characteristics is an obvious improvement to force certain behavior.

The initial plug mass $m_0$ strongly influenced the displacement period and step length, but the mass change rate $\kappa$ was held constant, so a complete reformulation of the SPASM model would be required when forcing variations in $m_0$ over time. We do not reformulate the whole system, but determine how the system of equations reacts applying different assumptions on the underlying behavior.

These examples show that the SPASM model is very sensitive to changes and can even loose its periodic characteristics. The reason for these results when applying new assumptions on the system of equations becomes apparent after differentiation of Equation (5.3) with time and combination with (5.4)

$$\frac{d^2u}{dt^2} = \frac{1}{m_0 + \kappa t}\left(-\kappa g - 2\kappa\frac{du}{dt} - \frac{A}{V_m\left(\alpha_1 + \alpha_2\right)}\left(Au + \left(1 - \frac{\rho_m}{\rho_s}\right)B - Q\right) - \frac{dF}{dt}\right). \quad (5.14)$$

In our model with fluid degassing, we assumed a vapor-liquid-equilibrium for magma and exsolved gases for the closed system, i.e. when fluids do not escape along the solid plug towards the free surface. Another possibility to describe melt-magmatic gas-interactions is Henry's law for ideal gases (Huppert and Woods, 2002; Melnik and Sparks, 1999). It is commonly used for estimating concentrations of volatiles (especially water) dissolved in and exsolving from erupting melt due to pressure changes. For rhyolite magmas the mass fraction of exsolved volatiles $n$ is proportional to the square root of pressure and states $n = N - s\sqrt{p}$, where $s = 4.1 \times 10^{-6}\sqrt{\mathrm{Pa}}$ is the solubility of water and $N$ the initial volatile content in the melt. From this relationship, we can estimate the degassing rate required for the source term in Equation (5.10) from the assumed initial volatile content at MSH of approximately 12% (Pallister et al., 2008). The result is shown in Figures 5.6(a) and (b) together with the originally used vapor-liquid-equilibrium solution. We recognize that the time difference between displacement steps remains the same, but the application of Henry's law causes disturbances on the amplitude, i.e. the displacement length, and the slope of the function. Shortly after initialization the green line flattens and after approximately 1200 seconds the displacement amplitude decreases to recover and increase again. That means that fluctuations in extrusion rate can be achieved by changing the degassing assumptions.

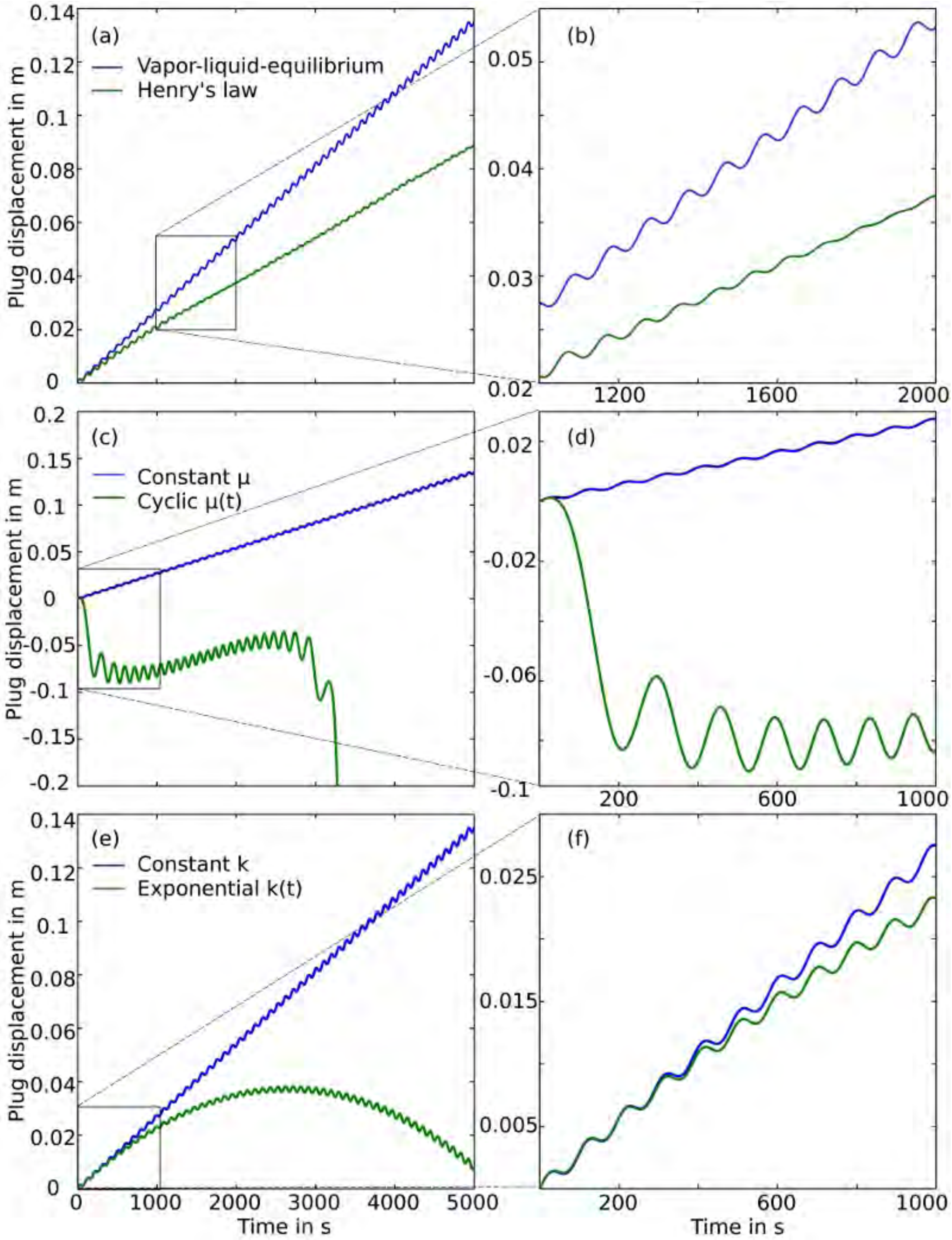

**Figure 5.6:** Plug displacement depending on different degassing rules and time-dependent parameter functions. (a) Vapor-liquid-equilibrium versus Henry's law assumption on the exsolution behavior with (b) detailed view on amplitude changes. (c) and (d) show arbitrary time-dependent (cyclic) coefficient of friction $\mu(t)$ with break down of the linear extrusion rate ($\mu$ constant), and (e) and (f) exhibit the effect of an exponentially decreasing gouge permeability function $k(t)$ compared with constant $k$.

Next, we investigate the displacement behavior due to the introduction of gouge material permeability $k(t)$ and friction coefficient $\mu(t)$ functions, neglecting their changes with position. The choice of replacing these two constant parameters as well as their time-dependent formulation is arbitrary. We apply a cyclic, i.e. sinusoidal, friction coefficient function, which might arise from changes in the friction angle when the plug is moving up- and downward. Figures 5.6(c) and (d) depict the strong effect on the amplitude and frequency of the function until the oscillating displacement breaks down and the plug "falls down" into the conduit. Choosing an exponentially decreasing gouge permeability function $k(t)$, e.g. resulting from erosion of the material and extrusion at the free surface, the step sizes remain almost the same, but the slope loses its linearity trend and decreases rapidly.

Equation (5.14) is a second order differential equation with the form of a damped, forced oscillator. This implies that the plug velocity $u$ has a natural tendency to oscillate about equilibrium with the period and damping controlled by the particular choice of parameters. The general form of damped, forced harmonic oscillators is mostly given by

$$\ddot{x} + 2\gamma\dot{x} + \omega^2 x = \varphi, \tag{5.15}$$

where $x$ is the oscillator, $\dot{x}$ and $\ddot{x}$ its time derivatives, $2\gamma$ denotes the damping constant, $\omega$ is the characteristic, natural, angular frequency (giving the frequency of the oscillation via $f = \omega/(2\pi)$), and $\varphi$ is an external force (Iverson, 2008, and references therein). This formulation shows that by applying arbitrary assumptions on e.g. permeability function as seen above, the model can be extended to mimic external factors controlling the system. But care must be taken, as the periodic behavior can break down: Oscillation of the harmonic, damped, forced system is ensured, if $\gamma^2 < \omega^2$ (under-damping). So parameter combinations, especially when dealing with parameter functions, must be chosen carefully as all parameters of the SPASM model can effect changes in the frequency and amplitude of the solution (as seen for 5.6(a)), force the system to follow an external function (compare with 5.6(e)) or even break it down (see 5.6(c)) for $\gamma^2 \geq \omega^2$, when over-damping and critically damping the systems.

## 5.5 Concluding remarks

We modified the original SPASM model by including the effects of fluids produced by the degassing magma body into the system. Using a Coulomb-type friction law taking into account effective stress concepts, we showed that a simple friction function is also able to simulate the dynamics of linear volcanic extrusion accompanied by shallow drumbeat earthquakes at MSH. Model results show a displacement profile with appropriate displacement differences (step lengths and time cycles) that match the earthquake period and observed average extrusion rate at MSH. Plug velocity saturates naturally from the underlying equations, leading to reasonable solutions and good comparisons with the measured average velocity values.

However, many assumptions and simplifications were necessary to keep the model simple, and many aspects of the observed MSH activity were ignored. One possible extension is the introduction of a more precise gouge matrix description with time dependent porosity as an additional parameter for the fluid flow process (Segall and Rice, 1995). Periodic responses due to compaction and dilatation of fluids inside fractured systems or along faults can also be simulated with the concepts of fluid flow in a ductile matrix such as porosity wave propagation (Connolly and Podladchikov, 1997). Both theories require a sound knowledge of the material matrix with respect to position and must be considered when calculating the fluid propagation path towards the surface, but are not necessary for our transient function examination. The model can be improved by inserting additional functions instead of constant parameters, but changes should be made with care in order to maintain the natural tendency of the system for forced, damped oscillation.

Finally, an important issue when applying and adopting the SPASM model to other volcanic settings is to clearly distinguish between the source of the seismic events, as nonlinear processes during the crystallization and decompaction of magma bodies also bear cyclic extrusion rates and eruptions accompanied by earthquakes (Barmin et al., 2002; Costa et al., 2007).

# Chapter 6

# Summary and Conclusion

The focus of this work is the numerical modeling and identification of fluid pressure driven phenomena and processes. The effects of overpressurized fluids in the lithosphere were considered for three different settings that occurred during the last five years. The aim of this thesis is to further our physical understanding of fluid pressure related geohazards and their interaction in the upper 20 km of the crust, covering statistical data analyses, conceptual model development and mathematical modeling. The cases and settings considered involve diverse range of globally observed phenomena, so various mathematical and conceptual developments were employed.

The models developed for periodic volcanic extrusion processes for the LUSI mud volcano in Indonesia and for the Mount St. Helens in Washington cover dynamical fluid escape aspects on the one hand and concomitant phenomena like earthquake generation due to mechanistic effects on the other.

For LUSI, representative of mud extrusion and eruption problems, the mathematical formulation and its results are a cornerstone for mud volcano and geyser modeling, as this study is the first being able to predict the eruption decay. We showed the wide application possibilities of the modular concept and its advantage of being capable for extensions and improvements by providing results for one conduit geometry and two mud reservoir estimates, and by presenting the dependence of discharge rate and extruded mud volume solutions on initial conditions and parameter choices. The model was published as part of the Marine and Petroleum Geology Special Issue “Mud Volcanism: Processes and Implications”, where Adriano Mazzini says within the editorial article (Mazzini, 2009):

> *Despite the numerous studies, the mechanisms controlling mud volcano eruptions are still debated. Among the most advanced and innovative approaches are the numerical modeling simulations. In this special issue are included some examples of revolutionary techniques that help to test hypotheses from the bosom of the Earth exploring the cyclicity and the parameters controlling the blasts (Gisler, 2009; Zoporowski and Miller, 2009).*

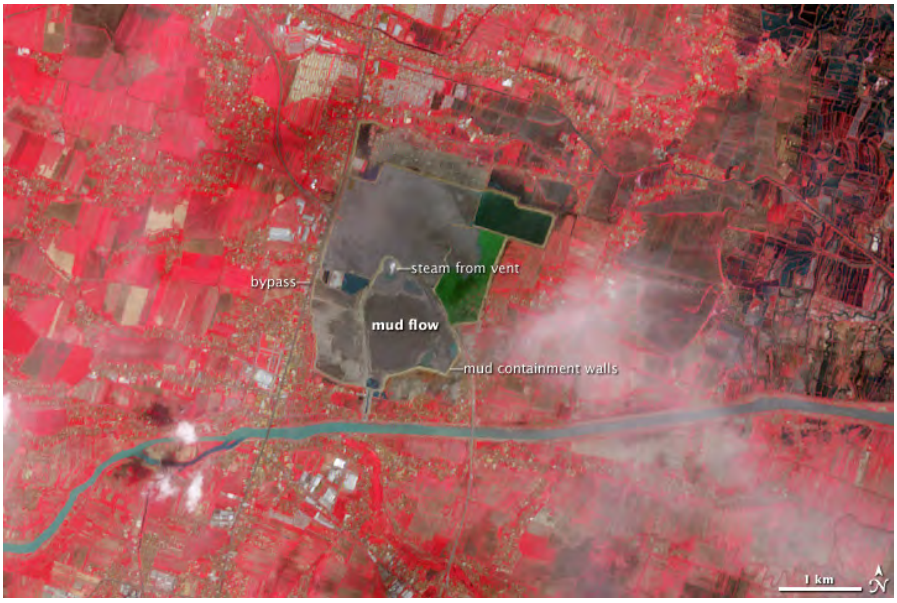

**Figure 6.1:** LUSI, the Lumpur Sidoarjo mud flow in East Java, Indonesia. Top view on mud flooded area. The Advanced Spaceborne Thermal Emission and Reflection Radiometer on NASA's Terra satellite acquired these image on November 11, 2008. In these false-color images, red indicates vegetation, pale blue and green indicate bare ground and/or fallow fields, and black indicates water. Figure source: Allen (2008).

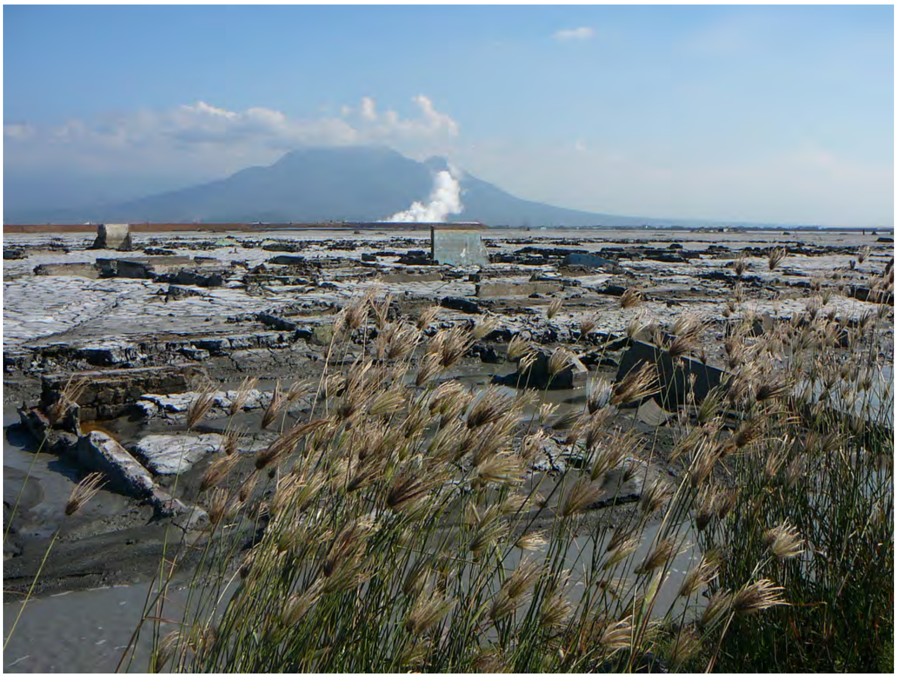

**Figure 6.2:** Flooded landscape in Sidoarjo, Indonesia, including streets, buildings and agricultural areas. More than 40 thousand inhabitants are still affected. Steaming LUSI and the stratovolcano Mount Penanggungan can be seen in the background. Picture taken from Stein (2008).

However, the examination of mud ascent through an open mud volcano conduit is just a first step forward. The social and environmental impact of LUSI was extreme as the mud, covering an area of seven square kilometers with 20 meters thickness, wiped out 12 villages and displaced more than 40,000 inhabitants of Sidoarjo (Berry, 2010). All attempts to stop the flow have failed (Glionna, 2010). Combination of the approach presented with initial triggering and conduit opening processes is desirable for enhancing forecasting of mud volcano eruptions. Introducing fully compressible flow, the use of a non-constant viscosity, different conduit shapes and temperature into the problem are reasonable suggestions to develop reliable techniques for the control of mud extrusion.

Modeling the volcanic earthquakes at Mount St. Helens, Washington, provided an opportunity to link together dynamical and mechanistic effects of overpressurized fluids. The underlying SPASM model has provided an important first approach to explain the origin of periodic seismic responses at volcanic settings, but lacks justifications due to the use of empirical functions describing the quantitative behavior (Iverson et al., 2006). We showed, using a Coulomb-type friction law taking into account effective stress concepts, a simple friction function to be able to simulate the dynamics of linear volcanic extrusion accompanied by shallow drumbeat earthquakes at MSH, and furthermore, the effects of fluids produced by the degassing magma body were introduced into the system. Model results match the earthquake period and observed mean extrusion rate at MSH and plug velocity saturates naturally from the underlying equations, leading to reasonable solutions and good comparisons with the measured mean extrusion velocity values.

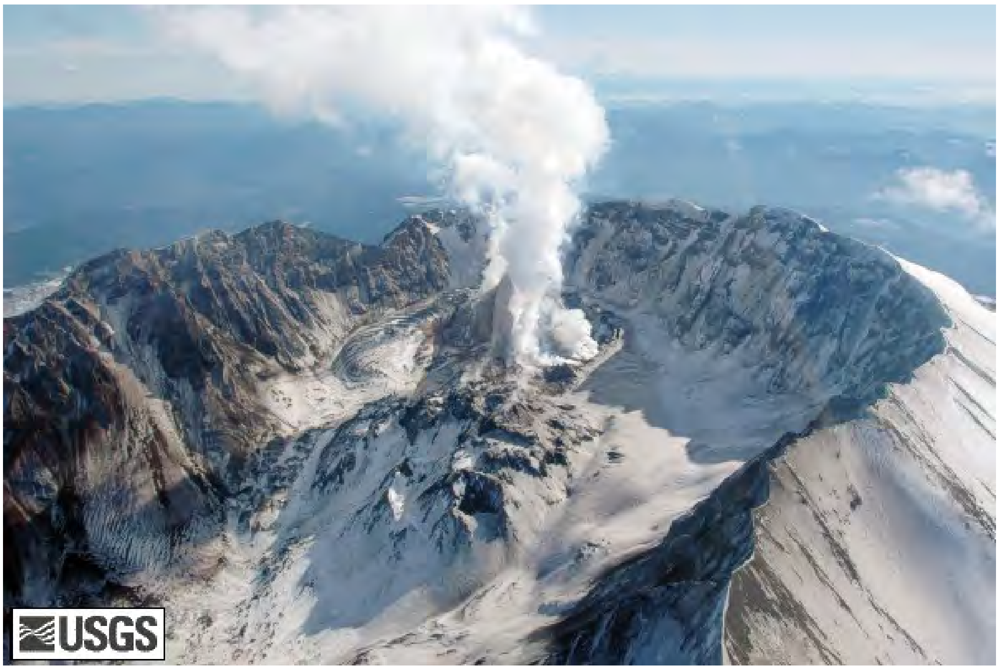

**Figure 6.3:** Aerial view from north-west of a steaming Mount St. Helens with extruded lava dome. Picture source: Doukas and Griswold (2005).

Recent publications dealing with periodic extrusion or tilt confirm that our idea is a reasonable starting point to extend the SPASM model and worth, while combining with other models. For example, Lensky et al. (2008) describe similar effects at Soufrière Hills Volcano, Montserrat, taking the vesicularity and gas exsolution of magma as the driving system for pressurization and depressurization instead of plug movement. That shows that taking into account a degassing magma body is crucial for modeling volcanic processes. It is desirable to join the complex pressurization process provided by Lensky et al. (2008) with the extended SPASM model proposed here, and trying to reproduce the observations at MSH given by Iverson et al. (2006).

Further simulations are necessary for the transferability of our model to other volcanoes, with adjusted parameter ranges or parameter functions. The mathematical formulation and its results need to be confirmed by controlled laboratory analogue simulations (J. Phillips, 2008, personal communication), and an application on the oscillatory plug behavior at Santiaguito volcano, Guatemala, is striven (L. Scharff, 2009, personal communication). But changes should be made with care, when the natural tendency of the system for forced, damped oscillation should persist.

Future volcano modeling studies should include the introduction of the material matrix with respect to position, which has to be considered when calculating the accurate fluid propagation path towards the surface. A more precise gouge matrix description for the fluid flow process (Segall and Rice, 1995), or the simulation of periodic responses due to compaction and dilatation of fluids inside fractured systems or along faults with the concepts of porosity wave propagation (Connolly and Podladchikov, 1997).

Findings presented in chapter 4 showed additional evidence for fluid-induced earthquake and aftershock generation in L'Aquila, Italy, 2009. The results of our analyses on the spatiotemporal distribution of aftershocks and the expected Coulomb stress change and dilatation due to different fault scenarios does not support the theory that the L'Aquila earthquake was purely driven by static stress transfer. There are two reasons for these conclusions:

1. The positive Coulomb stress changes due to the analyzed fault scenarios do not significantly correlate with aftershock hypocenter locations, and a significant number of events occur as well in negative $\Delta CFS$ regions.

2. Earthquakes following the April 6th main shock show a very strong correlation with regions between positive and negative dilatation, indicating some sort of diffusion dominated process.

The evolution of aftershock locations indicate that aftershocks behave similar to the 1997 Colfiorito earthquake sequence, lying in the same geological setting, known for being driven by trapped high pressure fluids (Miller et al., 2004). Consequently, we suggest the L'Aquila aftershock sequence to be driven by fluid flow associated with volumetric compression and by the diffusion of high pressure fluids from a deep source, initialized by fracturing due to the main shock.

These findings were used by Terakawa et al. (2010) as supporting evidence for a new analysis technique termed Focal Mechanism Tomography (FMT) for identifying trapped pressurized fluids in aftershock sequences. Contemplating figures presented in this manuscript, Terakawa et al. (2010) state:

> *Aside from narrow regions to the southeast of the fault strike, the change in Coulomb failure stress ($\Delta CFS$) has little correlation with aftershock locations at individual depths (Fig. DR5), or in profile (Fig. 4B). The locations of early aftershocks appear to be related to regions of volumetric compression due to the main shock (Figs. 4B and DR5), indicating a mechanism where compression of high-fluid-pressure reservoirs initiates fluid flow toward dilatant zones (Nur and Booker, 1972). This increases the fluid pressure down-gradient and generates poro-elastic shear stresses in response to that flow (Nur and Booker, 1972; Bosl and Nur, 2002; Rozhko et al., 2007).*

The basis for FMT is the assumption that earthquakes occur in the direction of the resolved shear traction acting on pre-existing faults (McKenzie, 1969), which also applies in stress inversion of fault slip data (Gephart and Forsyth, 1984; Michael, 1984, 1987). Based on the moment tensor solutions of the main-shock and extensional tectonics in the central Apennines (Walters et al., 2009), a series of inversions

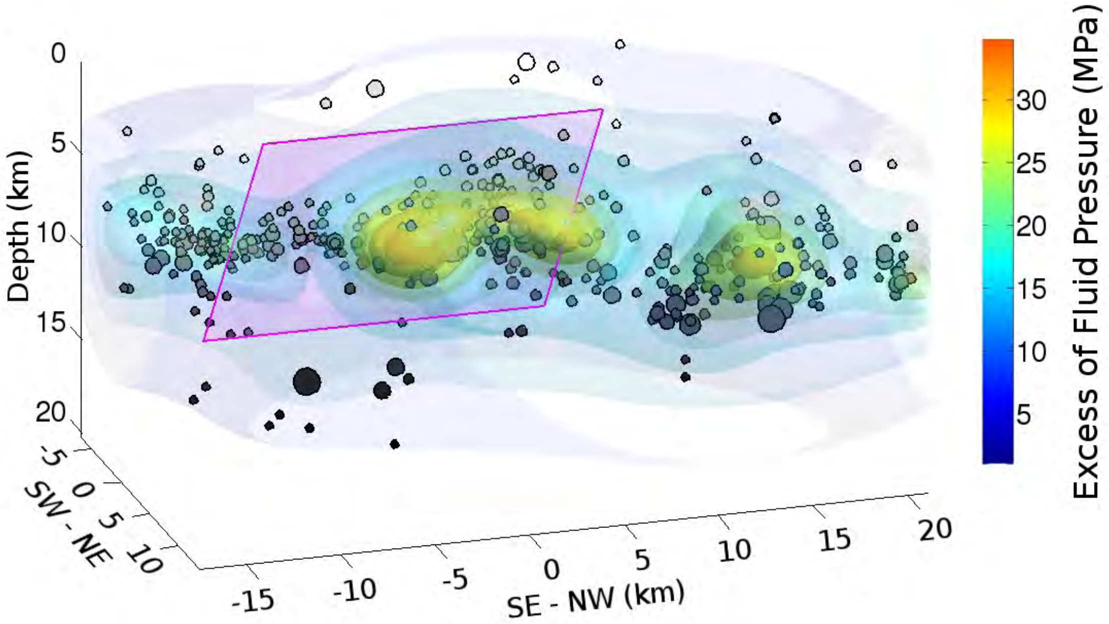

**Figure 6.4:** Three-dimensional image of the excess fluid pressure field with the hypocenters of foreshocks and aftershocks (Chiarabba et al., 2009) and projected fault of the main shock (Cirella et al., 2009). View is from the northeast toward southwest. Figure taken from Terakawa et al. (2010, Fig. 3B).

were performed to maximize the sum of the closeness of the observed and theoretical moment tensors for the given stress state, and Terakawa et al. (2010) indeed identified three large-scale pockets of high fluid pressure at depths of 7-10 km, and show a very strong correlation between these high fluid pressure regions and both foreshock and aftershock hypocenters. The mapped 3D fluid pressure field inferred from the FMT (Fig. 6.4) provides an important boundary condition for modeling fluid flow and stress evolution for a mechanistic assessment of the continuing seismic hazard in the region.

The cases considered in this thesis have already contributed to the physical understanding of fluid pressure driven aftershock scenarios and the dynamical behavior and interaction of overpressurized fluids in the upper Earth's crust. We want the models and techniques to be developed further and adjusted and applied to similar volcanoes, mud flows and earthquakes around the world. The findings have been integrated into the geoscientific knowledge pool and shall be employed by open-minded researchers. We hope that our conclusions will be regarded in future studies for enhancing forecasting techniques and hazard analysis, with the benefit of minimizing natural disasters.

# Appendix A

## A.1 Runge-Kutta method

Presented solutions of ordinary differential equations for continuous time dynamics are obtained by numerical integration. Many different methods exist to solve accurately various types of ordinary differential equations. Most used are the Runge-Kutta methods, discretizing the differential system to produce a difference equation with dynamics corresponding closely to the dynamics of the differential equation (Arndt, 2003). The examined initial-value problems are characterized by specifying initial conditions for the solution at the start of the trajectory (in contrast to other problems where conditions are specified at the start and at the end of the trajectory, called boundary-value problem). As problems described by ordinary differential equations can always be reduced to a system of first-order ordinary differential equations by introducing the derivatives of the original variables as new variables, the general non-autonomous initial value problem reads

$$\begin{aligned} y' &= f(x, y), \\ y_0 &= y(x_0), \quad x_0 \leq x, \end{aligned} \tag{A.1}$$

where $y' = \frac{dy}{dx}$ ($x$ often representing time). This can be a single equation or a coupled system of equations $(x, y) \in (\mathbb{R}, \mathbb{R}^m)$, $m \geq 1$. Sufficient conditions for the existence of an unique, continuous, differentiable function $y(x)$ as a solution to equation (A.1) is that $f(x, y)$ is defined, continuous and satisfies the Lipschitz condition

$$\|f(x, y) - f(x, \tilde{y})\| \leq L\|y - \tilde{y}\|, \quad \forall (x, y), (x, \tilde{y}) \in (\mathbb{R}, \mathbb{R}^m), \tag{A.2}$$

in $y$ in $[x_0, x_{\text{end}}] \times (-\infty, \infty)^m$ with existing Lipschitz constant $L$. Runge-Kutta methods compute approximations $u_j$ to $y_j = y(x_j)$, with initial values $u_0 = y_0$, where $x_{j+1} = x_j + h$, $j = 0, 1, 2, \ldots$, using the Taylor series expansion

$$y(x + h) = y(x) + hy'(x) + \frac{1}{2}h^2 y''(x) + \cdots + \frac{1}{p!}h^p y^{(p)}(x) + \mathcal{O}(h^{p+1}), \tag{A.3}$$

with $h$ the non-negative step length of the method. For an explicit $s$-stage Runge-Kutta method, $s \in \mathbb{N}$, it is

$$u_{j+1} = u_j + h \sum_{i=1}^{s} b_i v_i(x_j, u_j, h), \tag{A.4}$$

with

$$v_s(x_j, u_j, h) = f\left( x_j + hc_s\,,\; u_j + h \sum_{i=1}^{s-1} a_{si} v_i(x_j, u_j, h) \right). \tag{A.5}$$

The schemes are one-step methods giving $u_{j+1}$ in terms of $u_j$. They have order $p$, i.e. $p$ is the largest integer with

$$y(x+h) - y(x) - h \sum_{j=1}^{s} a_{ij} v_j = \mathcal{O}(h^{p+1}). \tag{A.6}$$

The goal is to find values for $a_{ij}$, $b_j$ and $c_i$ with $1 \leq (i,j) \leq p$ so that equation (A.4) matches the first $p+1$ terms in equation (A.3), which is achieved by expanding equation (A.4) in Taylor series about $(x_j, u_j)$ under the assumption that $u_j = y_j$. With that all previous values are exact and the comparison with equation (A.3) makes equation of coefficients possible. A general result is that an explicit $s$-stage method cannot have order greater than $s$, being an upper bound that is realized only for $s \leq 4$. This is the reason why fourth-order methods are so common and popular, because after that, one has to add two more stages to the method to obtain any increase in the order (Cartwright and Piro, 1992). For example, the classical 4th order Runge-Kutta method has the coefficients

$$\begin{array}{c|cccc} c_1 & & & & \\ c_2 & a_{21} & & & \\ c_3 & a_{31} & a_{32} & & \\ c_4 & a_{41} & a_{42} & a_{43} & \\ \hline & b_1 & b_2 & b_3 & b_4 \end{array} \qquad \begin{array}{c|cccc} 0 & & & & \\ \frac{1}{2} & \frac{1}{2} & & & \\ \frac{1}{2} & 0 & \frac{1}{2} & & \\ 1 & 0 & 0 & 1 & \\ \hline & \frac{1}{6} & \frac{2}{6} & \frac{2}{6} & \frac{1}{6} \end{array} \tag{A.7}$$

Requirements for a successful numerical algorithm is its convergence and consistency. A numerical method is called convergent, if the global error $\varepsilon_h(x) = y(x) - u_h(x)$ fulfills

$$\|\varepsilon_h\|_h = \max_{x_0 \leq x \leq x_{end}} |y(x) - u_h(x)| \xrightarrow{h \to 0} 0, \tag{A.8}$$

and it is called consistent, if $|u_{h,0} - y_0| \xrightarrow{h \to 0} 0$ and the local error $r(x,y,h) = \frac{y(x+h)-y(x)}{h} - \sum_{j=1}^{s} b_j v_j(x, y(x), h)$ fulfills

$$\sup_{x_0 \leq x \leq x_{end}-h} |r(x,y,h)| \xrightarrow{h \to 0} 0. \tag{A.9}$$

The necessary and sufficient condition for Runge-Kutta methods to be consistent is

$$\sum_{j=1}^{s} b_j = 1 \tag{A.10}$$

which is automatically satisfied when the method has order one or higher. Furthermore it is known that consistency is necessary and sufficient for convergence of Runge-Kutta methods, so all Runge-Kutta methods are convergent (Henrici, 1962).

In order to produce good results, numerical methods rely on error estimates to exercise control of the step length. This step control to maintain accuracy requirements is the use of a Runge-Kutta method that has been specially developed to provide an estimate of the principal local discretization error at each step. This may be done by embedding a $s$-stage, $p$th-order method within a $s+1$-stage, $p+1$-order method. Dormand and Prince (1980) derived an algorithm using this embedding estimate formulae of order 4 and 5 with automatic error estimation which have a minimum principal truncation (discretization) term and have an extended region of absolute stability

$$\begin{array}{c|ccccccc l}
0 & & & & & & & & \\
\frac{1}{5} & \frac{1}{5} & & & & & & & \\
\frac{3}{10} & \frac{3}{40} & \frac{9}{40} & & & & & & \\
\frac{4}{5} & \frac{44}{45} & -\frac{56}{15} & \frac{32}{9} & & & & & \\
\frac{8}{9} & \frac{19372}{6561} & -\frac{25360}{2187} & \frac{64448}{6561} & -\frac{212}{729} & & & & \\
1 & \frac{9017}{3168} & -\frac{355}{33} & \frac{46732}{5247} & \frac{49}{176} & -\frac{5103}{18656} & & & \\
1 & \frac{35}{384} & 0 & \frac{500}{1113} & \frac{125}{192} & -\frac{2187}{6784} & \frac{11}{84} & & \\
\hline
b_i & \frac{35}{384} & 0 & \frac{500}{1113} & \frac{125}{192} & -\frac{2187}{6784} & \frac{11}{84} & 0 & (\text{order } p=5) \\
b_i^* & \frac{5179}{57600} & 0 & \frac{7571}{16695} & \frac{393}{640} & -\frac{92097}{339200} & \frac{187}{2100} & \frac{1}{40} & (\text{order } p^*=4)
\end{array} \tag{A.11}$$

where using coefficients $b_i$ gives a 5th-order method and using $b_i^*$ gives a method of order 4. Furthermore, it was extended to a continuous Runge-Kutta method by using inexpensive interpolants for the Dormand-Prince pair (Dormand and Prince, 1986), given by

$$\begin{aligned}
b_1(\theta) &= b_1(1)\cdot\theta^2(3-2\theta)+\theta(\theta-1)^2-5\cdot\frac{2558722523-31403016\cdot\theta}{11282082432}\cdot\theta^2(\theta-1)^2 \\
b_2(\theta) &= 0 \\
b_3(\theta) &= b_3(1)\cdot\theta^2(3-2\theta)+100\cdot\frac{882725551-15701508\cdot\theta}{32700410799}\cdot\theta^2(\theta-1)^2 \\
b_4(\theta) &= b_4(1)\cdot\theta^2(3-2\theta)-25\cdot\frac{443332067-31403016\cdot\theta}{1880347072}\cdot\theta^2(\theta-1)^2 \\
b_5(\theta) &= b_5(1)\cdot\theta^2(3-2\theta)+32805\cdot\frac{23143187-3489224\cdot\theta}{199316789632}\cdot\theta^2(\theta-1)^2 \\
b_6(\theta) &= b_6(1)\cdot\theta^2(3-2\theta)-55\cdot\frac{29972135-7076736\cdot\theta}{822651844}\cdot\theta^2(\theta-1)^2 \\
b_7(\theta) &= \theta^2(\theta-1)+10\cdot\frac{7414447-829305\cdot\theta}{29380423}\cdot\theta^2(\theta-1)^2.
\end{aligned} \tag{A.12}$$

Generally, a continuous Runge-Kutta method is given, when the approximations $u_h(x_j)$ to $y(x_j)$ are interpolated via

$$u_h(x_j+\theta h) = u_h(x_j) + h\sum_{i=1}^{s} b_i(\theta)v_i(x_j,u_h(x_j),h), \quad 0<\theta\le 1, \tag{A.13}$$

with $b_i(1) = b_i$, in order to obtain a continuous approximation $u_h(x)$ to $y(x)$.

The Dormand-Prince method forms the base for the MATLAB `ode45` Runge-Kutta-solver, which computes high quality solution values at four points spaced evenly within the span of each natural step. The MATLAB source code is not under public license. `[T,Y] = ode45(odefun,tspan,y0)` with `tspan = [t0 tf]` integrates the system of differential equations (A.1) from time `t0` to `tf` with initial conditions `y0`. It is a one-step solver for non-stiff problems, i.e. in computing `y(tn)`, it needs only the solution at the immediately preceding time point `y(tn − 1)`. Function `f = odefun(t,y)`, for a scalar `t` and a column vector `y`, returns a column vector `f` corresponding to the right hand side of equation (A.1). Each row in the solution array `Y` corresponds to a time returned in column vector `T`. By default, the steps are chosen by the solver, using a scalar relative error tolerance $\texttt{RelTol} = 10^{-3}$ and a vector of absolute error tolerances for all components $\texttt{AbsTol} = 10^{-6}$. `ode45` accepts modifications to default settings and further parameter options.

We used this effective tool to obtain continuous solutions to our dynamical models described by ordinary differential equations in chapter 3 and chapter 5.

## A.2 Coulomb failure stress analysis

Coulomb 3.1 (Lin and Stein, 2004; Toda et al., 2005) is a MATLAB add-on tool to investigate Coulomb stress changes on mapped faults and earthquake nodal planes. Analysis and visualization of strains and stresses caused by fault slip and of problems like how an earthquake promotes or inhibits failure on nearby faults are provided.

Calculations are made in the $(x, y, z)$ Cartesian coordinate system in an elastic half-space with uniform isotropic elastic properties following Okada (1992). Coulomb calculations require properly formated input files, which can be automatically created by inserting parameters into a graphical user interface. In these input files, fault properties like position and depth, displacement, direction, dip and angle must be specified. The faults are defined with right-hand rule for start points, positive dip, right-lateral/reverse or rake/net slip (right-lateral is positive, and reverse slip is positive) according to the Aki and Richards (2002) sign convention. The total seismic moment of the earthquake source fault is calculated using the fault area, slip, Young's modulus and Poisson's ratio. To remove unrealistic stress concentrations at the edges of a fault, the slip can be tapered by interlaced faults. This procedure can be also used for creating faults with known variable slip or non-uniform slip distributions.

Source faults have slip and impart Coulomb stress on specified or optimally-oriented receiver planes with assumed slip directions given by the regional stress, following the Coulomb failure hypothesis

$$\Delta CFS = \Delta\tau + \mu\Delta\sigma_n. \tag{A.14}$$

Failure is promoted when the Coulomb stress increases. $\Delta CFS$ is the change in failure stress on the receiver fault caused by slip on the source fault(s), $\Delta\tau$ is the change in shear stress (positive in the direction of receiver fault slip), $\Delta\sigma_n$ is change in normal stress (positive when the receiver fault is unclamped), and $\mu$ is effective fault friction coefficient on the receiver fault. The regional stress tensor (positive in compression) and friction coefficient may be adjusted as additional input parameters.

Graphical and numerical output parameters provided by Coulomb 3.1 include displacement, dilatational strain $\varepsilon_{xx} + \varepsilon_{yy} + \varepsilon_{zz}$ and Coulomb stress change $\Delta CFS$ in both, map view and cross-section view. In addition, the graphical output may be overlaid with seismic catalog information. The format of the dataset must match one of the supported catalog formats (U.S., Japan, etc.), and may be filtered for time, location (longitude/latitude), depth and earthquake magnitude.

Figures included in chapter 4, showing the 2009 L'Aquila main shock fault and aftershock locations in 3D and map views and cross-sections of $\Delta CFS$ and dilatational strain overlaid with seismic data, were created with the Coulomb 3.1 software. In the following, input file examples for regional static stress change and dilatational strain calculations are given. Not all files used in chapter 4 are provided, but three files are shown, exemplifying a single source fault with uniform slip, a single fault with non-uniform slip and a multi-fault system:

**Listing A.1:** Coulomb 3.1 input file for a single source fault with uniform slip distribution.

```
header line 1
header line 2

#reg1=  0  #reg2=  0  #fixed=   1  sym=  1
 PR1=       0.250     PR2=       0.250   DEPTH=       7.500
  E1=     8.000e+05    E2=     8.000e+05
XSYM=       .000     YSYM=       .000
FRIC=          0.400
S1DR=         19.000 S1DP=         -0.010 S1IN=        100.000 S1GD=          0.000
S2DR=         89.990 S2DP=         89.990 S2IN=         30.000 S2GD=          0.000
S3DR=        109.000 S3DP=         -0.010 S3IN=          0.000 S3GD=          0.000

  #   X-start    Y-start     X-fin      Y-fin   Kode  rt.lat    reverse   dip angle     top      bot
xxx xxxxxxxxxx xxxxxxxxxx xxxxxxxxxx xxxxxxxxxx xxx xxxxxxxxxx xxxxxxxxxx xxxxxxxxxx xxxxxxxxxx xxxxxxxxxx
  1     0.9330     5.2925     9.7093    -2.8915 100     0.1277    -0.6007    54.0000     3.0019    11.9981
       Fault 1


     Grid Parameters
  1  ----------------------------  Start-x =      -64.1494702
  2  ----------------------------  Start-y =      -83.1404175
  3  --------------------------   Finish-x =       50.9906782
  4  --------------------------   Finish-y =       72.5326495
  5  ------------------------  x-increment =        0.9841038
  6  ------------------------  y-increment =        0.9979043

      Size Parameters
  1  --------------------------  Plot size =        2.0000000
  2  --------------  Shade/Color increment =        1.0000000
  3  ------  Exaggeration for disp.& dist. =    10000.0000000

      Cross section default
  1  ----------------------------  Start-x =       13.5446377
  2  ----------------------------  Start-y =       13.8963962
  3  --------------------------   Finish-x =       42.4726424
  4  --------------------------   Finish-y =       42.7319841
  5  ------------------  Distant-increment =        1.0000000
  6  ----------------------------  Z-depth =      -30.0000000
  7  ------------------------  Z-increment =        1.0000000

      Map info
  1  ---------------------------- min. lon =       12.6000004
  2  ---------------------------- max. lon =       14.0000000
  3  ---------------------------- zero lon =       13.3800001
  4  ---------------------------- min. lat =       41.5999985
  5  ---------------------------- max. lat =       43.0000000
  6  ---------------------------- zero lat =       42.3476982
```

**Listing A.2:** Coulomb 3.1 input file for a single source fault with non-uniform slip.

```
header line 1
header line 2

#reg1=  0  #reg2=  0  #fixed=  5  sym=  1
 PR1=       0.250     PR2=       0.250    DEPTH=        6.000
  E1=      8.000e+05   E2=      8.000e+05
XSYM=       .000     YSYM=       .000
FRIC=          0.400
S1DR=         19.000 S1DP=         -0.010 S1IN=        100.000 S1GD=          0.000
S2DR=         89.990 S2DP=         89.990 S2IN=         30.000 S2GD=          0.000
S3DR=        109.000 S3DP=         -0.010 S3IN=          0.000 S3GD=          0.000

  #   X-start    Y-start     X-fin      Y-fin   Kode  rt.lat    reverse   dip angle     top      bot
xxx xxxxxxxxxx xxxxxxxxxx xxxxxxxxxx xxxxxxxxxx xxx xxxxxxxxxx xxxxxxxxxx xxxxxxxxxx xxxxxxxxxx xxxxxxxxxx
  1     0.1822     4.5640    10.7888    -6.0426 100     0.0225    -0.2730    55.0000     2.3958     9.6042
       Fault 1
  1     1.0400     3.3005     9.5253    -5.1848 100     0.0225    -0.2522    55.0000     2.8054     9.1946
       Fault 1
  1     1.8979     2.0371     8.2619    -4.3269 100     0.0225    -0.2522    55.0000     3.2149     8.7851
       Fault 1
  1     2.7558     0.7736     6.9984    -3.4690 100     0.0225    -0.2522    55.0000     3.6245     8.3755
       Fault 1
  1     3.6137    -0.4899     5.7349    -2.6111 100     0.0225    -0.2522    55.0000     4.0341     7.9659
       Fault 1


    Grid Parameters
  1  ----------------------------  Start-x =     -64.1494675
  2  ----------------------------  Start-y =     -83.1404190
  3  --------------------------   Finish-x =      50.9906769
  4  --------------------------   Finish-y =      72.5326462
  5  ------------------------  x-increment =       0.9841038
  6  ------------------------  y-increment =       0.9979043

     Size Parameters
  1  --------------------------  Plot size =       2.0000000
  2  --------------  Shade/Color increment =       1.0000000
  3  ------  Exaggeration for disp.& dist. =   10000.0000000

     Cross section default
  1  ----------------------------  Start-x =      13.5446377
  2  ----------------------------  Start-y =      13.8963962
  3  --------------------------   Finish-x =      42.4726424
  4  --------------------------   Finish-y =      42.7319841
  5  ------------------  Distant-increment =       1.0000000
  6  ----------------------------  Z-depth =     -30.0000000
  7  ------------------------  Z-increment =       1.0000000

     Map info
  1  ---------------------------- min. lon =      12.6000004
  2  ---------------------------- max. lon =      14.0000000
  3  ---------------------------- zero lon =      13.3800001
  4  ---------------------------- min. lat =      41.5999985
  5  ---------------------------- max. lat =      43.0000000
  6  ---------------------------- zero lat =      42.3476982
```

**Listing A.3:** Coulomb 3.1 input file for a multi-fault system with uniform slip distribution.

```
header line 1
header line 2

#reg1=  0  #reg2=  0  #fixed=  20  sym=  1
 PR1=       0.250     PR2=       0.250   DEPTH=       9.640
  E1=      8.000e+05   E2=      8.000e+05
XSYM=       .000     YSYM=       .000
FRIC=          0.400
S1DR=         19.000 S1DP=         -0.010 S1IN=        100.000 S1GD=          0.000
S2DR=         89.990 S2DP=         89.990 S2IN=         30.000 S2GD=          0.000
S3DR=        109.000 S3DP=         -0.010 S3IN=          0.000 S3GD=          0.000

  #   X-start    Y-start     X-fin      Y-fin   Kode  rt.lat    reverse   dip angle     top      bot
xxx xxxxxxxxxx xxxxxxxxxx xxxxxxxxxx xxxxxxxxxx xxx xxxxxxxxxx xxxxxxxxxx xxxxxxxxxx xxxxxxxxxx xxxxxxxxxx
  1    -0.3156    -2.0908    -0.1975    -1.4211 100    -0.0459    -0.0322    45.0000    11.0775    11.9825
       Fault 1
  1    -0.2845    -1.0711    -0.1924    -0.5491 100    -0.0680    -0.0476    45.0000     9.8076    10.5924
       Fault 2
  1    -4.7445     9.4111    10.4164    -1.6040 100     0.0485    -0.3948    35.0000     6.0816    12.8384
       Fault 3
  1    -2.7085     3.0706    -2.6475     2.3733 100    -0.0181    -0.0675    65.0000    -0.4149     0.5549
       Fault 4
  1    -4.0179     1.1919    -4.0179     3.2119 100    -0.0833    -0.0993    35.0000     8.9547    10.2853
       Fault 5
  1    -3.8715    -0.0239    -4.2476     0.7827 100    -0.0126    -0.0794    30.0000    11.2025    11.8375
       Fault 6
  1    -3.4455     2.0432    -3.4455     2.9832 100    -0.0479    -0.0684    40.0000     8.8825     9.7375
       Fault 7
  1     1.1429    12.8538    -0.0121    14.8543 100    -0.0000    -0.1402    40.0000     9.9772    11.6228
       Fault 8
  1     1.0526    -1.5592     0.8914     0.2838 100    -0.0873    -0.1871    30.0000     7.2775     8.3625
       Fault 9
  1     7.9650    -6.7634     6.2446    -2.0367 100    -0.1101    -0.1907    70.0000    12.1910    16.4290
       Fault 10
  1    -1.0518     2.3119    -1.4718     3.0393 100    -1.6670    -4.5800    45.0000     9.0187     9.8813
       Fault 11
  1     7.2494    -4.4107     7.6109    -4.7983 100     3.3094   -10.1852    73.0000     8.5792     9.4208
       Fault 12
  1    -1.2087    19.9031     0.9307    16.8477 100    -0.0000    -0.3699    40.0000     9.2766    11.6034
       Fault 13
  1     5.9019    -1.3179     5.4969    -0.6165 100    -0.0440    -0.0628    90.0000    13.6550    14.8450
       Fault 14
  1     5.2366    11.7938     5.2985    12.5011 100    -0.0681    -0.0681    55.0000     6.7877     7.6723
       Fault 15
  1    -0.7317    20.6646     1.1068    18.8262 100     0.0009    -0.0101    45.0000     9.1136    11.0864
       Fault 16
  1    -0.0452    17.3573    -0.9496    19.2968 100    -0.0025    -0.0140    30.0000     5.1650     6.3750
       Fault 17
  1     9.8142   -11.6463     9.6434   -11.0087 100    -0.0464    -0.0995    35.0000     9.2975     9.8825
       Fault 18
  1    -1.9968    11.1286    -2.6910    11.9559 100    -0.0120    -0.0449    90.0000    10.6750    12.1450
       Fault 19
  1     0.3838    -1.4664     0.2640    -0.7869 100    -0.0427    -0.0915    40.0000     9.2993     9.9807
       Fault 20


    Grid Parameters
  1  ----------------------------  Start-x =     -64.1494702
  2  ----------------------------  Start-y =     -83.1404175
  3  --------------------------   Finish-x =      50.9906782
  4  --------------------------   Finish-y =      72.5326495
  5  ------------------------  x-increment =       0.9841038
  6  ------------------------  y-increment =       0.9979043

     Size Parameters
  1  --------------------------  Plot size =       2.0000000
  2  --------------  Shade/Color increment =       1.0000000
  3  ------  Exaggeration for disp.& dist. =   10000.0000000

     Cross section default
  1  ----------------------------  Start-x =      13.1854543
  2  ----------------------------  Start-y =      13.5988633
  3  --------------------------   Finish-x =      42.2038077
  4  --------------------------   Finish-y =      42.5815231
  5  ------------------  Distant-increment =       1.0000000
  6  ----------------------------  Z-depth =     -30.0000000
  7  ------------------------  Z-increment =       1.0000000

     Map info
  1  ---------------------------- min. lon =      12.6000004
  2  ---------------------------- max. lon =      14.0000000
  3  ---------------------------- zero lon =      13.3800001
  4  ---------------------------- min. lat =      41.5999985
  5  ---------------------------- max. lat =      43.0000000
  6  ---------------------------- zero lat =      42.3476982
```

# Bibliography

Aki, K., Richards, P.G., 2002. Quantitative Seismology. 2nd Edition, University Science Books.

Allen, J., 2008. Sidoarjo Mud Flow, Indonesia - NASA image created using data from NASA/GSFC/METI/ERSDAC/JAROS and the U.S./Japan ASTER Science Team. *http://earthobservatory.nasa.gov*, accessed January 9, 2011.

Anzidei, M., Boschi, E., Cannelli, V., Devoti, R.; Esposito, A., Galvani, A., Melini, D., Pietrantonio, G., Riguzzi, F., Sepe, V., Serpelloni, E., 2009. Coseismic deformation of the destructive April 6, 2009 L'Aquila earthquake (central Italy) from GPS data. Geophysical Research Letters 36, L17307, doi:10.1029/2009GL039145.

Arndt, H., 2003. Gewöhnliche und verzögerte Differentialgleichungen. Universität Bonn.

Aslan, A., Warne, A.G., White, W.A., Guevara, E.H., Smyth, R.C., Raney, J.A., Gibeaut, J.C., 2001. Mud volcanoes of the Orinoco Delta, Eastern Venezuela. Geomorphology 41, 323-336.

Bar-Meir, G., 2010. Basics of Fluid Mechanics. Chicago, *http://www.potto.org/FM/fluidMechanics.pdf*, accessed March 11, 2011.

Barmin, A., Melnik, O., Sparks, R.S.J., 2002. Periodic behavior in lava dome eruptions. Earth and Planetary Science Letters 199, 173-184.

Batchelor, G.K., 2000. An Introduction to Fluid Dynamics. Cambridge University Press.

BBC News, 2010. Iceland's volcanic ash halts flights in northern Europe. *http://news.bbc.co.uk/2/hi/8622978.stm*, accessed May 27, 2011.

Berry, A., 2010. Indonesia mud volcano still spewing sludge four years later. *http://www.physorg.com/news194273892.html*, accessed January 7, 2011.

Boncio, P., Lavecchia, G., Milana, G., Rozzi, B., 2004. Seismogenesis in Central Apennines, Italy: an integrated analysis of minor earthquake sequences and structural data in the Amatrice-Campotosto area. Annals of Geophysics 47(6), 1723-1742.

Bonini, M., 2007. Interrelations of mud volcanism, fluid venting, and thrust-anticline folding: Examples from the external northern Apennines (Emilia-Romagna, Italy). Journal of Geophysical Research 112, B08413, doi:10.1029/2006JB004859.

Bosl, W.J., Nur, A., 2002. Aftershocks and pore fluid diffusion following the 1992 Landers earthquake. Journal of Geophysical Research 107(B12), 2366, doi:10.1029/2001JB000155.

Brodsky, E.E., Sturtevant, B., Kanamori, H., 1998. Earthquakes, volcanoes, and rectified diffusion. Journal of Geophysical Research 103(B10), 23,827-23,838.

Carcione, J.M., Helle, H.B., 2002. Rock physics of geopressure and prediction of abnormal pore fluid pressures using seismic data. Canadian Society of Exploration Geophysicists Recorder 27, 7, 8-32.

Cartwright, J.H.E., Piro, O., 1992. The Dynamics of Runge-Kutta Methods. International Journal of Bifurcation and Chaos 2, 427-449.

Chiarabba, C., Amato, A., Anselmi, M., Baccheschi, P., Bianchi, I., Cattaneo, M., Cecere, G., Chiaraluce, L., Ciaccio, M.G., De Gori, P., De Luca, G., Di Bona, M., Di Stefano, R., Faenza, L., Govoni, A., Improta, L., Lucente, F.P., Marchetti, A., Margheriti, L., Mele, F., Michelini, A., Monachesi, G., Moretti, M., Pastori, M., Piana Agostinetti, N., Piccinini, D., Roselli, P., Seccia, D., Valoroso, L., 2009. The 2009 L'Aquila (central Italy) M(W)6.3 earthquake: Main shock and aftershocks. Geophysical Research Letters 36, L18308, doi:10.1029/2009GL039627.

Chiodini, G., Cardellini, C., Amato, A., Boschi, E., Caliro, S., Frondini, F., Ventura, G., 2004. Carbon dioxide Earth degassing and seismogenesis in central and southern Italy. Geophysical Research Letters 31, L07615, doi:10.1029/2004GL019480.

Chouet, B., 2003. Volcano Seismology. Pure and Applied Geophysics 160, 739-788.

Cirella, A., Piatanesi, A., Cocco, M., Tinti, E., Scognamiglio, L., Michelini, A., Lomax, A., Boschi, E., 2009. Rupture history of the 2009 L'Aquila (Italy) earthquake from non-linear joint inversion of strong motion and GPS data. Geophysical Research Letters 36, L19304, doi:10.1029/2009GL039795.

Collettini, C., 2002. Hypothesis for the mechanics and seismic behaviour of low-angle normal faults: the example of the Altotiberina fault Northern Apennines. Annals of Geophysics 45, 5, 683-698.

Collettini, C., Barchi, M.R., 2002. A low-angle normal fault in the Umbria region (Central Italy): a mechanical model for the related microseismicity. Tectonophysics 359, 97-115.

Costa, A., Melnik, O., Sparks, R.S.J., Voight, B., 2007. Control of magma flow in dykes on cyclic lava dome extrusion. Geophysical Research Letters 34, L02303, doi:10.1029/2006GL027466.

Connolly, J.A.D., Podladchikov, Y.Y., 1997. Compaction-driven fluid flow in viscoelastic rock. Geodinamica Acta 11, 55-84.

Cox, S.F., 2010. The application of failure mode diagrams for exploring the roles of fluid pressure and stress states in controlling styles of fracture-controlled permeability enhancement in faults and shear zones. Geofluids 10, 217–233, doi:10.1111/j.1468-8123.2010.00281.x.

Davies, R.J., Brumm, M., Manga, M., Rubiandini, R., Swarbrick, R., Tingay, M., 2008. The East Java Mud Volcano (2006 to Present): An Earthquake or Drilling Trigger? Earth and Planetary Science Letters, doi:10.1016/j.epsl.2008.05.029.

Denlinger, R.P., Hoblitt, R.P., 1999. Cyclic eruptive behavior of silicic volcanoes. Geology 27(5), 459-462.

Desjardins, B., Grenier, E., 1998. Low Mach Number Limit of Viscous Compressible Flows in the Whole Space. École Normale Supérieure, Département de Mathématiques et Informatique, Lmens-98-39.

Deville, E., Guerlais, S.-H., Callec, Y., Griboulard, R., Huyghe, P., Lallemant, S., Mascle, A., Noble, M., Schmitz, J., Caramba working group, 2006. Liquefied vs. stratified sediment mobilization processes: Insight from the South of the Barbados accretionary prism. Tectonophysics 428, 33-47.

Dimitrov, L.I., 2002. Mud volcanoes - the most important pathway for degassing deeply buried sediments. Earth Science Reviews 59, 49-76.

Dobran, F., 2001. Volcanic processes: mechanisms in material transport. Kluwer Academic/ Plenum Publishers, New York.

Dormand, J.R., Prince, P.J., 1980. A family of embedded Runge-Kutta formulae. Journal of Computational and Applied Mathematics 6, 1, 19-26.

Dormand, J.R., Prince, P.J., 1986. Runge-Kutta triples, Computers and Mathematics with Applications 12, 9, 1007-1017.

Doukas, M., Griswold, J., 2005. MSH aerial view on hood from NW - USGS Photograph taken on February 25, 2005. *http://vulcan.wr.usgs.gov/Volcanoes/MSH*, accessed December 22, 2010.

Dutta, N., Mukerji, T., Prasad, M., Dvorkin, J., 2002. Seismic detection and estimation of overpressures - Part II: Field Applications. Canadian Society of Exploration Geophysicists Recorder 27, 7, 58-73.

Dzurisin, D., Vallance, J.W., Gerlach, T.M., Moran, S.C., Malone, S.D., 2005. Mount St. Helens reawakens. EOS - Transactions, AGU 86(3), 25.

Fang, H.-Y., Daniels, J.L., 2006. Introductory Geotechnical Engineering: An environmental perspective. Taylor and Francis, London.

Fortes, A.D., Grindrod, P.M., 2006. Modelling of possible mud volcanism on Titan. Icarus 182, 550-558.

Fowler, C.M.R., 2005. The Solid Earth: An Introduction to Global Geophysics. 2nd Edition. Cambridge University Press.

Freed, A.M., 2005. Earthquake Triggering by Static, Dynamic, and Postseismic Stress Transfer. In: Jeanloz, R., Albee, A.L., Burke, K.C. (Eds.), Annual Review of Earth and Planetary Sciences 33, Annual Reviews, Palo Alto, p. 335-367.

GeoNet, 2006. Seismic Monitoring of Volcanoes. *http://www.geonet.org.nz/volcano/monitoring-methods/seismic.html*, accessed February 14, 2011.

Georgiou, G.C, 1996. Extrusion of a compressible Newtonian fluid with periodic inflow and slip at the wall. Rheologica Acta 35, 531-544.

Gephart, J.W., Forsyth, D.W., 1984. An improved method for determining the regional stress tensor using earthquake focal mechanism data - Application to the San Fernando earthquake sequence. Journal of Geophysical Research 89(B11), 9305-9320, doi:10.1029/JB089iB11p09305.

Gisler, G., 2009. Simulations of the explosive eruption of superheated fluids through deformable media. Marine and Petroleum Geology 26, 9, 1888-1895, doi:10.1016/j.marpetgeo.2008.12.006.

Glionna, J.M., 2010. Indonesia's mud volcano flows on. *http://articles.latimes.com/2010/jul/10/world/la-fg-indonesia-mudslide-20100710*, accessed January 10, 2011.

GNS Science, 2009. New Zealand's leading provider of Earth, geoscience and isotope research and consultancy services. *http://www.gns.cri.nz/content/download/6157/33798/file/QuickFacts%20%20WhiteIsland.pdf*, accessed February 14, 2011.

Gowd, T.N., 2004. Stable continental region earthquakes due to pressure-weakening of existing faults. Journal of the Indian Geophysical Union 8, 3, 195-198.

Harris, R.A., 1998. Introduction to a special section: Stress triggers, stress shadows, and implications for seismic hazards. Journal of Geophysical Research 103(B10), 24,347-24,358, doi:10.1029/98JB01576.

Hayes, G.P., Briggs, R.W., Sladen, A., Fielding, E.J., Prentice, C., Hudnut, K., Mann, P., Taylor, F.W., Crone, A.J., Gold, R., Ito, T., Simons, M., 2010. Complex rupture during the 12 January 2010 Haiti earthquake. Nature Geoscience, doi:10.1038/ngeo977.

Herrmann, R. B., Malagnini, L., 2009. Fault dynamics of the April 6, 2009 L'Aquila Italy earthquake sequence (draft). *http://www.eas.slu.edu/Earthquake_Center/MECH.IT*, accessed March 1, 2010.

Henrici, P., 1962. Discrete Variable Methods in Ordinary Differential Equations. John Wiley and Sons, New York.

Hill, D.P., Pollitz, F., Newhall, C., 2002. Earthquake-volcano interactions. Physics Today 55, 11, 41-47.

Hovland, M., Hill, A., Stokes, D., 1997. The structure and geomorphology of the Dashgil mud volcano, Azerbaijan. Geomorphology 21, 1-15.

Huppert, H.E., Woods, A.W., 2002. The role of volatiles in magma chamber dynamics. Nature 420, 493-495.

Ingebritsen, S.E., Rojstaczer, S.A., 1993. Controls on Geyser Periodicity. Science 262, 889-892.

ISIDe, 2009. The Italian Seismic Instrumental and parametric Data-base. Italian Seismic Bulletin, Istituto Nazionale di Geofisica e Vulcanologia, *http://iside.rm.ingv.it*, accessed April 27, 2010.

Iverson, R.M., 2009. Dynamics of Seismogenic Volcanic Extrusion Resisted by a Solid Surface Plug, Mount St. Helens, 2004-05. In: Sherrod, D.R., Scott, W.E., Stauffer, P.H. (Eds.), A Volcano Rekindled: The Renewed Eruption of Mount St. Helens, 2004-2006. U.S. Geological Survey Professional Paper 1750, Chap. 21.

Iverson, R.M., Dzurisin, D., Gardner, C.A., Gerlach, T.M., LaHusen, R.G., Lisowski, M., Major, J.J., Malone, S.D., Messerich, J.A., Moran, S.C., Pallister, J.S., Qamar, A.I., Schilling, S.P., Vallance, J.W., 2006. Dynamics of seismogenic volcanic extrusion at Mount St Helens in 2004-05. Nature 444, 439-443.

Iverson, W.P., Martinsen, R.S., Surdam, R.C., 1994. Pressure seal permeability and two-phase flow. American Association of Petroleum Geologists, Memoir 61, 313-320.

Kim, V., 2011. Japan damage could reach $235 billion, World Bank estimates. Los Angeles Times Business, *http://www.latimes.com/business/la-fgw-japan-quake-world-bank-20110322,0,3799976.story*, accessed May 27, 2011.

King, G. C. P., Stein, R. S., Lin, J., 1994. Static stress changes and the triggering of earthquakes. Bulletin of the Seismological Society of America 84, 935-953.

Law, B.E., Ulmishek, G.F., Slavin, V.I. (Eds.), 1998. Abnormal pressures in hydrocarbon environments. American Association of Petroleum Geologists, AAPG Memoir 70.

Lay, T., Kanamori, H., Ammon, C.J., Nettles, M., Ward, S.N., Aster, R.C., Beck, S.L., Bilek, S.L., Brudzinski, M.R., Butler, R., DeShon, H.R., Ekström, G., Satake, K., Sipkin, S., 2005. The Great Sumatra-Andaman Earthquake of 26 December 2004. Science 308, 5725, 1127-1133, doi: 10.1126/science.1112250.

Lensky, N.G., Sparks, R.S.J., Navon, O., Lyakhovsky, V., 2008. Cyclic activity at Soufrière Hills Volcano, Montserrat: degassing-induced pressurization and stick-slip extrusion. Geological Society London, Special Publications 307, 169-188, doi:10.1144/SP307.10.

Lin, J., Stein, R.S., 2004. Stress triggering in thrust and subduction earthquakes, and stress interaction between the southern San Andreas and nearby thrust and strike-slip faults. Journal of Geophysical Research 109, B02303, doi:10.1029/2003JB002607.

Lindman, M., Lunda, B., Robertsa, R., Jonsdottir, K., 2006. Physics of the Omori law: Inferences from interevent time distributions and pore pressure diffusion modeling. Tectonophysics 424(3-4), 209-222, doi:10.1016/j.tecto.2006.03.045.

Linnenbrink, M., 2010. Ein Jahr nach dem Erdbeben. Deutsche Welle, Aus der Mitte Europas, *http://www.dw-world.de/dw/article/0,,5434840,00.html*, accessed May 27, 2011.

Lions, P.-L., Masmoudi, N., 1998. Incompressible Limit for a Viscous Compressible Fluid. Journal de Mathématiques Pures et Appliquées 77, 585-627.

Manga, M., Brodsky, E., 2006. Seismic triggering of eruptions in the far field: Volcanoes and geysers. Earth and Planetary Sciences 34, 263-291.

Manga, M., Rudolph, M.L., Brumm, M., 2009. Earthquake Triggering of Mud Volcanoes. Marine and Petroleum Geology 26, 9, 1785-1798, doi:10.1016/j.marpetgeo.2009.01.019.

Mazzini A., Svensen, H., Akhmanov, G.G., Aloisi, G., Planke, S., Malthe-Sørenssen, A., Istadi, B., 2007. Triggering and dynamic evolution of the LUSI mud volcano, Indonesia. Earth and Planetary Science Letters 261, 375-388.

Mazzini, A., Nermoen, A., Krotkiewski, M., Podladchikov, Y., Planke, S., Svensen, H., 2009. Strike-slip faulting as a trigger mechanism for overpressure release by piercement structures. Implications for the Lusi mud volcano, Indonesia. Marine and Petroleum Geology 26, 9, 1751-1765, doi:10.1016/j.marpetgeo.2009.03.001.

Mazzini, A., Svensen, H., Planke, S., Guliyev, I., Akhmanov, G.G., Fallik, T., Banks, D., 2009. When mud volcanoes sleep: Insight from seep geochemistry at the Dashgil mud volcano, Azerbaijan. Marine and Petroleum Geology 26, 9, 1704-1715, doi:10.1016/j.marpetgeo.2008.11.003.

Mazzini, A., 2009. Mud volcanism: Processes and implications. Marine and Petroleum Geology 26, 9, 1677-1680, doi:10.1016/j.marpetgeo.2009.05.003.

McKenzie, D.P., 1969. Relation between fault plane solutions for earthquakes and directions of principal stresses. Bulletin of the Seismological Society of America 59, 2, 591-601.

McNutt, S.R., 2000. Volcanic seismicity. In: Sigurdsson, H. (Ed.), Encyclopedia of Volcanoes. Academic Press, San Diego, p. 1015-1033.

Melnik, O., Sparks, R.S.J., 1999. Nonlinear dynamics of lava dome extrusion. Nature 402, 37-41.

Melnik, O., Sparks, R.S.J., 2005. Controls on conduit magma flow dynamics during lava dome building eruptions. Journal of Geophysical Research 110, B02209, doi:10.1029/2004JB003183.

Michael, A.J., 1984. Determination of stress from slip data - Faults and folds. Journal of Geophysical Research 89(B13), 11517-11526.

Michael, A.J., 1987. Use of focal mechanisms to determine stress - A control study. Journal of Geophysical Research 92(B1), 357-368, doi:10.1029/JB092iB01p00357.

Miller, S.A., Nur, A., Olgaard, D.L., 1996. Earthquakes as a Coupled Shear Stress - High Pore Pressure Dynamical System. Geophysical Research Letters 23(2), 197-200, doi:10.1029/95GL03178.

Miller, S.A., Nur, A., 2000. Permeability as a toggle-switch in fluid-controlled crustal processes. Earth Planet Science Letters 183, 133-146.

Miller, S.A., 2002. Properties of Large Ruptures and the Dynamical Influence of Fluids on Earthquakes and Faulting. Journal of Geophysical Research 107(B9), 2182, doi:10.1029/2000JB000032.

Miller, S.A., Collettini, C., Chiaraluce, L., Cocco, M., Barchi, M., Kaus, B.J.P., 2004. Aftershocks driven by a high-pressure CO2 source at depth. Nature 427, 724-727, doi:10.1038/nature02251.

Moore, P.L., Iverson, N.R., Iverson, R.M., 2008. Frictional Properties of the Mount St. Helens Gouge. In: Sherrod, D.R., Scott, W.E., Stauffer, P.H. (Eds.), A Volcano Rekindled: The Renewed Eruption of Mount St. Helens, 2004-2006. U.S. Geological Survey Professional Paper 1750, Chap. 20.

Moran, S.C., Malone, S.D., Qamar, A.I., Thelen, W., Wright, A.K., Caplan-Auerbach, J., 2008. Seismicity Associated with Renewed Dome Building at Mount St. Helens, 2004-2005. In: Sherrod, D.R., Scott, W.E., Stauffer, P.H. (Eds.), A Volcano Rekindled: The Renewed Eruption of Mount St. Helens, 2004-2006. U.S. Geological Survey Professional Paper 1750, Chap. 2.

Nostro, C., Stein, R.S., Cocco, M., Belardinelli, M.E., Marzocchi, W., 1998. Two-way coupling between Vesuvius eruptions and southern Apennine earthquakes, Italy, by elastic stress transfer. Journal of Geophysical Research 103(B10), 24,487-24,504, doi:10.1029/98JB00902.

Nur, A., Booker, J.R., 1972. Aftershocks caused by pore fluid flow. Science 175, 885.

Okada, Y., 1992. Internal deformation due to shear and tensile faults in a half-space. Bulletin of the Seismological Society of America 82(2), 1018-1040.

Okrusch, M., Matthes, S., 2010. Mineralogie: Eine Einführung in die spezielle Mineralogie, Petrologie und Lagestättenkunde. 8th Edition, Springer Verlag Berlin.

Oran, E.S., Boris, J.P., 2000. Numerical Simulation of Reactive Flow. 2nd Edition, Cambridge University Press.

Pallister J.S., Thornber, C.R., Cashman, K.V., Clynne, M.A., Lowers, H.A., Mandeville, C.W., Brownfield, I.K., Meeker, G.P., 2008. Petrology of the 2004-2006 Mount St. Helens lava dome—implications for magmatic plumbing and eruption triggering. In: Sherrod, D.R., Scott, W.E., Stauffer, P.H. (Eds.), A Volcano Rekindled: The Renewed Eruption of Mount St. Helens, 2004-2006. U.S. Geological Survey Professional Paper 1750, Chap. 30.

Paul-Choudhury, S., Hooper, R. (Eds.), 2011. Second explosion at Fukushima nuclear plant. New Scientist Blogs, *http://www.newscientist.com/blogs/shortsharpscience/2011/03/massive-explosion-rips-through.html*, accessed May 27, 2011.

PNSN, 2010. The Pacific Northwest Seismic Network - All about earthquakes and geologic hazards of the Pacific Northwest. *http://www.ess.washington.edu/SEIS/PNSN/HELENS*, accessed July 28, 2010.

Poling, B.E., Prausnitz, J.M., O'Connell, J.P., 2000. The Properties of Gases and Liquids. 5th Edition, McGraw-Hill Professional.

Powrie, W., 2004. Soil Mechanics. 2nd Edition, Spon Press, London.

Rojstaczer, S., Wolf, S., Michel, R., 1995. Permeability enhancement in the shallow crust as a cause of earthquake-induced hydrological changes. Nature 373, 237-239.

Rozhko, A.Y., Podladchikov, Y.Y., Renard, F., 2007. Failure patterns caused by localized rise in pore-fluid overpressure and effective strength of rocks. Geophysical Research Letters 34, L22304, doi:10.1029/2007GL031696.

Rubey, W. W., Hubbert, M. K., 1959. Role of fluid pressure mechanics of overthrust faulting, II. Overthrust belt in geosynclinal area of Western Wyoming in light of fluid pressure hypothesis. Geological Society of America, 70, 167-205.

Schaefers, M., 2009. Jzeemap0.3 - An open source data overlay tool. *http://sourceforge.net/projects/jzeemap*, accessed Mai 28, 2010.

Scott, W.E., Sherrod, D.R., Gardner, C.A., 2008. Overview of the 2004 to 2006, and Continuing, Eruption of Mount St. Helens, Washington. In: Sherrod, D.R., Scott, W.E., Stauffer, P.H. (Eds.), A Volcano Rekindled: The Renewed Eruption of Mount St. Helens, 2004-2006. U.S. Geological Survey Professional Paper 1750, Chap. 1.

Segall, P., Rice, J.R., 1995. Dilatancy, compaction, and slip instability of a fluid-infiltrated fault. Journal of Geophysical Research 100(B11), 22,155-22,171, doi:10.1029/95JB02403.

Sibson, R. H., 2007. An episode of fault-valve behaviour during compressional inversion? The 2004 M(J)6.8 Mid-Niigata Prefecture, Japan, earthquake sequence. Earth and Planetary Science Letters 257, 188-199, doi:10.1016/j.epsl.2007.02.031.

Skinner, J.A., Mazzini, A., 2009. Martian mud volcanism: Terrestrial analogs and implications for formational scenarios. Marine and Petroleum Geology 26, 9, 1866-1878, doi:10.1016/j.marpetgeo.2009.02.006.

Skinner, J.A., Tanaka, K.L., 2007. Evidence for and implications of sedimentary diapirism and mud volcanism in the southern Utopia highland-lowland boundary plain, Mars. Icarus 186, 41-59.

Stein, J., 2008. Schlamm-“Vulkan” von Sidoarjo. Image taken June 27, 2008. *http://www.flickr.com/photos/drstein/3524815451*, accessed May 11, 2011.

Terakawa, T., Zoporowski, A., Galvan, B., Miller, S.A., 2010. High-pressure fluid at hypocentral depths in the L'Aquila region inferred from earthquake focal mechanisms. Geology 38(11), 995-998, doi:10.1130/G31457.1.

Terzaghi, K., 1943. Theoretical Soil Mechanics. John Wiley and Sons, New York.

Toda, S., Stein, R.S., Sagiya, T., 2002. Evidence from the AD 2000 Izu islands earthquake swarm that stressing rate governs seismicity. Nature 419, 58-61, doi:10.1038/nature00997.

Toda, S., Stein, R. S., Richards-Dinger, K., Bozkurt, S., 2005. Forecasting the evolution of seismicity in southern California: Animations built on earthquake stress transfer. Journal of Geophysical Research 110, B05S16, doi:10.1029/2004JB003415.

Trenkamp, O., 2010. Bilanz der Katastrophe von Chile. Spiegel Online Panorama, *http://www.spiegel.de/panorama/0,1518,684001,00.html*, accessed May 27, 2011.

U.S. Geological Survey, 2010. M 8.8 Maule, Chile, Earthquake of 27 February 2010. Earthquake summary map, *http://earthquake.usgs.gov/earthquakes/eqarchives/poster/2010/20100227.pdf*, accessed May 27, 2011.

U.S. Geological Survey, 2011. The M 9.0 Great Tohoku Earthquake (northeast Honshu, Japan) of March 11, 2011. Earthquake summary map, *ftp://hazards.cr.usgs.gov/maps/sigeqs/20110407/20110407.pdf*, accessed May 27, 2011.

Utsu, T., Ogata, Y., Matsu'ura, R.S., 1995. The centenary of the Omori formula for a decay law of aftershock activity. Journal of the Physics of the Earth 43, 1-33.

Waite, G.P., Chouet, B.A., Dawson, P.B., 2008. Eruption dynamics at Mount St. Helens imaged from broadband seismic waveforms: Interaction of the shallow magmatic and hydrothermal systems. Journal of Geophysical Research 113, B02305, doi:10.1029/2007JB005259.

Walters, R.J., Elliott, J.R., D'Agostino, N., England, P.C., Hunstad, I., Jackson, J.A., Parsons, B., Phillips, R.J., Roberts, G., 2009. The 2009 L'Aquila earthquake (central Italy): A source mechanism and implications for seismic hazard. Geophysical Research Letters 36, L17312, doi:10.1029/2009GL039337.

Wilson, L., Sparks, R.S.J., Walker, G.P.L., 1980. Explosive volcanic eruptions - IV. The control of magma properties and conduit geometry on eruption column behaviour. Geophysical Journal of the Royal Astronomical Society 63, 117-148, doi:10.1111/j.1365-246X.1980.tb02613.x.

Wisner, B., Blaikie, P., Cannon, T., Davis, I., 2004. At Risk - Natural hazards, people's vulnerability and disasters. Wiltshire: Routledge.

Wojtanowicz, A.K., Nishikawa, S., Rong, X., 2001. Diagnosis and remediation of sustained casing pressure in wells. Final Report, Louisiana State University. Submitted to: US Department of Interior, Minerals Management Service, Virginia.

Wylie, J.J., Voight, B., Whitehead, J.A., 1999. Instability of Magma Flow from Volatile-Dependent Viscosity. Science 285, 1883, doi:10.1126/science.285.5435.1883.

Yoshino, M., Hotta, Y., Hirozane, T., Endo, M., 2007. A numerical method for incompressible non-Newtonian fluid flows based on the lattice Boltzmann method. Journal of Non-Newtonian Fluid Mechanics 147 (1-2), 69-78.

Zoporowski, A., Miller, S.A., 2009. Modelling Eruption Cycles and Decay of Mud Volcanoes. Marine and Petroleum Geology 26, 9, 1879-1887, doi:10.1016/j.marpetgeo.2009.03.003.

# List of Figures

1.1 View from north-west of the caldera of Piton de la Fournaise, Île de la Réunion, Indian Ocean. The hot spot fed volcano is currently one of the most active volcanoes in the world, affecting the lives of the island inhabitants. . . . . . . . . . . . . . . . . . . . . . . . . . . . . 2

1.2 Mostly harmless fumaroles (Rotorua, New Zealand), emitting steam and gases such as carbon dioxide, sulfur dioxide, hydrochloric acid, and hydrogen sulfide, may indicate increasing magmatic activity due to changes in gas concentrations. However, $CO_2$ gas can collect in low-lying valleys because of its density larger than air, with the danger of suffocation for humans and animals. . . . . . . . . . . . . . . . . . . . . . 3

1.3 Living on a tectonic faulting system: the diverging Mid-Atlantic Ridge in the Mývatn district, Iceland. The location offers availability of geothermal power, but also volcanic eruptions and earthquake hazard. . . . . . . . . . . . . . . . . . . . . . . . . . . . . . . . . . . 4

1.4 Strokkur geyser in the geothermic region near Hvítá River in Iceland erupts regularly every 4-8 minutes, after being unblocked in 1789 by an earthquake. Beside geysers, earthquakes ruptures are a common remote triggering mechanisms for mud pots, volcanoes, landslides, tsunamis and further seismicity. . . . . . . . . . . . . . . . . . . . . . . 5

1.5 Laacher See in Germany is a caldera lake and a potentially active volcano, proven by seismic activities, thermal anomalies and carbon dioxide gas bubbling up from magma at the southeastern shore. A new eruption could result in a major disaster, especially because Germany is a heavily populated country and this caldera lies just 8 km from the Rhine river. . . . . . . . . . . . . . . . . . . . . . . . . . . 6

1.6 White Island is an active stratovolcano, situated offshore the North Island of New Zealand. Attempts on sulfur mining were stopped after the collapse of the western crater rim had created a lahar, killing 11 mining workers in 1914 (GNS, 2009). . . . . . . . . . . . . . . . . . . 7

2.1 Global distribution of abnormal pressures (heavier shaded) taken from Law et al. (1998). The index numbers refer to selected attributes of abnormally pressured regions of the world given in the same source (e.g. no. 21 Italy, no. 30 Indonesia). . . . . . . . . . . . . . . . . . . 12

2.2 Left: Pressure versus depth plots for uniform density and gravity distributions. Rocks with pressure plots between the hydrostatic (blue) and lithostatic (red) gradients are termed overpressurized. Right: Pressure and/or stress versus depth plot for overpressure generated by disequilibrium compaction. Fluid retention occurs at depth where the permeability and sedimentation rate combine to prevent complete dewatering. Below the fluid retention depth the profile changes to almost constant effective stress (green), i.e. a pressure profile almost parallel to the lithostatic pressure gradient. Figure adopted from Law et al. (1998). . . . . . . . . . . . . . . . . . . . . . . . . . . 13

2.3 Left: Location map of earth degassing processes in central south Italy. Right: Map showing the probability that a deep source of carbon is present at any location, compared with seismic activity. Figures taken from Chiodini et al. (2004). For more details we refer to captions and text given therein. . . . . . . . . . . . . . . . . . . . . . . . . . 14

2.4 The stresses on the surfaces of an infinitesimal small control volume. $\sigma_{xx}, \sigma_{yy}, \sigma_{zz}$ are normal stresses, $\tau_{ij}, i, j = x, y, z, i \neq j$ indicate shear stresses. . . . . . . . . . . . . . . . . . . . . . . . . . . 16

2.5 Mohr's circle for a three-dimensional state of stress. $\sigma_1$ is the maximum, $\sigma_3$ the minimum principle stress and $\sigma_2$ lies in between. . . . . 17

2.6 Mohr's circle and Coulomb failure curve. The circle increases, when increasing $\sigma_1$ or decreasing $\sigma_3$ while remaining the other constant, and hits the Coulomb failure criterion. The frictional strength of the fault is exceeded and an earthquake occurs. . . . . . . . . . . . . . 18

2.7 Mohr's circle and Coulomb failure curve for effective stress $\sigma_{\text{eff}}$. The circle moves when increasing pore pressure $p$ while remaining the other stresses constant, and hits the Coulomb failure criterion. The frictional strength of the fault is exceeded and an earthquake occurs at lower shear stresses $\tau$. . . . . . . . . . . . . . . . . . . . . . . . . 19

2.8 The mass balance in Cartesian coordinates on the infinitesimal control volume. Figure taken from Bar-Meir (2010, p. 228). . . . . . . . . . . 21

2.9 Illustration (no scale) of the shear stress $\tau$ versus strain rate $\dot{\varepsilon}$ behavior for Newtonian and non-Newtonian fluid properties. . . . . . . . . 23

2.10 Illustration of laminar and turbulent flows through a cylindrical pipe. For laminar viscous flows the Poiseuille flow condition (2.23) holds. . 24

2.11 Illustration of multi-phase flows. Gas-liquid, liquid-liquid and liquid-solid flows occur very often in geoscientific settings. . . . . . . . . . . 25

2.12 Illustration (no scale) of a continental volcanic system showing the local occurrence of earthquakes. Figure taken from Hill et al. (2002). 26

2.13 Waveforms for typical volcano-tectonic, hybrid and low-frequency events recorded at Mount St. Helens, Washington, during first four days of renewed activity in 2004. Time in seconds. Figure source: Moran et al. (2008). . . . . . . . . . . . . . . . . . . . . . . . . . 28

2.14 Real-time seismic-amplitude measurement plot (overall signal size over periods of 10 minutes, top) and seismic spectral-amplitude measurement plot (relative signal size in different frequency bands, bottom) showing volcanic tremor at Mt. Ruapehu, New Zealand, 2006. Volcanic tremor tends to have energy in a limited range of frequencies (a narrow-band signal). Figure source: GeoNet (2006). . . . . . . . . 29

2.15 Left: Seismic record from 1700 on October 15 through 1800 on October 17, 2004, showing onset of small, regularly spaced events occurring between larger events at MSH. Right: Plot showing spectral-amplitude (dominating LF band, top), inter-event spacing (period of approx. 150 s, middle), and peak amplitudes (bottom) for detected events at MSH between September 23, 2004, and December 31, 2005. Figure taken from Moran et al. (2008). . . . . . . . . . . . . . . . . . 30

3.1 (a) Mud volcanoes belonging to a mud pool near Krafla volcano. (b)-(e) Detailed view on an eruption. Námaskarð region, Iceland. . . . . . 34

3.2 Schematic illustrating the basic concept of our two-component mud volcano model (not to scale). . . . . . . . . . . . . . . . . . . . . . . 35

3.3 Discharge rate $Q$ solutions for a change in initial conditions. (a) Decreasing $V_0$, a faster decay can be seen. (b) Close-up, no period changes. (c) A decrease in $I_0$ changes the extrusion intensity and decay. (d) Detailed view shows amplitude changes by factor 0.5, while period remains the same. (e) Long-term $Q$ solution for increase in initial discharge rate $Q_0$. (f) The period between oscillation peaks drops to approx. 2 hours. . . . . . . . . . . . . . . . . . . . . . . . . 42

3.4 Discharge rate $Q$ for changes in parameter values. (a) Long-term behavior of mud compressibility $\beta$, decay occurs already after six months. (b) The smaller $\beta$, the shorter the discharge rate period. (c) Long-term discharge rate $Q$ for increase in mud viscosity $\mu$. Eruption period remains the same, oscillation amplitude decreases. (d) Reaching $\mu = 1$ Pa s, constant mud extrusion is observed following one significant discharge peak, decaying later on towards zero (not visible here). (e) Long-term discharge rate $Q$ evolution for increase in $A$ and (f) zoomed detail. Same effects can be seen for decrease in height $h$. . . . . . . . . . . . . . . . . . . . . . . . . . . . . . . 43

3.5 (a) Solutions for the influx $I$ and discharge $Q$ functions calculated from Equations (3.3, 3.5 and 3.10) given in previous paragraphs. As the mud reservoir deflates, $I$ decreases, and $Q$ decays towards zero following the solution graph of $I$. (b) Long-term discharge $Q$ and influx $I_{const}$ rates behavior. $Q$ decays towards the value of $I_{const}$. Logarithmic time scale. . . . . . . . . . . . . . . . . . . . . . . . . 44

3.6 (a) Limit cycle and (b) detailed view for constant influx rate. Stable state of $Q$ is reached, when oscillating about the value of $I_{const} = 1$ m$^3$/s. Plotted versus fluctuating reservoir volume $V$. (c) Limit cycle, discharge rate $Q$ vs. reservoir volume $V$, for an open mud conduit with deflating source. (d) Zoomed detail of Figure c, showing up the initialization and equilibrium points. Periodic behavior with stable state in (0,0). . . . . . . . . . . . . . . . . . . . . . . . . . . 45
3.7 Discharge rate $Q$ functions for different values of $I_{const}$, (a) Long-term behavior and (b) zoomed detail. (c) Discharge rate $Q$ for constant $I$ and additional changes in $\mu$. (d) As expected, the discharge rate oscillation amplitude changes. . . . . . . . . . . . . . . . . . . . . . 46
3.8 Extruded volume at surface of the mud volcano. (a) Dependence on a constant influx $I_{const}$. (b) Dependence on initial conditions, when $I$ is not constant. (c) Dependence on parameter choices, when $I$ and $Q$ decay to zero. . . . . . . . . . . . . . . . . . . . . . . . . . . . 46

4.1 Map view of the L'Aquila region, Apennines, Italy, showing the location of the April 6 main shock and $M_w > 2$ aftershocks for a total of three months. . . . . . . . . . . . . . . . . . . . . . . . . . . . . 52
4.2 Aftershocks number per day plotted versus time in logarithmic scale. Black circles show earthquake number for all magnitudes plotted versus time in days together with the linear decay rate fitting. Additionally, colored marks give the number of earthquakes broken down according to their magnitude. . . . . . . . . . . . . . . . . . . . . . 53
4.3 The aftershock decay rate data-fitting. Black circles show earthquake number for all magnitudes plotted versus time in days. Left: Aftershocks number per day plotted versus time in logarithmic scale. Right: The Omori's Law decay rate function is given as red line ($p = 1.14$ for $c = 0$). . . . . . . . . . . . . . . . . . . . . . . . . 54
4.4 Spatial distribution of aftershocks. The horizontal axis gives the distance from the red fault center, representing the $M = 6.3$ L'Aquila main shock on 06/04/2009 1:32, the vertical axis is the depth. The smaller events propagate to the north, clustering near Campotosto. Different fault colors give the net slip in meters, estimated from earthquake magnitude-area relations. Cross section view (a) perpendicular to the main fault, (b) from south-east and (c) from north-east. . . . . 56
4.5 The spatiotemporal pattern of the Campotosto aftershock cluster (not equal time steps). Aftershocks with $M > 4$ (yellow rectangles) trigger smaller events (orange dots) in the hanging wall. Video screen-shots created with the data overlay tool Jzeemap0.3 (Schaefers, 2009). . . . 57
4.6 Fault source model inferred from InSAR and its influence on the Apennines region. Sliced views on the Coulomb stress change (left) and dilatation (right) in 5, 7.5, 10 and 12.5 km depth. Aftershocks to the east and west are in decreased stress regions and are situated on borders between high and low dilatation. . . . . . . . . . . . . . 59

4.7 Fault source model inferred from GPS data. Top views of stress (left) and dilatational (right) effects in depths of 5, 7.5, 10 and 12.5 km are superposed with $M_w > 2.5$ aftershocks. Most aftershocks lie in negative $\Delta CFS$ regions and occur between max. and min. dilatation values. . . . . . . . . . . . . . . . . . . . . . . . . . . . . . . . 60

4.8 Fault source model with non-uniform slip adopted from Cirella et al. (2009). Views for 7 and 10 km depth. Only deep earthquakes match well with static stress transfer assumptions (left). Earthquakes occur between high and low dilatation regions (right). . . . . . . . . . . . . 61

4.9 Coulomb stress change $\Delta CFS$ (left) and dilatation (right) as map view of the region produced by the multi-fault system at 7.5 km and 10 km depth. Red rectangles show the locations and sizes of the source faults, black circles indicate the aftershock locations. . . . . . . 62

4.10 Cross-section view from south-east on the regional changes caused by the multi-fault system. Coulomb stress change on left and dilatation on right. . . . . . . . . . . . . . . . . . . . . . . . . . . . . . . . 63

5.1 Top view of Mount St. Helens crater and north-south and east-west conduit profiles. The new 2006 lava dome is accentuated. Figures adopted from PNSN (2010). . . . . . . . . . . . . . . . . . . . . . . . 68

5.2 The model sketch (not to scale, based on (Iverson et al., 2006)) showing the upper 2 km of a volcanic conduit, plugged by solidified magma. The magma pressure driven plug ascend is resisted by a friction force, including the concept of effective stress. . . . . . . . . . . . . . . . . 70

5.3 (a) Plug displacement calculation for 15 months of MSH activity. Plot indicates the linearity of the extrusion rate. (b) Stepwise motion characteristics, indicating underlying stick-slip mechanism for drumbeat creation ($t < 8000$ s). (c) Oscillating motion characteristics due to up- and downward plug motion ($t > 8000$ s). . . . . . . . . . . . . . 75

5.4 (a) Calculated velocity evolution during the first 8000 s (2.5 hours). (b) Extrusion velocity calculation for 15 months of MSH activity. Logarithmic scale. . . . . . . . . . . . . . . . . . . . . . . . . . . . . 76

5.5 Plug displacement depending on parameter variations. Characteristics due to (a) plug mass change rate $\kappa$, (b) the change in the coefficient of friction $\mu$ and (c) in the fault gouge permeability $k$. For increases in $\kappa$ and $k$ the period between slip events remains the same, but the slip distance decreases. Changes in $\mu$ do not yield significant result differences. (d) The amplitude and frequency of plug displacement depends strongly on the initial plug mass $m_0$ and (e) the change in the initial velocity $u_0$ effects large amplitude differences. (f) Plug displacement depending on the change in the initial magma volume $V_0$ results in solutions similar to 5.5(a). . . . . . . . . . . . . . . . . . 77

5.6 Plug displacement depending on different degassing rules and time-dependent parameter functions. (a) Vapor-liquid-equilibrium versus Henry's law assumption on the exsolution behavior with (b) detailed view on amplitude changes. (c) and (d) show arbitrary time-dependent (cyclic) coefficient of friction $\mu(t)$ with break down of the linear extrusion rate ($\mu$ constant), and (e) and (f) exhibit the effect of an exponentially decreasing gouge permeability function $k(t)$ compared with constant $k$. . . . . . . . . . . . . . . . . . . . . . . . . . 79

6.1 LUSI, the Lumpur Sidoarjo mud flow in East Java, Indonesia. Top view on mud flooded area. The Advanced Spaceborne Thermal Emission and Reflection Radiometer on NASA's Terra satellite acquired these image on November 11, 2008. In these false-color images, red indicates vegetation, pale blue and green indicate bare ground and/or fallow fields, and black indicates water. Figure source: Allen (2008). . 84
6.2 Flooded landscape in Sidoarjo, Indonesia, including streets, buildings and agricultural areas. More than 40 thousand inhabitants are still affected. Steaming LUSI and the stratovolcano Mount Penanggungan can be seen in the background. Picture taken from Stein (2008). . . . 84
6.3 Aerial view from north-west of a steaming Mount St. Helens with extruded lava dome. Picture source: Doukas and Griswold (2005). . . 85
6.4 Three-dimensional image of the excess fluid pressure field with the hypocenters of foreshocks and aftershocks (Chiarabba et al., 2009) and projected fault of the main shock (Cirella et al., 2009). View is from the northeast toward southwest. Figure taken from Terakawa et al. (2010, Fig. 3B). . . . . . . . . . . . . . . . . . . . . . . . . . . . 87

# List of Tables and Listings

3.1 Parameter symbols, description and their values or conversion used for numerical computation. . . . . . . . . . . . . . . . . . . . . . . . . 41

4.1 Events used for stress and dilatation calculations for the multi-fault system. Data based on moment tensor solutions provided by Herrmann and Malagnini (2009). . . . . . . . . . . . . . . . . . . . . . . 55

5.1 Parameter symbols, description and their values used in modeling and for numerical computation. Adopted or calculated from values given in (Iverson, 2008; Moore et al., 2008; Pallister et al., 2008; Scott et al., 2008). . . . . . . . . . . . . . . . . . . . . . . . . . . . . . . . 74

A.1 Coulomb 3.1 input file for a single source fault with uniform slip distribution. . . . . . . . . . . . . . . . . . . . . . . . . . . . . . . 95
A.2 Coulomb 3.1 input file for a single source fault with non-uniform slip. 96
A.3 Coulomb 3.1 input file for a multi-fault system with uniform slip distribution. . . . . . . . . . . . . . . . . . . . . . . . . . . . . . . 97

# Symbols and Abbreviations

| | |
|---|---|
| 1D, 3D | one-dimensional, three-dimensional |
| $A$ | area |
| $a_{ij}, b_i^*, b_j, c_i$ | coefficients in Runge-Kutta method |
| $\alpha_1$ | magma compressibility |
| $\alpha_2$ | elastic compliance of conduit walls |
| $\forall$ | for all |
| $B$ | accretion rate |
| $\beta$ | compressibility |
| $CO_2$ | carbon dioxide |
| $C_{ijkl}$ | elasticity tensor |
| $c$ | time offset in Omori's Law |
| $c_0$ | cohesion |
| $d$ | plug displacement |
| $dx$ | differential of $x$ |
| $\Delta$ | difference |
| $\Delta CFS$ | Coulomb failure stress change |
| $\nabla, \nabla\cdot$ | vector differential operator (gradient, divergence) |
| $\nabla^2$ | vector Laplace operator |
| $\partial x$ | partial differential of $x$ |
| $E$ | Young's modulus |
| $E$ | erosion rate |
| $\varepsilon, \varepsilon_{ij}$ | strain, strain tensor components |
| $\dot{\varepsilon}$ | strain rate |

| | |
|---|---|
| $\varepsilon_h$ | global error in Runge-Kutta method |
| $\in$ | element |
| FMT | Focal Mechanism Tomography |
| $F$ | force, friction force |
| $f$ | oscillation frequency |
| $_f, _m, _s$ | subscripts for fluid, magma, solid |
| $\mathbf{f}$ | body force |
| $\varphi$ | porosity |
| $\varphi$ | external force |
| GPS | Global Positioning System |
| $G$ | shear modulus |
| $G$ | liquid/gas phase change |
| $g$ | gravitational acceleration |
| $\gamma$ | damping constant |
| HF | High-Frequency |
| $H_2O$ | water |
| $H_2S$ | hydrogen sulfide |
| $H$ | enthalpy |
| $h$ | height, depth |
| $h$ | step length in Runge-Kutta method |
| $\eta$ | dynamic viscosity |
| InSAR | Interferometric Synthetic Aperture Radar |
| $I, I_0, I_{const}$ | mud influx rate, initial influx rate, constant influx rate |
| $_i, _j, _k, _l$ | indices |
| $\mathbb{I}$ | identity matrix |
| $K$ | earth pressure coefficient |
| $k$ | permeability |
| $k$ | Boltzmann's constant |
| $k$ | amplitude in Omori's Law |

| | |
|---|---|
| $\kappa$ | mass increase rate |
| LF | Low-Frequency |
| LP | Long-Period |
| LUSI | Lumpur Sidoarjo mud flow |
| $L$ | Lipschitz constant |
| $\Lambda$ | dissipation of energy due to viscous effects |
| $\lambda$ | second coefficient of viscosity |
| $\lambda$ | convex combination parameter |
| MSH | Mount St. Helens |
| $M, M_w, M_0$ | magnitude, moment magnitude, seismic moment |
| $m, m_0$ | mass, initial mass |
| max | maximum |
| $\mu$ | coefficient of friction |
| $\mu$ | dynamic viscosity |
| NASA | National Aeronautics and Space Administration |
| NE | North-East |
| NW | North-West |
| $N$ | number of particles |
| $N$ | initial volatile content |
| $n$ | volatile concentration |
| $\vec{n}$ | normal vector |
| $\nu$ | Poisson's ratio |
| $\mathbb{N}$ | set of natural numbers |
| $\omega$ | characteristic, natural, angular frequency |
| $\mathcal{O}$ | limiting behavior of a function |
| PDT | Pacific Daylight Time |
| $p$ | aftershock decay rate in Omori's Law |
| $p, p^*$ | order of Runge-Kutta method |
| $p, p_0$ | pressure, initial pressure |

| | |
|---|---|
| $p_{z_0}$ | pressure at zero reference depth |
| $\pi$ | ratio of the circumference of a circle to its diameter ($\approx 3.14159$) |
| $Q$ | magma influx rate |
| $Q, Q_0$ | mud discharge rate, initial discharge rate |
| $R$ | rate of earthquakes in Omori's Law |
| $r$ | local error in Runge-Kutta method |
| $r, r_0$ | radius, initial radius |
| $\rho$ | density |
| $\mathbb{R}, \mathbb{R}^m$ | set of real numbers, $m$-dimensional vector space of real numbers |
| SE | South-East |
| SHV | Soufrière Hills Volcano |
| SP | Short-Period |
| SPASM | Seismogenic Plug of Ascending Solidifying Magma |
| SW | South-West |
| $SO_2$ | sulfur dioxide |
| $\sin, \cos, \tan$ | sine, cosine, tangent |
| $\sup$ | supremum |
| $S$ | liquid/solid phase change |
| $S, S_0$ | surface area, initial surface area |
| $s$ | solubility of water |
| $s$ | stage of Runge-Kutta method |
| $\sigma, \sigma_{ij}$ | stress, stress tensor components |
| $\sigma_n, \sigma_{\mathrm{eff}}$ | normal stress, effective stress |
| $\sigma_1, \sigma_2, \sigma_3$ | principal stresses |
| $\sum$ | sum |
| $\int$ | integral |
| $T$ | temperature |
| $^T$ | transpose |
| $t$ | time |

| | |
|---|---|
| $\tau, \tau_{ij}$ | shear stress, stress tensor components |
| $\theta$ | plane angle |
| $\theta$ | coefficient for the Runga-Kutta interpolants |
| $\mathbb{T}$ | deviatoric stress tensor |
| USGS | United States Geological Survey |
| UTC | Coordinated Universal Time |
| $u, u_x$ | displacement, displacement in $x$-direction |
| $u, u_0$ | velocity, initial velocity |
| $\bar{u}$ | average velocity |
| $u_j, u_0$ | solution approximation in Runge-Kutta method, initial value |
| VLP | Very-Long-Period |
| VT | Volcano-Tectonic |
| $V, V_0$ | volume, initial volume |
| $v, v_0$ | velocity, initial velocity |
| $v_j$ | scheme function in Runge-Kutta method |
| $\mathbf{v}$ | velocity vector field |
| $x$ | oscillator |
| $\dot{x}, \ddot{x}$ | time derivatives of $x$ |
| $x, y, z$ | Cartesian coordinates |
| $\xi, \upsilon, \zeta$ | variables of integration |
| $y, \tilde{y}$ | initial value problem solution |
| $y', y'', y^{(p)}$ | derivatives of $y$ |
| $y_0$ | initial value in $x_0$ |
| $z_0$ | zero reference depth |
| $\lVert\cdot\rVert$ | norm |
| $\lvert\cdot\rvert$ | absolute value |
| $\rightarrow$ | approaches |

# Acknowledgments

It is a pleasure to express my gratitude to those who have contributed to the completion of this thesis.

First of all, I am very much obliged to Prof. Dr. Steven A. Miller for his motivating research projects and his constructive criticism. I also appreciate Prof. Dr. Andreas Kemna's encouragement and his second opinion on this dissertation. Many thanks are given to the remaining members of the examining board, Prof. Dr. Bernd Diekkrüger and PD Dr. Jürgen Kerp, for their willingness to join the committee.

A sincere thank you is directed to all colleagues of the Geodynamics / Applied Geophysics group, and the members of the "Kaffeerunde" for the nice working atmosphere. In particular, I am very grateful to Dr. Toshiko Terakawa for her scientific advice and Dr. Andreas Dreist for the excellent IT working conditions.

On a personal level, I will always be indebted to my companion in life Michael Schaefers, my sister Monika and my parents Barbara and Johann Zoporowski, as well as my friends, for their encouragement and undesigning support.